Scanning Probe Microscopy and Electrochemical Studies of Deposition on Electrode Surfaces

A thesis submitted for the

Degree of Doctor of Philosophy

University of Oxford

Michael Edwin Hyde

New College

Trinity Term 2005

Scanning Probe Microscopy and Electrochemical Studies of Deposition on Electrode Surfaces

Abstract of a thesis submitted for the degree of Doctor of Philosophy

Michael Edwin Hyde

New College, Trinity Term 2005

SPM, optical microscopy, and electrochemical techniques are used to study a range of electrochemical deposition processes on carbon electrodes, particularly those associated with diffusion-controlled multiple nucleation.

Anodic stripping voltammetry for analytical measurements using solid electrodes is addressed in the light of limitations arising from electrode heterogeneity, electrode morphology, inhibited electrodeposition, and incomplete stripping of deposited metal. It is shown, using direct imaging of electrode surfaces, that each of the preceding factors may produce significant deviations from ideal electrode behaviour.

The electrochemical nucleation of silver on BDD is examined. Data are obtained for the nucleation rate by interpretation of the deposition voltammetry, and by inspection of in-situ optical microscopic images. The particle distributions are analyzed and a stochastic model of nucleation developed.

A model for the potentiostatic nucleation and three dimensional growth of deposits on an electrode surface under hydrodynamic conditions is examined. A wall-tube and stirred cell are used to generate conditions in which the diffusion layer thickness is in

the range 10 – 40 μm. It is shown that the model provides excellent fits to the experimental data.

A previously unrecognised correlation between the morphology of the PbO_2 deposits and their electrocatalytic activity is established. The morphology of the films are observed as a function of time and potential using in-situ AFM.

Nanotrench arrays are fabricated on HOPG surfaces. Cyclic voltammetry in simple redox couples is used to provide experimental evidence that the voltammetric response of a graphite electrode is solely due to the edge plane sites, with the basal plane sites having no measurable contribution.

Nanotrenches are used as templates in a simple method for generating random assemblies of metal nanobands. This method is shown to be effective for generating gold, silver and copper nanowires. The electrochemical properties of the array are investigated via cyclic voltammetry.

Acknowledgements

First I would like to thank Richard Compton for giving me the opportunity to work in his group, and for his help and supervision over the last four years.

I would like to thank, in no particular order, Robert Jacobs for his help with the AFM and metal evaporation, Oleksiy Klymenko for helping with the mathematics in appendix 3, and Trevor Davies for his work with the HOPG.

I would also like to thank my parents and Christine for their support.

Contents

1 Dynamic Electrochemistry

Electrochemical deposition is the formation of a new phase from a solution of ions, at the electrode/electrolyte interface. In the case of electrochemical metal phase formation creating crystalline metal deposits, the process is known as electrocrystallization. More generally, the term electrodeposition is used. The heterogeneous transfer of electrons from the solution environment is clearly a key process in electrodeposition. Voltammetric methods can be used to probe these processes, offering a range of experimental methods to best suit the system of interest. Both steady-state and transient methods are used; however the methods employed in this thesis are exclusively transient, and these are the methods discussed in more detail below. The use of voltammetry also allows precise control of the experimental conditions.

1.1 Voltammetry

1.1.1 Introduction

In electrochemical experiments, a current is generated by the transfer of electrons between the electrode surface and any electroactive species (where 'electroactive' means capable of undergoing a redox process under the conditions in the cell) in solution in contact with it. There are two main methods of controlling such a system: [1]

- Galvanostatic control, in which the current passing through the system is controlled, and the potential measured.
- Potentiostatic control, in which the electrode potential is controlled, and the current is measured.

Galvanostatic control is commonly used in areas such as bulk metal plating. However, the mechanism of electrodeposition is often highly potential dependent; all of the techniques used in this thesis therefore employ potentiostatic control, and hence it is the only type considered further.

1.1.2 The electrochemical cell

In principle, the simplest arrangement for the measurement of a current response to an applied potential would be to use a two electrode system consisting of an inert, conductive working electrode (WE) and a reference electrode (RE). The reference electrode produces a stable potential such that when a voltage is applied between the electrodes the potential drop between them is well defined. The voltage applied to the cell is then given by

$$E_{appl} = \left(E_{WE} - E_{RE}\right) + iR_s \tag{1.1}$$

in which E_{WE} and E_{RE} are the potentials of the working electrode and reference electrode respectively. R_s is the resistance of the solution and i is the current flowing between the two electrodes. This allows the current response of the working electrode relative to the solution to be measured, assuming two conditions are met: first, that E_{RE} is in fact stable, and second that the iR_s term is small enough to be negligible. The former is usually not the case if relatively large currents are flowing. For these reasons, two electrode cells are more commonly used with microelectrodes, where the cell currents are low enough to meet the two above conditions.

However, for cells involving larger currents (i.e. macroelectrodes), a more sophisticated control system is required.[2] A three electrode arrangement is used, with separate reference and counter (CE) electrodes. The potential of the WE is adjusted

relative to the RE, but current only flows between the WE and the CE. The electrical mechanism by which this is achieved is described in chapter 3. This arrangement eliminates problems with the stability of the reference electrode as effectively zero current passes through it. However, the iR_s term may not be completely eliminated. If the RE is placed at any point other than at the electrode surface, some fraction of iR_s, called iR_u or the 'ohmic drop', where R_u is the 'uncompensated resistance', remains. Three methods are used to minimize the ohmic drop: first, by decreasing the path between the RE and the WE. A "good" cell design ensures that the separation between these two electrodes is minimized (within certain constraints). Second, the current transferred may be minimized. This is achieved using microelectrodes. Third, the resistance of the solution may be decreased by the addition of a large excess of supporting electrolyte. In addition, modern potentiostats often incorporate automatic electronic compensation for ohmic drop, which in simple cases is largely effective.

1.1.3 Contributions to the current

In general, two types of processes occur at electrodes. These are:

- Faradaic (or charge transfer) processes. In this case, charge is transferred across the electrode-solution interface, causing oxidation or reduction of electroactive species in solution. These reactions are governed by Faraday's law,

$$Q = zFN \tag{1.2}$$

  where Q is the amount of charge passed, N is the amount of substance converted by electrolysis, z is the number of electrons transferred per molecule and F is the Faraday constant.

- Nonfaradaic processes. An electrode-solution interface may display a range of potentials where no faradaic processes occur, because they are

kinetically or thermodynamically unfavourable. These are caused by processes such as adsorption/desorption and changes in the structure of the electrode-solution interface with changing potential. Such effects will cause transient external currents to flow when the potential, electrode area, or solution changes. Such effects are not governed by Faraday's law.

Faradaic processes are clearly of primary interest in most cases, as they provide information about the electroactive species. However, when an electrode process takes place, both faradaic and nonfaradaic processes occur: the effects of nonfaradaic processes must therefore be taken into account when examining voltammograms (although some workers suggest that the two types of process are inextricably linked).[3] Hence, we next examine the nature of the electrode-solution interface.

1.1.4 The electrical double layer

At the interfacial region, the electrostatic potential, Φ, changes from that in the bulk solution. In effect, ions in solution of an opposite charge to the electrode are attracted to it, and the electrode charge is neutralized to some extent.

The simplest model is that of Helmholtz,[4] in which the charge on the electrode produces a layer of oppositely charged ions from the solution, as illustrated in figure 1.1A. The interactions do not penetrate further into the solution. The charge neutralization is complete, and the double layer acts as a capacitor: the contact surface of the electrode acts as one plate, and the plane passing through the centres of the adsorbed ions the other. This model is incompatible with experimental observation. In particular it suggests that the capacitance of the double layer should be independent of potential, and does not take into account any dependence on electrolyte concentration.

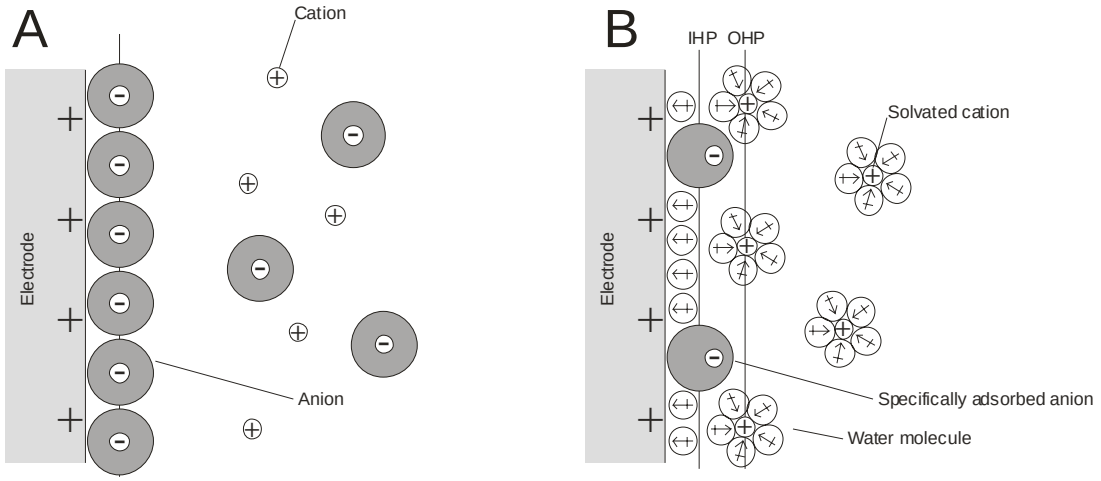

Figure 1.1: A) The Helmholtz model of the double layer. The line indicates the position of one plate of the equivalent capacitor. B) The Bockris, Devanathan and Müller model. The IHP and OHP designate the Inner and Outer Helmholtz Planes respectively.

The model of Helmholtz has been successively updated by Gouy[5] and Chapman,[6] Stern,[7] and Grahame.[8] The most recent classical model of the double layer was proposed by Bockris, Devanathan and Müller,[9] illustrated in figure 1.1B. This distinguishes between specifically adsorbed ions (in the inner Helmholtz plane), solvated but adsorbed ions (in the outer Helmholtz plane), and solvated ions outside the outer Helmholtz plane. It also includes treatment of the fact that a considerable amount of water will be adsorbed by the electrode due to its dipolar nature.

The most important non-faradaic process is the result of the capacitor-like structure of the double layer. In fact the electrode-solution interface may be experimentally characterized by the double layer capacitance, C_d. If a potential is applied to the interface, a current will flow as the double layer is charged; typical double layer capacitances for aqueous solutions are between 10-40 μFcm^{-2}. For a linear potential sweep, i_c, the charging current response (assuming the cell consists purely of a capacitor of capacitance C_d and a cell resistance, R_s, in series) is given by

$$i_c = \nu C_d \left(1 - e^{-t/R_s C_d}\right) \tag{1.3}$$

where v is the scan rate. This current response is illustrated in figure 1.2. It should be noted however, that in a real cell the value of C_d is generally a function of potential.

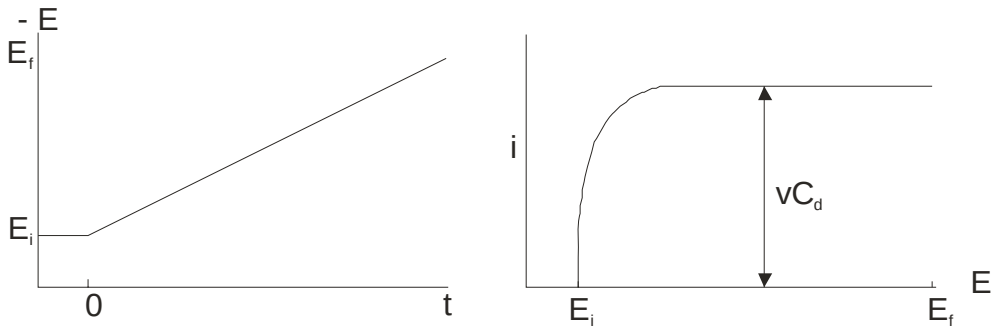

Figure 1.2: The charging current response to a linear potential sweep.

1.2 Mass Transport in Solution

Mass transport is the means by which electroactive species reach the electrode surface from the bulk solution. In the absence of any unusual processes, the faradaic current may be limited by either the rate of electron transfer, or the rate of transfer of the electroactive species from the bulk solution to the electrode surface. This distinction is particularly important when considering the modelling of metal nucleation; we therefore now consider the three processes by which mass transport occurs.

1.2.1 Diffusion

Diffusion results from the natural movement of species in solution, and is due to the presence of concentration gradients.[10] This is quantified by Fick's first law,[11] expressed here in one dimension:

$$J_i = -D_i \frac{\partial c_i}{\partial x} \tag{1.4}$$

where J_i is the flux for species i, $\frac{\partial c}{\partial x}$ is the concentration gradient in the direction x, and D is a proportionality constant called the diffusion coefficient. D is a function of solvent viscosity, temperature and electrolyte. Fick's second law expresses the variation of the concentration at a point as a function of time:

$$\frac{\partial c_i}{\partial t} = D_i \frac{\partial^2 c_i}{\partial x^2} \tag{1.5}$$

1.2.2 Migration

Migration is the motion of species due to potential gradients. Clearly it only affects charged species, and the flux due only to electrical effects is given by:

$$J_i = -z_i c_i \frac{F}{RT} \frac{\partial \Phi}{\partial x} \tag{1.6}$$

where R is the molar gas constant, T is the absolute temperature and z_i is the charge on the ion under consideration. In fact, the movement of migrating ions is retarded by three factors:[1]

- A frictional force, dependent on the size of the migrating ion.
- An asymmetric effect, whereby the movement distorts the ionic atmosphere of the ion.
- An electrophoretic effect, where ion movement causes a motion of solvent molecules in the opposite direction.

The overall rate of migration may be different for the cation and anion, and this results in a liquid junction potential.

Migration effects are usually undesirable in electrochemical experiments; varying the potential at the electrode alters the rate of migration and makes the interpretation of voltammetric data difficult. Hence migratory effects are usually minimized by using a

large excess of supporting electrolyte (≥0.1M).[12] The excess of non-electroactive species maintain electroneutrality during electrolysis, ensuring that electric field extends no further than the electrical double layer. In addition, as discussed earlier, using excess electrolyte has the effect of reducing ohmic drop effects in the cell.

1.2.3 Convection

Convection is the movement of the solution by mechanical forces. Natural convection, for example from temperature gradients in the solution, is undesirable as it is difficult to quantify. There are two solutions – first to do the experiment on a relatively short timescale, so that convection effects are negligible,[12] or second to swamp natural convection using some kind of well understood external agitation. Examples of this are stirring,[13] the use of flow cells,[14, 15] or the application of ultrasound.[16-19]

1.3 Electron Transfer

Electron transfer between the electrode and electroactive species (heterogeneous transfer) is the main factor other than rate of diffusion which is often rate determining. As an illustration of the principles involved, we consider the simple system:

$$A \rightleftharpoons B + e^-$$

At a given potential, the overall current for this process can be expressed as the sum of the oxidative and reductive currents:

$$i = FA\left(k_{ox}[B]_{electrode} - k_{red}[A]_{electrode}\right) \tag{1.7}$$

where A is the electrode area, k_{red} and k_{ox} are the first order heterogeneous rate constants for the reductive and oxidative electron transfers and $[B]_{electrode}$ and $[A]_{electrode}$ refer to the concentrations of B and A at the electrode surface. Using transition state theory, the two rate constants can then be expressed as a function of

two parameters: α, the charge transfer coefficient, and k_0, the standard heterogeneous charge transfer coefficient at E_f^0, where E_f^0 is the formal potential of the system vs. the reference electrode, defined by:

$$E_f^0 = E^0 + \frac{RT}{F}\ln\left(\frac{\gamma_A}{\gamma_B}\right) \tag{1.8}$$

where E^0 is the standard electrode potential of the system. The formal potential is used here instead of the standard potential to reflect the fact that real experiments are rarely performed under standard conditions.

The resulting expressions are:

$$k_{ox} = k_0 e^{\left\{(1-\alpha)\left(E-E_f^0\right)\frac{F}{RT}\right\}} \tag{1.9}$$

$$k_{red} = k_0 e^{\left\{-\alpha\left(E-E_f^0\right)\frac{F}{RT}\right\}} \tag{1.10}$$

These can then be substituted into equation (1.7) to give the Butler-Volmer equation:[20, 21]

$$i = FAk_0\left([A]_{electrode} e^{\left\{(1-\alpha)\left(E-E_f^0\right)\frac{F}{RT}\right\}} - [B]_{electrode} e^{\left\{-\alpha\left(E-E_f^0\right)\frac{F}{RT}\right\}}\right) \tag{1.11}$$

The term $\left(E-E_f^0\right)$ is the *overpotential, η*. The Butler-Volmer equation can be combined with equations for mass transport to give a theoretical treatment of the current response to the applied potential.

1.4 Voltammetric Methods

Two main analysis methods are considered: linear sweep/cyclic voltammetry, and potential step chronoamperometry.

1.4.1 Linear sweep voltammetry

In analogue linear sweep voltammetry, the applied potential is ramped linearly (although see chapter 3 for further details of the operation of a potentiostat) between two limit potentials, E_i and E_f, and the resulting current recorded. The scan rate is in the range mVs^{-1} to Vs^{-1} for many applications.

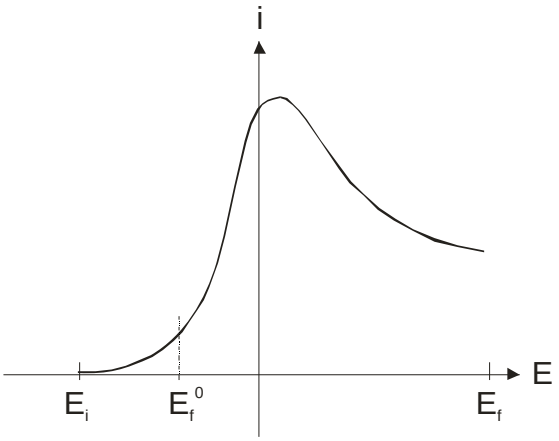

Figure 1.3: The current response of a $1e^-$ reduction to a linear potential sweep.

The purely capacitative current response to a potential sweep has been discussed above, and is illustrated in figure 1.2. Note that the resulting current is a function of the scan rate, v, and capacitance of the double layer, C_d. For a reversible $1e^-$ process $A + e^- \rightleftharpoons B$, the scan is of the form in figure 1.3 (assuming that the rate of electron transfer is fast compared to the potential scan rate; see below). The initial increase in current before E_f^0 is capacitative. At the potential E_f^0 reduction begins, generating a concentration gradient, and increasing diffusional flux towards the electrode. The surface concentration of A then decreases to almost zero, mass transfer reaches a maximum rate, and then declines as A is depleted. Note that in practice the capacitative component is minimized by the addition of excess inert electrolyte.

1.4.2 Cyclic voltammetry

Cyclic voltammetry (CV) is possibly the most commonly used method for investigating electrochemical systems. A ramped potential is applied, as in the previous section, then the scan direction is immediately reversed, giving a triangular scan of potential (figure 1.4).

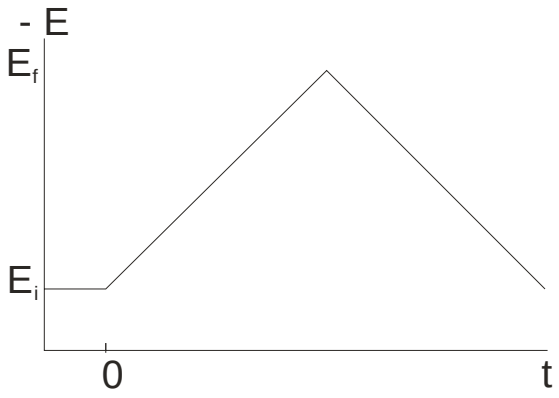

Figure 1.4: A triangular scan of potential.

Now consider the standard case in which the rate constant for the reaction is fast compared to the scan rate (a 'reversible' reaction). The concentration profile at the end of the forward scan shows a large concentration of oxidizable B at the electrode surface. The scan is immediately reversed: as E_f^0 is passed again, B is reoxidized, and the reverse peak has roughly the same shape (figure 1.5) as the forward peak, for much the same reason.

It is also important to consider the case in which the electron transfer reaction is slow compared to the rate of the potential sweep. Such reactions are known as 'quasi-reversible' or 'irreversible', depending on how exactly how slow the rate of electron transfer is.

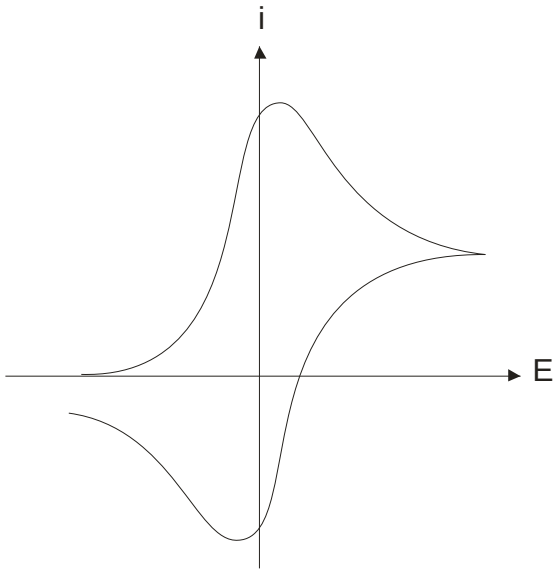

Figure 1.5: The current response of a reversible $1e^-$ reduction to a triangular potential sweep.

In this situation the voltage applied will not result in the generation of the concentrations at the electrode surface predicted by the Nernst equation. This happens because the equilibria are not established rapidly (in comparison to the voltage scan rate). In this situation the overall form of the voltammogram recorded is similar to that above, but unlike the reversible reaction now the position of the current maximum shifts depending upon the reduction rate constant. This occurs because the current takes more time to respond to the applied voltage than the reversible case. The effect of decreasing the reaction rate constant on a CV is illustrated in figure 1.6.

Despite the simplicity of the technique, CV is an effective way of investigating basic features of systems such as their approximate E_f^0 and reversibility.

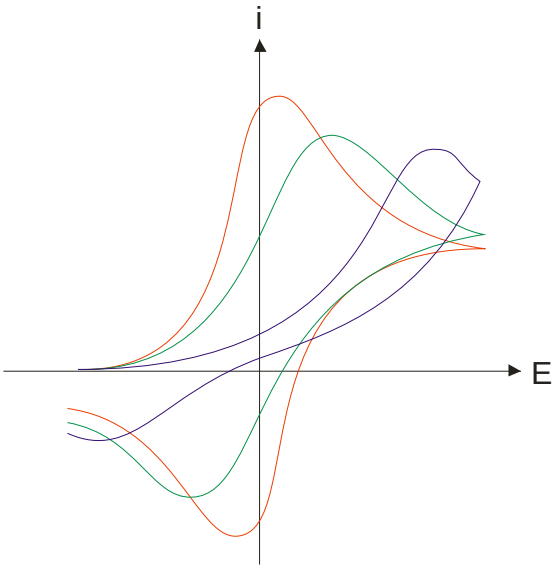

Figure 1.6: Cyclic voltammograms showing the effect of decreasing reaction reversibility. Red: reversible. Green to blue: decreasing reversibility.

1.4.3 Potential step chronoamperometry

As its name suggests, this technique involves stepping the applied potential instantaneously from E_i to E_f (figure 1.7A) and recording the current as a function of time. Typically, E_i is a potential at which no redox reaction occurs and E_f is a potential where oxidation/reduction does occur. The current response provides information about the mechanism of the processes occurring at the electrode, and will be extensively considered in the chapter 4.

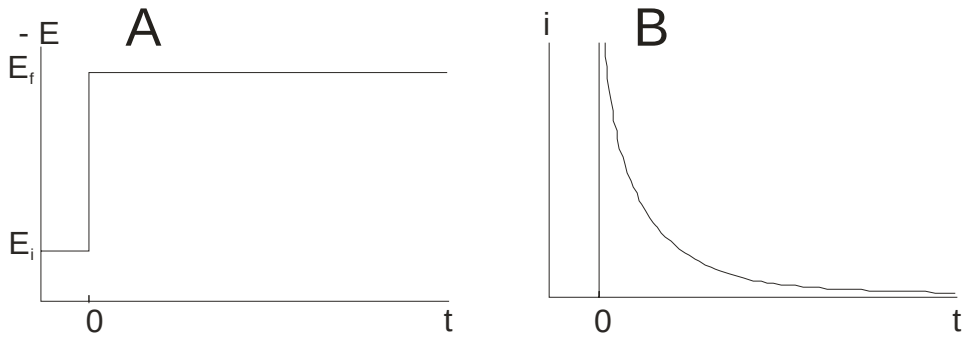

Figure 1.7: A) A single potential step. B) The current response according to the Cottrell equation.

Consider the simplest case, in which the one electron reduction $A + e^- \rightleftharpoons B$ occurs, and in which the system is under diffusion control. We initially observe a large current, the effect of capacitative currents and the concentration of A at the electrode being at a maximum (i.e. the concentration of A at the electrode is equal to the bulk concentration). The current then decays asymptotically to zero (figure 1.7B) according to the Cottrell equation,[22] assuming the electrode is planar:

$$|i| = \frac{zFA\sqrt{D}[A]_{bulk}}{\sqrt{\pi t}} \tag{1.12}$$

In this simple case we can obtain information on the diffusion coefficient of the species A. More complex reaction mechanisms may lead to chronoamperograms having more complex shapes. For example, many metal deposition processes show an initial maximum (if an appropriate potential is applied) before tending to Cottrell decay,[23] for reasons that are discussed in chapter 4. In addition, if the transport to the electrode is convection rather than diffusion controlled, we may see a monotonically rising transient, tending to a current maximum[24] (see chapter 7).

1.5 Types of Electrode

1.5.1 Microelectrodes vs. macroelectrodes

One definition of a microelectrode is an electrode which has its characteristic dimension on the scale of micrometres. Smaller electrodes may also be included in this category, or may be called ‘nanoelectrodes’ or ‘nanodes’. A macroelectrode is any electrode larger than a microelectrode, usually having a characteristic dimension on the scale of millimetres or centimetres.

Microelectrodes differ in their behaviour from macroelectrodes in several key ways:[25-27]

- Non-planar diffusion. Due to the increased current density at the edges of a microelectrode, they show convergent diffusion. This is illustrated in figure 1.8.

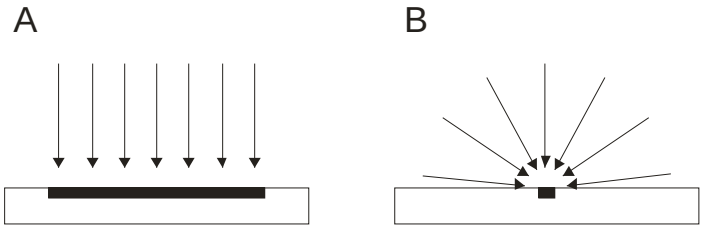

Figure 1.8: A) Linear diffusion to a macroelectrode. B) Convergent diffusion to a microelectrode.

  This effect increases the mass transport to the electrode, but has the additional effect that the electrodes are non-uniformly accessible. This means that the diffusion equation can no longer be reduced to a one-dimensional problem. This is relevant to the multiple nucleation of metals on electrodes, as each nucleus may be modelled as a growing hemisphere (see chapter 4).

- Reduced capacitance. The double layer capacitance is directly proportional to the area of the electrode.[1] Thus decreasing the area of the electrode immediately reduces the capacitance of the system.
- Reduced ohmic drop. The ohmic drop is proportional to the total current passed. The smaller electrode area decreases this current. However, reducing the total current passed also has a disadvantage in that more sensitive apparatus may be required to accurately measure it.

- Use in resistive media.[28] The combination of high current densities and low total currents permit the attainment of steady states in situations where this would be impossible with a macroelectrode.

An additional way to improve the performance of microelectrodes is to use a microelectrode array, in which a large number of microelectrodes are embedded in an insulating material, either as a regular array or a random assembly.[29] The electrodes are separated to a distance such that their diffusion layers do not overlap. This approach has the benefits of microelectrodes, but the total current is multiplied by the number of electrodes in the array, allowing for easier measurement. Another related approach is to use band electrodes, in which one dimension is on the micro- (or nano-) metre scale, while the other is orders of magnitude larger. Assemblies of nanobands are discussed further in chapter 11.

1.5.2 Hydrodynamic electrodes

Hydrodynamic electrodes employ some form of forced convection to improve rates of mass transport to the electrode. There are two methods for doing this: first, to flow solution across the electrode surface, or second to move the electrode itself, thereby inducing motion in the solution, as in a rotating disk electrode. The use of hydrodynamic methods has several advantages: steady state conditions are achieved rapidly, reducing problems with double layer charging currents. In a well designed system, the mass transport is entirely predictable and reproducible, simplifying modelling. Finally, the rate of mass transport may be altered simply by adjusting the flow rate or electrode rotation rate. Two types of hydrodynamic cell are employed in this thesis, both using flow rather than electrode motion.

A propeller cell is used to generate relatively low rates of mass transport. Electrochemical cells using stirring to agitate the solution are rarely employed for analytical work owing to the relative difficulty in rigorously modelling solution flow to the electrode compared to, for example, rotating disk electrodes (RDEs); however such cells are widely employed in practical metal plating. Another issue is the uniformity of the flow generated; it may be difficult to ensure that the electrode is uniformly accessible in the sense that the flux of electroactive species is the same to all parts of the electrode. On the other hand, it has been demonstrated that a carefully constructed stirred cell using a propeller can provide well defined mass transport to the electrode.[30] These issues are discussed further in chapter 7.

An impinging jet electrode is used where higher rates of mass transport are required. The flow in such an electrode is provided by an jet of electrolyte which strikes an electrode situated directly opposite the nozzle.[31] In such an electrode, two different flow regimes operate. Directly in front of the nozzle lies the 'stagnant region'.[32, 33] Outside this is the 'wall-jet' region in which the radial fluid velocity begins to decay.[34] In the limit where the electrode is entirely within the stagnant region, the electrode is uniformly accessible, with well understood flow characteristics. This specific situation is known as a wall tube electrode,[31] and is the type of impinging jet electrode employed in this thesis (see chapter 7).

1.6 References

[1] A. J. Bard, L. R. Faulkner, *Electrochemical Methods - Fundamentals and Applications*, 2nd ed., John Wiley & Sons, Inc., New York, **2001**.

[2] J. C. Eklund, A. M. Bond, J. A. Alden, R. G. Compton, *Adv. Phys. Org. Chem* **1999**, 1.

[3] C. P. Andrieux, P. Hapiot, J. M. Saveant, *Chem. Rev.* **1990**, *90*, 723.

[4] H. L. F. von Helmholtz, *Ann. Physik* **1853**, 211.

[5] G. Gouy, *J. Physique* **1910**, *9*, 457.

[6] D. L. Chapman, *Phil. Mag.* **1913**, *25*, 475.
[7] O. Stern, *Z. Elektrochem.* **1924**, *30*, 508.
[8] D. C. Grahame, *Chem. Rev.* **1947**, *41*, 441.
[9] J. O. Bockris, M. A. Devanathan, K. Müller, *Proc. R. Soc.* **1963**, 55.
[10] J. O. Bockris, A. K. N. Reddy, M. Gamboa-Aldeco, *Modern Electrochemistry 2A: Fundamentals of Electrodics*, 2nd ed., Plenum, New York, **2000**.
[11] A. Fick, *Phil. Mag.* **1855**, 30.
[12] K. B. Oldham, C. G. Zoski, in *Electrode kinetics : principles and methodology, Vol. 26* (Eds.: B. C.H., C. R.G.), Elsevier, Oxford, **1986**, p. 79.
[13] K. Scott, *Journal of Applied Electrochemistry* **1991**, *21*, 945.
[14] K. Toth, K. Stulik, W. Kutner, Z. Feher, E. Lindner, *Pure and Applied Chemistry* **2004**, *76*, 1119.
[15] D. T. Schwartz, *Proceedings - Electrochemical Society* **1995**, *95-11*, 200.
[16] C. E. Banks, R. G. Compton, *Electroanalysis* **2003**, *15*, 329.
[17] A. J. Saterlay, R. G. Compton, *Fresenius' Journal of Analytical Chemistry* **2000**, *367*, 308.
[18] R. G. Compton, J. C. Eklund, F. Marken, T. O. Rebbitt, R. P. Akkermans, D. N. Waller, *Electrochimica Acta* **1997**, *42*, 2919.
[19] R. G. Compton, J. C. Eklund, F. Marken, *Electroanalysis* **1997**, *9*, 509.
[20] J. A. V. Butler, *Trans. Faraday Soc.* **1924**, *19*, 734.
[21] T. Erdey Gruz, M. Volmer, *Z. Phys. Chem.* **1930**, *150A*, 203.
[22] F. G. Cottrell, *Z. Phys. Chem.* **1902**, *42*, 385.
[23] B. Scharifker, G. Hills, *Electrochim. Acta* **1983**, *28*, 879.
[24] M. E. Hyde, O. V. Klymenko, R. G. Compton, *Journal of Electroanalytical Chemistry* **2002**, *534*, 13.
[25] J. Heinze, *Angew. Chem., Int. Ed.* **1993**, *32*, 1268.
[26] P. Delahay, *Double Layer and Electrode Kinetics*, Wiley-Interscience, New York, **1965**.
[27] J. Koryta, *Principles of Electrochemistry*, Wiley, London, **1987**.
[28] C. M. A. Brett, A. M. O. Brett, *Electrochemistry - Principles, Methods, and Applications*, Oxford University Press, Oxford, **1993**.
[29] S. Fletcher, in *Microelectrodes: Theory and Applications* (Eds.: M. I. Montenegro, M. A. Queiros, J. L. Daschbach), Kluwer Academic Publishers, Dordrecht, **1991**, pp. 341.
[30] L. N. Nekrasov, T. N. Khomchenko, V. N. Alekseev, B. M. Grafov, S. A. Martem'yanov, *Russ. J. Electrochem.* **1999**, *35*, 966
[31] D. T. Chin, C.-H. Tsang, *J. Electrochem. Soc.* **1978**, *125*, 1461.
[32] Z. J. Karpinski, R. A. Osteryoung, *J. Electroanal. Chem.* **1993**, *349*, 285.
[33] M. V. Mirkin, T. C. Richards, A. J. Bard, *J. Phys. Chem.* **1993**, *97*, 7672.
[34] M. B. Glauert, *J. Fluid. Mech.* **1996**, *1*, 625.

2 Carbon Electrodes

A wide variety of carbon electrodes are available, with correspondingly varied properties. All of the major experiments described in this thesis were performed on carbon electrodes of one form or another, specifically glassy (or vitreous) carbon, boron-doped diamond and highly ordered pyrolytic graphite (HOPG). These types of carbon are described in detail in this section.

2.1 Glassy Carbon

The precise method of manufacture of glassy carbon is proprietary. However, in outline, the process is as follows:[2]

1. Mould the required shape out of a suitable polymer, for example dry or liquid phenol formaldehyde resin.
2. Thermally treat the resin to convert it to glassy carbon. This process may take up to several months depending on the size of the final object. The exact properties of the glassy carbon product depend on the details of this step: higher curing temperatures give a softer, less dense result, but with a higher thermal conductivity.

The result is a form of carbon which is completely amorphous: x-ray diffraction reveals no peaks at all, only an ‘amorphous halo’. This should be contrasted with graphite, which gives strong peaks indicating a high degree of order and crystallinity.[3]

2.1.1 Physical properties

Glassy carbon has a number of unusual properties compared to graphite.

- Density. Glassy carbon has a density of roughly 1.5 g cm^{-3} (depending on the details of manufacture). This is higher than a typical graphite sample (excluding HOPG, which may achieve close to the theoretical density of a perfect graphite crystal, approximately 2.25 g cm^{-3}), indicating a less porous structure.
- Thermal properties. Glassy carbon has a relatively good thermal conductivity; it is therefore resistant to thermal shock. It is also extremely stable: it may be heated to approximately 2500 °C in an inert atmosphere before conversion to a graphite phase begins.
- Chemical resistance. In theory, glassy carbon should have a chemical reactivity similar to graphite. In practice it is much less reactive, a result of its high density non-porous structure, and is highly resistant to commonly used electrochemical compounds including nitric, hydrochloric and sulfuric acids and caustic alkalis.

2.1.2 Structure

The structure of glassy carbon has been debated since it was first produced in the 1960s. A commonly used model, suggested by Jenkins et al.,[1, 4, 5] states that the molecular orientation of the resinous precursor is retained to some extent after carbonization. The structure is therefore similar to that of a polymer, having interlocking, twisted 'fibrils' of graphitic carbon. This is illustrated in figure 2.1. There are, however, some objections to this model. Such an open structure, consisting of many conjoined pores, might be expected to be gas-permeable, when in fact glassy carbon is highly gas-impermeable.[2] In addition, the structure shown in figure 2.1 has a high proportion of edge plane graphite. This is highly reactive compared to basal

plane graphite,[6, 7] and probably inconsistent with the notably low chemical reactivity of glassy carbon.

Recently, Harris and others[8-14] have demonstrated using transmission electron microscopy (TEM) that glassy carbon contains tightly curled single carbon layers (‘graphene sheets’) which enclose pores having a size of the order of 1 nm (depending on the specific manufacturing conditions). Harris and Tsang[12, 15] propose that the structure consists of fragments of curved carbon sheets (similar to fullerenes), illustrated schematically in figure 2.2. They suggest that increasing the curing temperature increases the size of the continuous graphene sheets and the size of the pores (resulting in reduced density). In this model the low reactivity of glassy carbon is explained by either a high proportion of closed fullerene-like particles or a tightly packed microstructure.

The diagram originally presented here cannot be made freely available via ORA because of copyright. Please see reference [1] for the diagram.

Figure 2.1: The Jenkins-Kawamura model of glassy carbon showing interlocking graphitic domains. Blue shows basal plane graphite, green edge plane.[1]

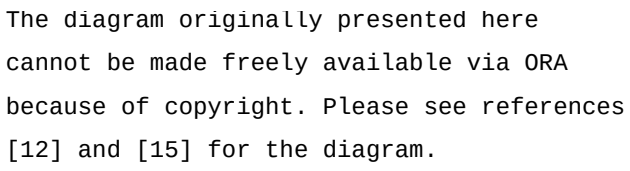

Figure 2.2: Harris's model for the structure of glassy carbon.

The glassy carbon electrodes used in the experiments described in this thesis were based on 3mm glassy carbon rod ('type 1', a low temperature cured form manufactured by Alfa Aesar). The rod was pressed into a PTFE housing and attached to a connector using silver loaded epoxy resin. As produced, glassy carbon has no well defined surface structure. It was therefore prepared for use as an electrode by mechanical polishing to a mirror finish using successively smaller grades of diamond polishing compound (Kemet) down to a grade of 1μm. Examination of the resulting surface using AFM shows that although homogeneous on a large scale, there is a network of scratches covering the surface, which has a mean roughness of approximately 30 nm (figure 2.3). This small scale irregularity makes it less suitable for AFM studies as it is more difficult to distinguish deposit from the background.[16] The use of glassy carbon electrodes in this thesis is therefore limited to applications in which accurate analysis using AFM is not required; further details of the treatment of the electrodes are given in the relevant chapters.

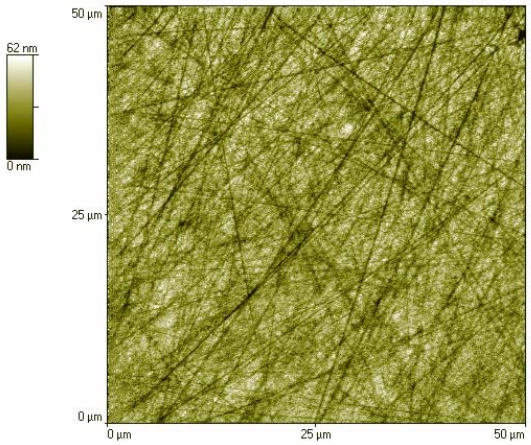

Figure 2.3: Large-scale AFM image of a freshly polished glassy carbon surface.

2.2 Boron-Doped Diamond (BDD)

Diamond as an electrode material has become increasingly popular owing to the unique properties of diamond.[17] These include extreme hardness, chemical inertness, and high thermal conductivity. Clearly pure diamond is also an excellent insulator; it is therefore doped (typically with boron) for applications in which conductivity is required. Diamond thin films can possess electronic properties ranging from insulator to semiconductor to semimetal depending on the level of doping.[18, 19] This behaviour occurs as the boron dopant atoms (electron acceptors) form a band approximately 0.35 eV above the valence band.[20] At room temperature the thermal energy is sufficient to promote some of the valence band electrons to the boron acceptors, resulting in free electrons in the dopant band and holes in the valence band.

2.2.1 BDD film generation

BDD film electrodes are grown using chemical vapour deposition (CVD).[2] This general method is illustrated in figure 2.4.[21] There are two main methods for activation of the gas mixture in the chamber. The hot filament method involves

heating a wire in the chamber to around 2100 °C in order to generate the atomic hydrogen while microwave discharge at a power of 1000-1300 W achieves the same result.[18, 19] In addition to generating the $CH_3^{\cdot}$ the atomic hydrogen is critical to the successful growth of diamond films for several other reasons: it prevents surface reconstruction from a diamond to a graphite microstructure during deposition, suppresses the formation of other non-diamond impurities and abstracts hydrogen from hydrocarbon surface sites.[22, 23]

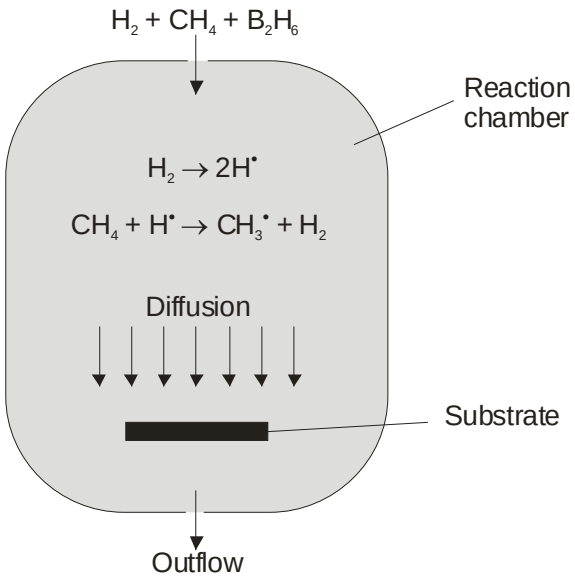

Figure 2.4: CVD method for growing BDD films.

Boron doping is usually accomplished by mixing B_2H_6 (or a similar boron-containing gas) with the source gases,[24] allowing doping levels as high as 10^4 ppm boron in the resulting film,[17] resulting in resistivities of less than 0.1 Ωcm.

2.2.2 Electrochemical properties

Highly boron-doped diamond electrodes (i.e. those doped close to the limit of 10^4 ppm) have a number of properties making them particularly interesting for certain electrochemical applications:

- Chemical inertness. Diamond may be used in a range of harsh environments. In addition it is biologically inactive under most experimental conditions; it is therefore potentially suitable for use in biological experiments.[25]
- Diamond is transparent over a wide spectral range (from ultraviolet to far infrared, depending on impurities). This allows simultaneous electrochemical and spectroscopic studies.
- The high thermal conductivity of diamond (20 W cm^{-1} K^{-1}) allows precise temperature control at the surface of the electrode.
- Diamond has a particularly wide potential window: up to 4.7 V in aqueous acid and 4.1 V in aqueous base,[26-28] allowing a wider range of electrochemical experiments to be performed.[24, 29, 30]
- Low background currents and double layer capacity: with BDD electrodes these may be up to an order of magnitude smaller than glassy carbon.[31]

Xu et al.[17] suggest that the factors responsible for the last two points may include an absence of electroactive carbon-oxygen groups on the surface and a low density of surface electronic states near the Fermi level (a result of the semimetal nature of BDD).

The diamond electrodes used in the experiments described in this thesis were supplied by Element 6 (formerly De Beers Industrial Diamond Division) as 5 x 5 x 0.53 mm square plates, with the diamond deposited on to a graphite substrate. The total resistance of each film was found to be approximately 0.4 Ω. The films were pre-polished, and were found to be extremely flat, having a roughness of approximately 1.5 nm over a 5 x 5 μm area.[16] This flatness, combined with the hardness of

diamond, provides an extremely favourable surface for AFM studies of deposition: even very small deposits may be easily resolved from the background. The electrodes were made by pressing the BDD plate in to a PTFE mounting and attaching a connection to the reverse (graphite) layer using silver loaded epoxy resin. Before each experiment, the electrode was polished using 1 μm alumina powder to remove any adherent deposits, then rinsed thoroughly.

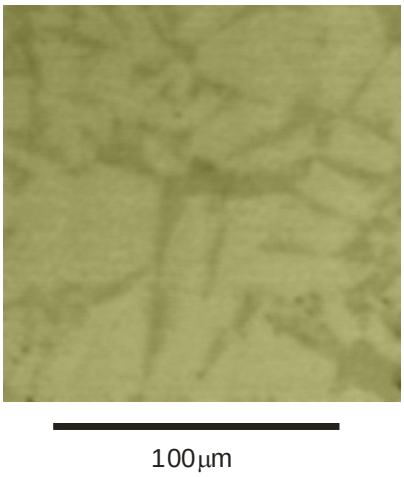

Figure 2.5: Optical microscopic image of a clean BDD electrode.

Although it is possible to generate single crystals of diamond by carefully controlling the CVD conditions, the diamond electrodes used in this thesis are polycrystalline. An optical microscopic image of the surface (figure 2.5) reveals irregular domains having sizes of the order of 50 μm. In fact we have found that the light and dark domains visible in the figure have a somewhat differing conductivity; one possible reason for this is the presence of some non-diamond impurity at the grain boundaries of individual crystals. This property of the electrode means that AFM experiments performed on such a surface should either be repeated at several points or collected at a large scan range in order to fully understand the deposition processes occurring.

2.3 Highly Ordered Pyrolytic Graphite (HOPG)

HOPG is a relatively new form of high-purity carbon, having a structure and density close to that of a hypothetical perfect graphite crystal.

2.3.1 Manufacture

As with the other carbon materials discussed, the precise method of manufacture of HOPG is proprietary. There are several variations, but in essence the following process is used.[32] Initially, CVD is used in a manner very similar to that for generating diamond. Typically, methane or a similar simple hydrocarbon is pyrolyzed at 1000 °C and reduced pressure, with the following (simplified) reaction scheme taking place:

$$\text{Methane} \rightarrow \text{Benzene} \rightarrow \text{Polyaromatic hydrocarbons} \rightarrow \text{Carbon} \qquad (2.1)$$

A common method for achieving the pyrolysis is to use a ‘cold wall’ reactor, in which no furnace is required as the substrate is heated directly. In this case, the substrate (usually a graphite disk) is heated by a high frequency induction coil. All the decomposition reactions in scheme (2.1) are endothermic, so deposition occurs preferentially on the hottest surfaces in the reaction chamber, i.e. the substrate, while the chamber walls remain uncoated.

The result of this process is so-called pyrolytic graphite. This is an aggregate of graphite crystallites, usually with many warped basal planes, lattice defects and other crystallite imperfections. The pyrolytic graphite is then annealed at 2700 °C under elevated pressure. This heat treatment causes the re-ordering of the structure: the basal planes coalesce and become more parallel, the crystallite imperfections tend to disappear, and the interlayer spacing decreases towards that of an ideal graphite

crystal. This last effect is attributed to the removal of interstitial carbon residue. The result of this annealing process is HOPG.[2]

2.3.2 Properties

HOPG consists of a lamellar structure, similar to mica. Unlike mica however, it is completely non-polar. Carbon atoms within a single plane interact much more strongly than with those in adjacent planes (figure 2.6), resulting in HOPG's characteristic cleaving properties.[33] The simplest cleaving approach is to press a piece of adhesive tape on to the surface of the HOPG block, then remove it. A thin layer of graphite is removed with the adhesive, leaving a freshly cleaved surface.[34]

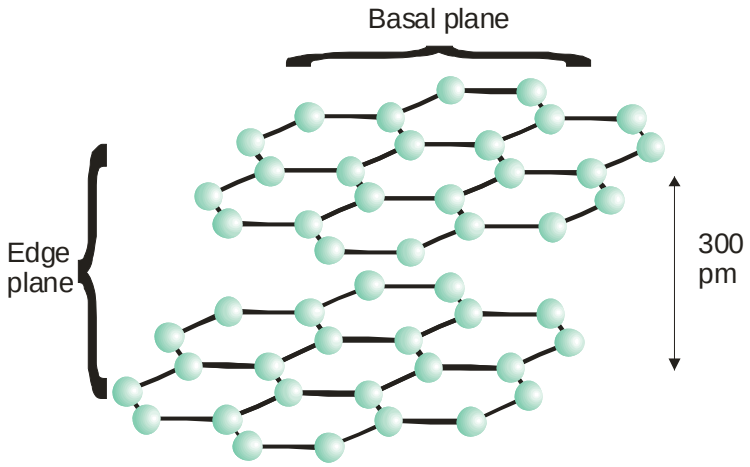

Figure 2.6: The structure of graphite

The basal planes of HOPG are unusually easy to image using "atomic resolution" STM, owing to its high conductivity and extremely regular structure. The image usually looks like a close packed array with a centre to centre atomic distance of 246 pm, rather than the true 'chicken wire' structure with a centre to centre atomic distance of around 142 pm.[35, 36] This has been explained as the effect of the underlying graphite sheet on the molecular orbitals of the top layer. Essentially,

certain carbon atoms interact with the layer below, forming bonding and antibonding orbitals. These bonding and antibonding orbitals no longer lie at the Fermi level, and no tunnelling to them can occur. This effect is discussed in more detail by various authors.[37-39] Such an image of the piece of HOPG used in the experiments described in this thesis is shown in figure 2.7.

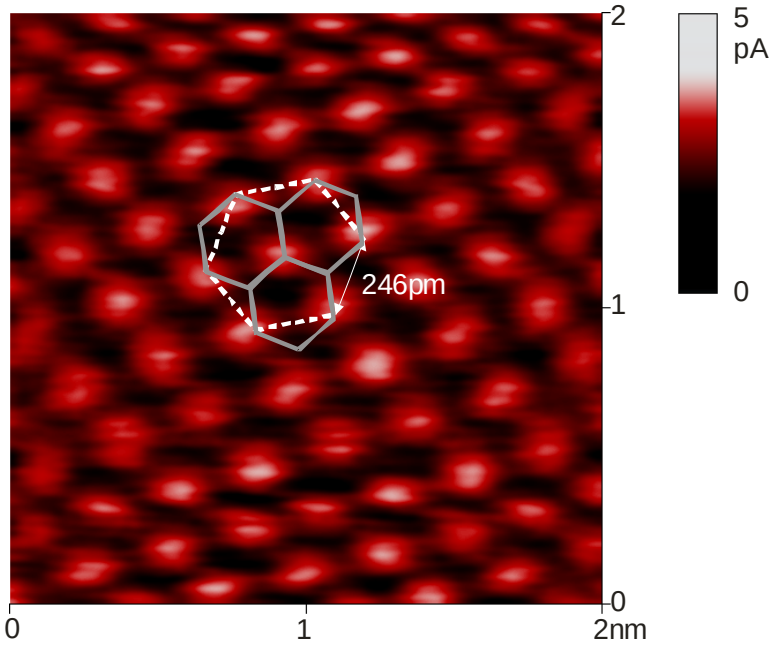

Figure 2.7: Atomic resolution (constant height) STM image of HOPG showing the apparent HCP structure (white). Actual positions of graphite atoms are shown in grey.

HOPG is commercially available in three grades, the quality of which are defined by two properties: the roughness/grain size and the mosaic spread. It has a polycrystalline structure, with the size of the crystals varying from tens of nanometres up to hundreds of micrometres or greater. A freshly cleaved surface consists of atomically flat planes with atomic steps (340 pm or multiples thereof) at the boundaries. Thus, larger crystal sizes result in a flatter surface. The mosaic spread is a measure of the disorientation of adjacent crystals; originally derived from X-ray crystallography, it is measured in degrees, with a smaller mosaic spread indicating a

more perfect surface. One of the higher two grades were used in all experiments involving HOPG described in this thesis; the properties of these are summarized in table 2.1.

Table 2.1: Properties of commercially available HOPG.

HOPG grade (SPI)*	HOPG grade (Advanced Ceramics)	Grain size	Mosaic spread
SPI-1	ZYA	≤ 3mm	0.4° ± 0.1°
SPI-2	ZYB	≤ 0.5mm	0.8° ± 0.2°

In addition HOPG has some properties similar to the other speciality types of carbon discussed. It is highly chemically inert (particularly when only the basal plane is exposed), again the result of a high density and low porosity. It has a high electrical and thermal conductivity, although these differ along the directions of the basal and edge planes, and it has an excellent resistance to heating.

2.3.3 Use of HOPG as an electrode material

The relationship between surface structure and electrochemical performance is of fundamental importance in electrochemistry and highlights the need for electrodes with well defined surfaces. For this reason, basal plane highly ordered pyrolytic graphite (HOPG) is an attractive electrode material. Because the surface is so well defined, HOPG has proved to be a popular surface on which to conduct electrodeposition experiments. Even more promising is the potential application in nanotechnology: a number of groups have reported the synthesis of nanowires and

* HOPG may be purchased from SPI Supplies (Structure probe Inc, West Chester, PA, USA. www.2spi.com) or Advanced Ceramics (a division of General Electric, www.advceramics.com). The quality of both materials is similar, but they are manufactured using different proprietary processes.

nanoribbons along edge plane steps. This application is discussed further in chapter 11.

However, the nature of HOPG also causes some practical difficulties. It is expensive, has a delicate surface, and until recently was only available in square sheets. The fact that it is cleaved rather than polished may also cause mounting problems as the thickness of the HOPG block decreases over time. In chapter 9 we discuss a novel electrode housing designed specifically to overcome these problems and to allow easy analysis of the block using techniques such as AFM.

2.4 References

[1] G. M. Jenkins, K. Kawamura, *Nature* **1971**, *231*, 175.
[2] H. O. Pierson, *Handbook of Carbon, Graphite, Diamond and Fullerenes*, Noyes Publications, New Jersey, **1993**.
[3] https://secure.2spi.com/catalog/mounts/vitreous.html.
[4] G. M. Jenkins, K. Kawamura, *Polymeric Carbons - Carbon Fibre, Glass and Char*, Cambridge University Press, Cambridge, **1976**.
[5] G. M. Jenkins, K. Kawamura, L. L. Ban, *Proc. Roy. Soc. A* **1972**, *327*, 501.
[6] C. E. Banks, T. J. Davies, G. G. Wildgoose, R. G. Compton, *Chem. Commun.* **2005**, 829.
[7] T. J. Davies, R. R. Moore, C. E. Banks, R. G. Compton, *J. Electroanal. Chem.* **2004**, *574*, 123.
[8] P. J. F. Harris, *Int. Mater. Rev.* **1997**, *42*, 206.
[9] P. J. F. Harris, *Carbon Nanotubes and Related Structures*, Cambridge University Press, Cambridge, **1999**.
[10] P. J. F. Harris, *Chemistry and Physics of Carbon, Vol. 28*, Marcel Dekker, New York, **2003**.
[11] P. J. F. Harris, A. Burian, S. Duber, *Phil. Mag. Lett.* **2000**, *80*, 381.
[12] P. J. F. Harris, S. C. Tsang, *Phil. Mag. A* **1997**, *76*, 667.
[13] A. Burian, J. C. Dore, *Acta. Phys. Polon. A* **2000**, *98*, 457.
[14] A. Burian, A. Szczygielska, J. Koloczek, J. C. Dore, V. Honkimaki, S. Duber, *Acta Phys. Polon. A* **2002**, *101*, 751.
[15] P. J. F. Harris, *Phil. Mag.* **2004**, *84*, 3159.
[16] M. E. Hyde, Part II thesis, University of Oxford **2002**.
[17] J. Xu, M. C. Granger, Q. Chen, J. W. Strojek, T. E. Lister, G. M. Swain, *Anal. Chem.* **1997**, *69*, 591.
[18] J. C. Angus, C. C. Hayman, *Science* **1988**, *241*, 913.
[19] A. Argoitia, J. C. Angus, J. S. Ma, L. Wang, P. Pirouz, W. R. L. Lambrecht, *J. Mater. Res.* **1994**, *9*, 1849.

[20] W. J. P. van Enckevort, in *Synthetic diamond: emerging CVD science and technology* (Eds.: K. P. Spear, J. P. Dismukes), John Wiley & Sons, New York, **1994**.
[21] A. Yarnell, *Chem. and Eng. News* **2004**, *82*, 26.
[22] J. R. Dennison, M. W. Holtz, G. M. Swain, *Spectroscopy* **1996**, *10*, 38.
[23] W. J. P. van Enckevort, in *Synthetic Diamond: Emerging Science and Technology* (Eds.: K. E. Spear, J. P. Dismukes), John Wiley and Sons, New York, **1994**.
[24] N. Vinokur, B. Miller, Y. Avyigal, R. Kalish, *J. Electrochem. Soc.* **1996**, *143*, L238.
[25] E. Fortin, J. Chane-Tune, D. Delabouglise, P. Bouvier, T. Livache, P. Mailley, B. Marcus, M. Mermoux, J.-P. Petit, S. Szunerits, E. Vieil, *Electroanalysis* **2005**, *17*, 517.
[26] R. G. Compton, J. S. Foord, F. Marken, *Electroanalysis* **2003**, *15*, 1349.
[27] I. Gerger, R. Haubner, *Diamond and Related Materials* **2005**, *14*, 369.
[28] I. Gerger, R. Haubner, H. Kronberger, G. Fafilek, *Diamond and Related Materials* **2004**, *13*, 1062.
[29] H. B. Martin, A. Argoitia, U. Landau, A. B. Anderson, J. C. Angus, *J. Electrochem. Soc.* **1996**, *143*, L133.
[30] Q. Chen, M. C. Granger, T. E. Lister, G. M. Swain, *J. Electrochem. Soc.* **1997**, *144*, 3806.
[31] S. Alehashem, F. Chambers, J. W. Strojek, G. M. Swain, R. Ramesham, *Anal. Chem.* **1995**, *68*, 2031.
[32] H. O. Pierson, *Handbook of Chemical Vapor Deposition*, Noyes Publications, New Jersey, **1992**.
[33] B. T. Kelly, *Physics of graphite*, Applied Science, London, **1981**.
[34] https://secure.2spi.com/catalog/new/hopgsub.shtml.
[35] T. Tiedje, J. Varon, H. Deckman, J. Stokes, *Journal of Vacuum Science & Technology, A: Vacuum, Surfaces, and Films* **1988**, *6*, 372.
[36] I. P. Batra, S. Ciraci, *Journal of Vacuum Science & Technology, A: Vacuum, Surfaces, and Films* **1988**, *6*, 313.
[37] H. A. Mizes, W. A. Harrison, *J. Vac. Sci. Technol. A* **1988**, *6*, 300.
[38] I. P. Batra, N. Garcia, H. Rohrer, H. Salemink, E. Stoll, S. Ciraci, *Surf. Sci.* **1987**, *181*, 126.
[39] D. Tomanek, S. G. Louie, H. J. Mamin, D. W. Abraham, R. E. Thomson, E. Ganz, J. Clarke, *Phys. Rev. B* **1987**, *35*, 7790.

3 Instrumentation

This chapter introduces the experimental equipment upon which all the experiments in this thesis are based. More specialized equipment, used only for particular experiments, is described in the appropriate chapters.

3.1 Chemicals

All reagents used were of analytical grade, and used without further purification. All aqueous solutions were prepared using water with a resistivity of not less than 18 MΩ cm, using an Elgastat (Elga, Bucks, UK) UHQ grade water purification system. The specific chemicals used for each set of experiments will be given in the relevant chapter.

3.2 Electrochemical Equipment

As outlined in chapter 1, a potentiostat is fundamentally an electronic device that controls the potential difference between a working electrode and a reference electrode. This control is achieved by supplying current into the cell through a counter (or 'auxiliary') electrode.

3.2.1 Potentiostat operational principles

A simplified block diagram of a typical potentiostat is shown in figure 3.1.[1] All parts of this circuit are analogue: in practice the output voltage and output (current * R_m) are sent to an analogue to digital (A/D) converter to allow interface with a computer. Also, the signal generator is usually a digital to analogue (D/A) converter receiving signals from the controlling computer. This gives great flexibility in the waveforms that may be applied. However, the output of the signal generator is a discrete

approximation of any continuous waveform. The size of the potential steps is dependent on the resolution of the D/A converter; it is important that the potential steps are set small enough such that the resulting waveform is a good approximation to an analogue ramp.

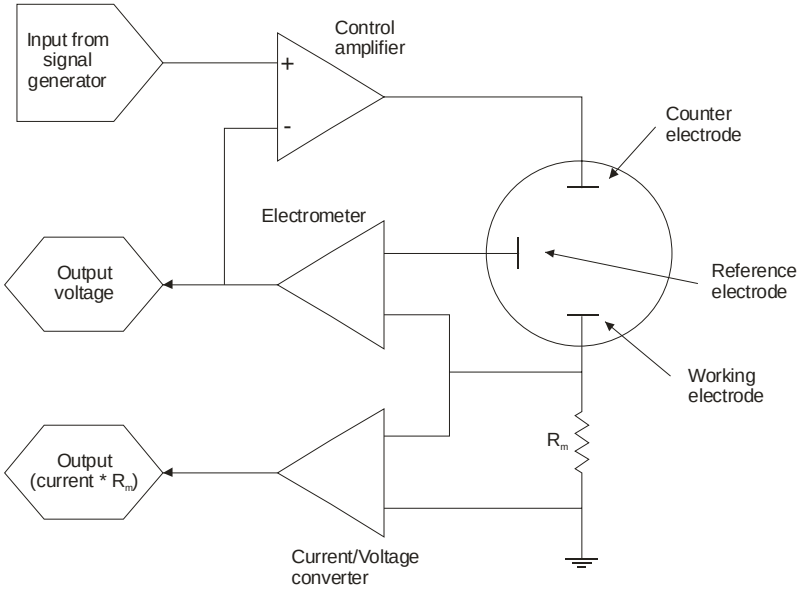

Figure 3.1: Simplified block diagram of a potentiostat

The critical components of the potentiostat are the three amplifiers (represented by triangular blocks in the diagram):

- **The electrometer.** The electrometer is a unity gain differential amplifier: the output voltage of the block is the voltage difference between its two inputs. In the potentiostat circuit it measures the potential difference between the working electrode and reference electrode. This has a dual purpose: it measures the cell voltage for output to the computer and also provides feedback to the control amplifier (discussed below).

Current flow through a reference electrode can change its potential (particularly in the case of quasi-reference electrodes), so ideally, the electrometer should have zero input current and an infinite impedance. In practice, modern electrometers have high enough impedances that this can be ignored in most applications.

- **The current to voltage (I/E) converter.** This component is also a unity gain differential amplifier. It measures the cell current: the current from the working electrode flows through the measurement resistor, R_m, and applying Ohm's law, the voltage drop may be directly related to the cell current. For accurate measurement, again the amplifier should have the highest possible input impedance.

  Typically a modern potentiostat will have a measurable current range from 100 nA to 10 mA or greater. A single resistor is unsuitable for accurate measurement across such a wide range, so in practice a computer controlled system is usually used which allows an R_m with an appropriate resistance to automatically be switched into the circuit.

- **The control amplifier.** This component compares the measured potential difference between the reference and working electrode with the input voltage from the signal generator and drives the current at the counter electrode to minimize the difference between the two inputs. Note that the measured cell potential is connected to the inverting input of the control amplifier (i.e. a positive perturbation in the cell potential causes a negative

perturbation in the output), thus maintaining an accurate cell potential using a negative feedback loop. The maximum potential/current that can be applied to the cell is defined by the capabilities of the control amplifier.

3.2.2 Apparatus

All electrochemical measurements recorded in this thesis were recorded using an Eco-Chemie μAutolab Type II potentiostat, having a current sensitivity range of 10 nA to 10 mA, and a maximum output of ±5 V and/or 10 mA. Cyclic voltammograms were recorded in staircase mode, with the step potential set to a maximum 150 μV to accurately approximate an analogue linear sweep.

In all experiments, a standard three electrode configuration was used. In all cases, the counter electrode was a coiled platinum wire, cleaned using conc. HNO_3 and rinsed thoroughly before use. Details of the reference and working electrodes employed for each experiment are described in the appropriate chapters.

3.3 Atomic Force Microscopy

3.3.1 SPM scanner operation

AFM, like other similar technologies such as scanning tunnelling microscopy (STM), is classified as a scanning probe technique (SPM); the feature uniting these techniques is the presence of a sharp probe or tip which at the beginning of the measurement is brought close to the surface of the material to be investigated, so that the tip may physically interact with the surface.

SPM operates by moving a sample mounted on a piezoelectric tube relative to a stationary probe. Modern SPMs use a single tube of layered piezoelectric material. Eight electrodes are distributed radially around the tube, and two more attached to the upper walls of the tube. This arrangement is illustrated in figure 3.2. By applying appropriate control potentials to these electrodes, the tube can be made to distort in such a way that the position of a sample attached to the top of the tube may be controlled in three dimensions.*

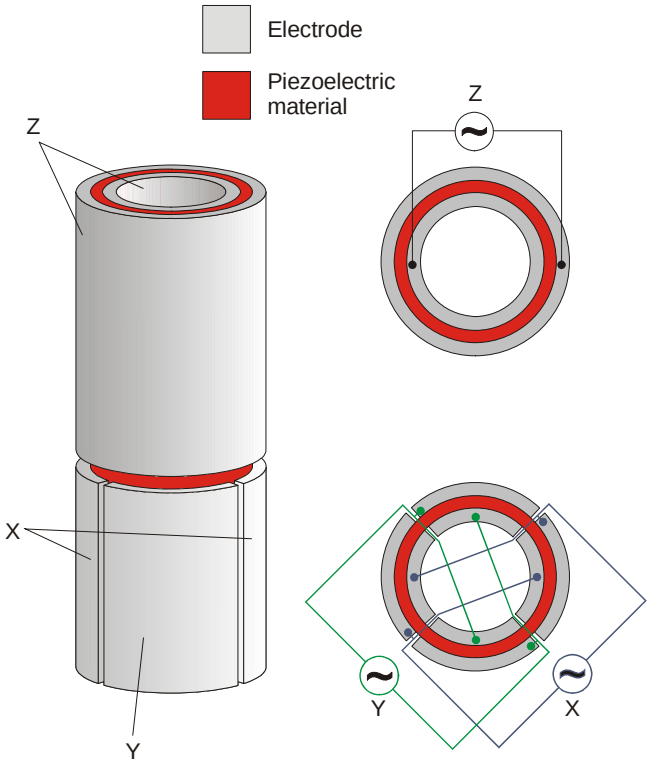

Figure 3.2: Typical scanner piezo tube and electrode configuration

* In fact the tube bends in the x-y directions, but in practice the scan range is usually small enough for the non-linearity to be negligible: the three degrees of freedom are essentially independent. At large scan ranges some correction may be required, but the non-linear response of the piezoelectric elements is usually a more important factor.

A typical piezoelectric material will expand by about 1 nm per applied volt. Thus, to get larger motions it is necessary to make piezoelectric transducers with hundreds of layers of piezoelectric materials. By using one thousand layers of piezoelectric material it is possible to get motions as large as 1000 nm per volt. Thus with 100 volts it is possible to get 0.1 mm of motion with a multiple layer piezoelectric transducer. It is important to note that the response of the piezoelectric transducer is complicated by several factors:

- The response of the piezoelectric element is non-linear with respect to voltage by the nature of the material from which it is made (often a kind of lead zirconate titanate ceramic, or PZT). The material also displays hysteresis; the response of the tube to a decreasing potential is not the same as the response to an increasing potential. The software controlling the SPM corrects for these effects by modelling the scanner's sensitivity curve across its full range and attempting to apply suitable non-linear potentials. This is illustrated for a simple case in figure 3.3. Although usually effective, this correction may fail, particularly at large scanner offsets, resulting in image distortion.

- As the scanner ages, its sensitivity (i.e. the distance the piezoelectric element distorts at a given applied voltage) decreases somewhat. It is therefore important to periodically recalibrate the instrument using a grating of known spacing (or a suitable atomic sample for short range scanners). This is particularly critical with a new scanner as the sensitivity changes decrease with use.

In practice, the sample is usually moved in a raster pattern relative to the tip, allowing a square image to be built up from individual lines. The axis parallel to the line direction is called the 'fast scan axis', while the perpendicular axis is the 'slow scan axis'.

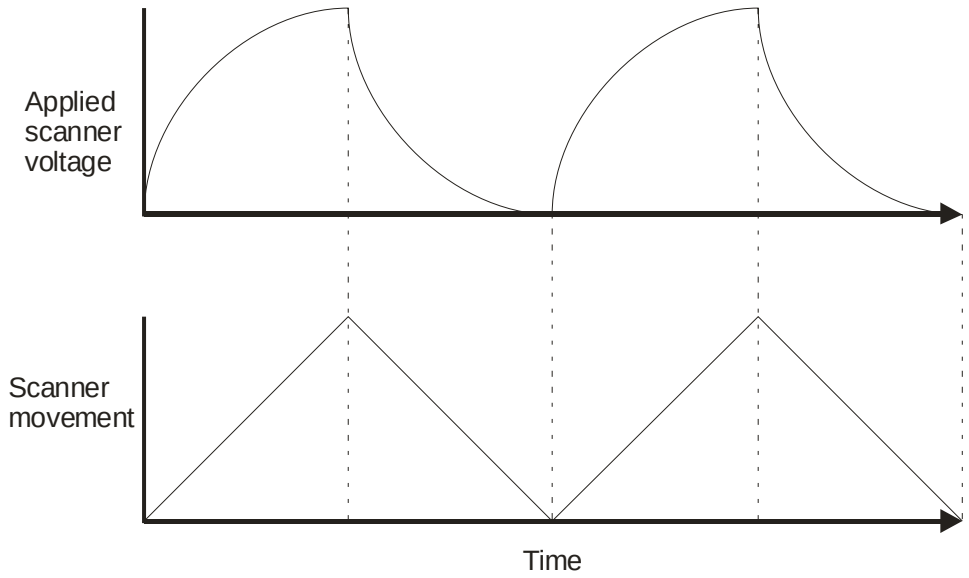

Figure 3.3: Illustration of electronic compensation for non-linear scanner response patterns.

3.3.2 Probe distance regulation

The essential difference between AFM and STM is the method by which the distance between the tip and the surface is measured (although the actual distance is usually not determined quantitatively; the measurement is instead used to observe changes in the tip-sample distance with time/position). In STM a user defined potential is applied between the (conductive) sample and a sharp tip, usually made of tungsten or platinum/iridium alloy. The tip is moved towards the surface until a tunnelling current is generated, which is then measured electronically. The tunnelling current is compared with a user defined current: if the tunnelling current is lower, the surface is

moved closer to the tip using the piezoelectric tube and vice versa. This feedback loop is in fact somewhat more sophisticated than described here, but its purpose is essentially to attempt to maintain a constant tip-sample distance. As the sample is raster scanned in the X-Y directions, the distance by which the scanner must move the sample in the Z direction at each sample point to maintain the setpoint current is measured, and a profile of the surface generated. The monitoring of tunnelling current remains the most sensitive distance measure used in SPM, achieving greater resolution than any other method. However, it suffers from the fact that it requires conductive samples (and will produce incorrect height measurements in samples with non-uniform conductivity; see chapter 11. AFM overcomes this difficulty by employing a fundamentally different distance measure.

AFM uses a sharp tip, usually made of silicon or silicon nitride depending on the application, attached to a flexible cantilever. A laser diode is aimed at the top of the cantilever, and the position of the reflection monitored using a four-segment photodetector. This apparatus (illustrated in figure 3.4A) allows sensitive measurement of the deflection of the cantilever (as well as torsion, although this is not used in simple AFM experiments).

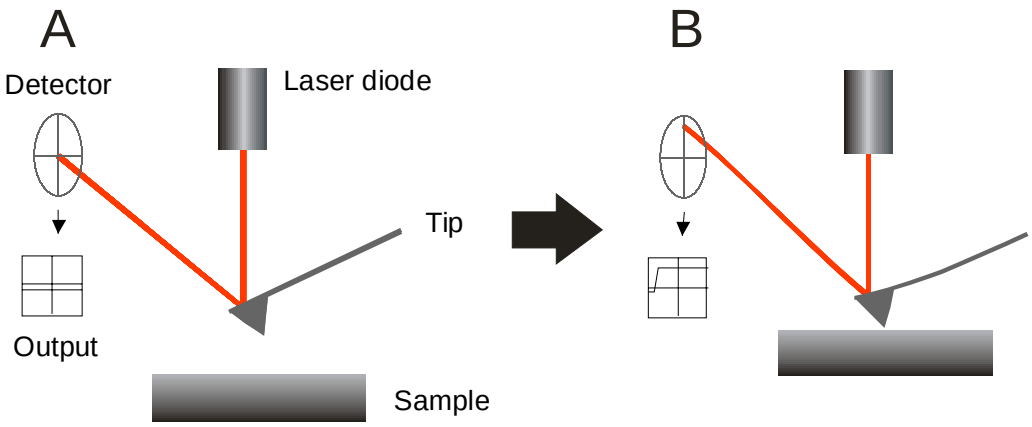

Figure 3.4: A) Schematic diagram of the AFM tip/photodetector configuration in contact mode. B) The effect of moving the sample close to the tip.

In Contact Mode (CM), the conceptually simplest method of AFM operation, the distance between the tip and the sample is monitored by measuring the deflection of the tip as it approaches the surface: as the tip is moved close to the surface, it deflects away from it (for reasons discussed below), and this is recorded by a change in position of the laser on the photodetector (figure 3.4B). While scanning, the feedback mechanism is identical to that described above for STM, except that the feedback loop attempts to maintain a constant cantilever deflection instead of tunnelling current, while measuring the distance in the Z axis the piezoelectric element must move to maintain this deflection. Contact mode is an example of constant force operation: in effect the deflection of the cantilever is a measure of the force the tip is exerting on the sample. This force is relatively large, and the tip is in continuous physical contact with the surface. Contact mode is therefore most appropriate for use on hard and stable surfaces which are unaffected by lateral (shear) forces exerted by the moving tip.

To reduce the interaction between the tip and surface, less invasive imaging modes have been developed. The most useful of these is Tapping Mode (TM). Tapping mode employs a relatively rigid cantilever attached to a piezoelectric oscillator. The oscillator is tuned to the resonant frequency of the cantilever (typically 300 kHz in air or 20 kHz in a liquid). As in contact mode, a laser is reflected from the back of the cantilever to a photodetector; in this case, however, the detector receives an oscillating signal (figure 3.5A). The RMS amplitude of this signal is a measure of the distance the cantilever is moving.

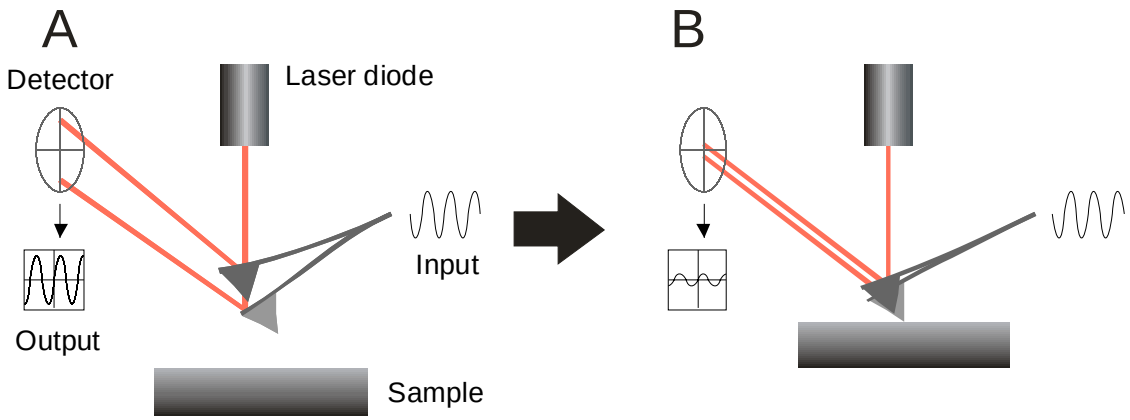

Figure 3.5: A) Schematic diagram of the AFM tip/photodetector configuration in tapping mode. B) The effect of moving the sample close to the tip.

As the distance between the tip and the sample is decreased, the oscillation of the cantilever is damped by interactions between the tip and the surface (illustrated in figure 3.5B). The output RMS amplitude is therefore proportional to the tip – surface distance, and again a feedback loop may be employed, this time adjusting the Z position to maintain a constant output amplitude. As the tip is not in contact with the surface as such, the forces applied to the surface are much smaller, and lateral forces reduced. This makes tapping mode preferable on soft samples, or those with poorly attached features which may be removed by contact mode imaging.

Tapping mode has another advantage over contact mode: a phase image may be recorded simultaneously. This measures the phase difference between the signal applied to the piezoelectric oscillator and the signal recorded at the photodetector. Variations in the characteristics of the surface (including hardness, adhesiveness and elasticity) result in variable phase differences. Phase imaging is therefore particularly useful in distinguishing features with similar morphologies or heights, but with differing surface properties.

3.3.3 Origin of tip-sample interactions

The force exerted between the tip and sample is a combination of attractive and repulsive components. The most important attractive forces are van der Waals interactions and capillary adhesion forces. Van der Waals forces are relatively long range, and relatively weak. They arise from a variety of interactions, particularly induced dipole and quadrupole interactions.[2] Van der Waals forces are non-localized in the sense that they are spread out over many atoms; they have been estimated to contribute a force in the order of 10-20 nN.[3]

When imaging a sample in air, capillary adhesion is usually an important attractive contributor.[4] A meniscus made of water and organic contaminants on the sample and tip is formed between the two surfaces, resulting in a relatively large attractive force, estimated to be 100 nN or greater.[5] Clearly no meniscus can form if the tip and sample are completely immersed in water (or another solvent), so capillary forces do not contribute when imaging *in-situ*. In addition, capillary effects may be reduced or eliminated by taking special precautions such as purging the AFM with dry nitrogen during use.

The primary repulsive force occurs at close range as the orbitals of the atoms or molecules comprising the tip and sample start to overlap, a result of the Pauli Exclusion Principle. Prediction of the magnitude of this effect is complicated by factors such as relaxation of atoms on the sample surface, but in practice at short range this is invariably the dominant force. In addition, repulsive forces may arise from solvation effects; as the tip moves close to the sample, structured solvent

molecules (particularly in the case of water) require energy to reorder as the tip pushes through them.[6]

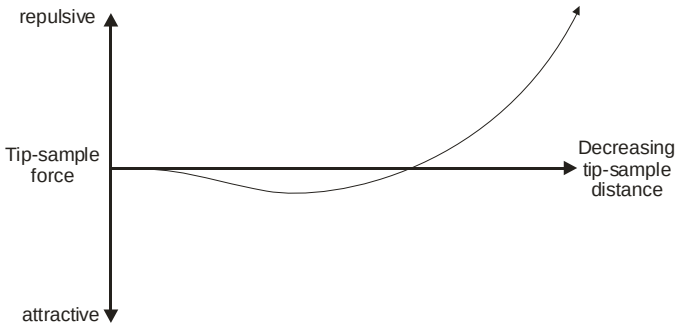

Figure 3.6: Force profile resulting from tip-sample interactions.

Overall, the force profile usually appears similar to that shown in figure 3.6. This profile suggests another possible mode of AFM operation: non-contact mode. If the tip can be moved to a distance from the surface such that attractive forces dominate, the cantilever will deflect downwards. In principle, this downward deflection can be maintained by a feedback loop as in the other operational modes discussed. This mode has the advantage that the large tip-sample distance minimizes disruptive interactions between the two. However, non-contact mode is very difficult in practice; in the attractive domain the forces involved are weaker and there are two tip-sample separations that will exert the same force, but with opposite signs for the force gradient. Tapping mode is therefore used in most applications where reduced tip-surface forces are required.

3.3.4 AFM tip and imaging considerations

In principle, the perfect AFM tip would be infinitely sharp. However, as shown in figure 3.7, the AFM tips usually employed are rectangular pyramidal. Contact mode probes are made of silicon nitride (Si_3N_4), and have a tip radius of <50 nm when new.

Tapping mode probes are made of silicon and have a smaller tip radius, typically <10 nm. The geometries of Veeco (Santa Barbara, CA, USA, www.veeco.com) contact mode and tapping mode tips are illustrated in figure 3.8.

The images originally presented here cannot be made freely available via ORA because of copyright. The original images were from www.veeco.com.

Figure 3.7: SEM images of commercial contact mode AFM tips.

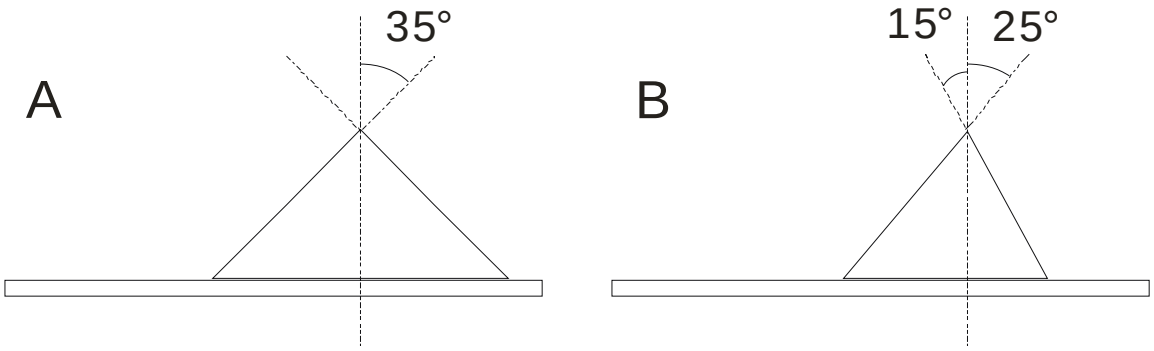

Figure 3.8: Geometries of commercially available AFM tips. A) Contact mode, B) Tapping mode.

The shape of the tip may cause several problems.[7] First, the effective radius of the tip may be reduced, either through wear or damage, or through adhesion of material to the tip. The increased radius of curvature decreases the resolution of the image. In particular, when imaging small steps or narrow features, the decreased resolution will make the feature appear broader than in reality. Severely damaged tips, or those with material adhering to them, may generate even more confusing artefacts including

multiple images of small features. Such artefacts may be reduced by frequently using fresh tips, and changing the tip whenever there is evidence of loss of image sharpness.

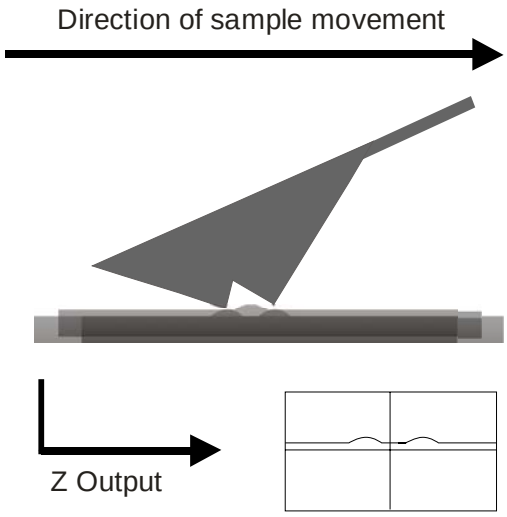

Figure 3.9: Artefacts generated by damage to the AFM tip.

The mechanism for this is illustrated in figure 3.9: in effect there are two tips, each of which generates its own image. Second, with large scale features, the tip shape can convolve with the surface, producing misleading results as the sides of the tip contact the edge of the feature before the apex of the tip contacts the surface. In the limiting case of an infinitely sharp feature on the surface, the feature in effect becomes the probe, and the geometry of the AFM tip is imaged. The effect of the pyramidal nature of the tip on imaging a large hemispherical feature is shown in figure 3.10; there is no way to avoid such artefacts while using commercial pyramidal tips on such a surface. The impact of these artefacts on apparent surface properties such as roughness and volume are discussed in detail in chapter 8.

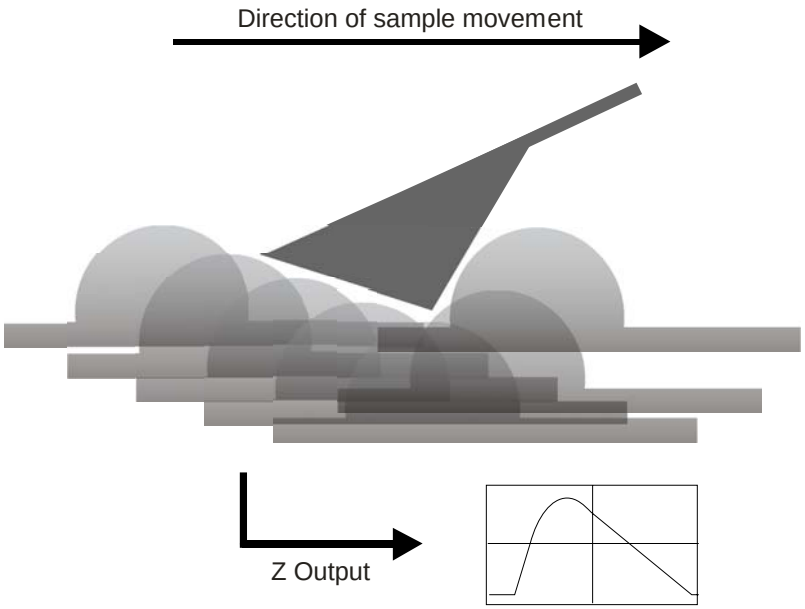

Figure 3.10: Artefacts caused by the pyramidal shape of the tip.

A third problem may occur when attempting to image narrow, deep features such as steep sided pits or trenches (see chapter 10). In this case, the pit will appear to be V-shaped as the edges of the tip meet the sides of the pit before the tip reaches the bottom. In addition, if the pit is deep enough, the tip will not reach the bottom before the other edge is reached, resulting in a decreased apparent depth. Attempts to reduce these second two problems have led to the development of tips with higher aspect ratios; however, these tips are relatively fragile and are not used routinely. Another interesting approach is to use a carbon nanotube as the AFM tip. Despite considerable investigation,[8-13] such tips are not suitable for routine use.

Artefacts may also be introduced into AFM images as a result of the operation of the scanner itself. As mentioned earlier, the response of the piezoelectric tube is non-linear. Particularly after a large change in the potential applied, the tube will continue to deform for some time, resulting in ‘smearing’ or distortion of surface features. In addition, when scanning a large area, horizontal image distortions may become

manifest. This is usually visible as ‘bowing’, where a feature known to be flat, such as an HOPG surface, appears to be curved. Bowing cannot usually be avoided, and the best approach to eliminating it involves careful use of image processing software after the image has been captured.

The quality of the image obtained is also highly dependent on the feedback parameter settings. The feedback control system uses a Proportional, Integral and Differential (PID) gain model. Setting these parameters too low results in poor tracking of the surface by the tip, leading to blurred images. Conversely, setting them too high results in high frequency (on the scale of the image) tip oscillation which obscures the features to be imaged. The correct PID settings are different for different samples, and are usually determined by trial and error and experience. In addition, the tip-sample interaction level affects the quality of the images obtained. Setting the deflection setpoint too low in contact mode (i.e. setting a low tip-surface force) or setting the amplitude setpoint too high in tapping mode will also lead to blurred images, as the tip is too far away to interact fully with the surface. Again, the correct level must be determined by experience; high tip-surface interactions will lead to good images in some cases, but damage the tip and/or sample in others.

Another important factor to consider when imaging is noise, both acoustic and electrical. Especially at small scan ranges, minimization of vibration is critical to achieving good quality images. For larger scale images simply placing the AFM on a passive laser table provides good enough vibrational isolation. Further stabilization can be provided by using a weighted table on bungee cords or springs and a hood to prevent air currents. Electrical noise (e.g. from the mains supply) may also lead to

artefacts in the image as noise in the voltages applied to the piezoelectric elements results in spurious measurements. Finally, changes in temperature may also introduce artefacts as parts of the AFM apparatus contract or expand. This is particularly noticeable when using a fluid cell, as the laser shining through the solution tends to locally heat it (see below for more details on use of a fluid cell).

There are various steps which may be taken to help ensure that an image accurately reflects the real surface. All of the following techniques have been used in the following chapters where appropriate: Similar topographical features should be observed when scanning the same sample with different tips. If in doubt, changing the tip for a new one should eliminate uncertainty in the quality of the image. Changing the angle of the scan axis will ideally reveal an identical image, and if artefacts are present a knowledge of how the tip interacts with the surface should reveal which parts of the image are artefacts. Physically rotating the sample may also be useful. Changing the scan rate (or scan size) should leave the morphology of features essentially unchanged. In addition, the use of image processing techniques should be minimized and used carefully where necessary, as they may modify critical surface parameters as well as removing noise or other artefacts.

3.3.5 Apparatus

All SPM experiments employed a Digital Instruments (now a division of Veeco) Multimode SPM connected to a Nanoscope III controller. The microscope was mounted on a passive laser table and equipped with a hood to reduce vibrational interference. A model 'J' scanner was used, having a lateral range of 125 x 125 µm and a vertical range of 5µm. All *ex-situ* AFM experiments were performed in TappingMode, using standard silicon probes (Nascatec GMBH part NST-NCHF).

STM experiments used commercially available Pt/Ir tips (Veeco part PT). Further experimental details are given in the relevant chapters.

3.3.6 *In-situ* AFM imaging

The use of *in-situ* AFM to study the electrodeposition of metals has some considerable advantages over traditional ex-situ methods. *In-situ* techniques allow the structure of the surface to be probed directly, without the need for removal of the electrode from solution, thereby avoiding any morphological changes that may occur on drying. Also, changes in the properties of a single area as a function of time may be studied, which is impossible when using *ex-situ* techniques.

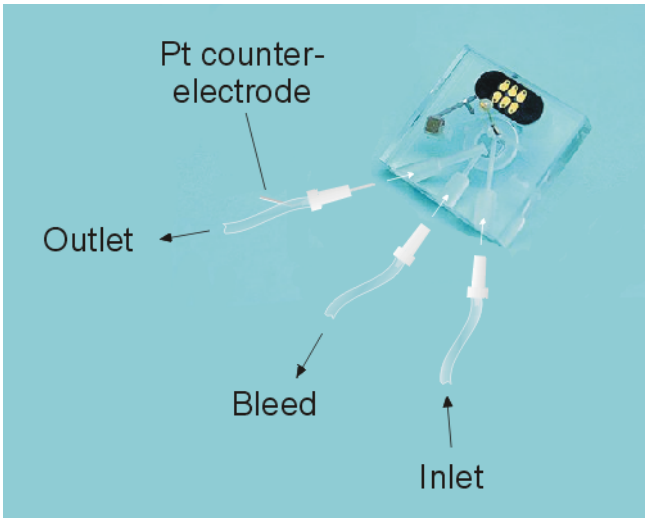

Figure 3.11: The Digital Instruments cell used for *in-situ* AFM.

In situ experiments were performed in a Digital Instruments tapping mode fluid cell (approximate volume 0.5ml), illustrated in figure 3.11. A silicone O ring was placed in the indent in the cell, which was then placed on the top of the AFM electrode and locked into place in the scanner head.

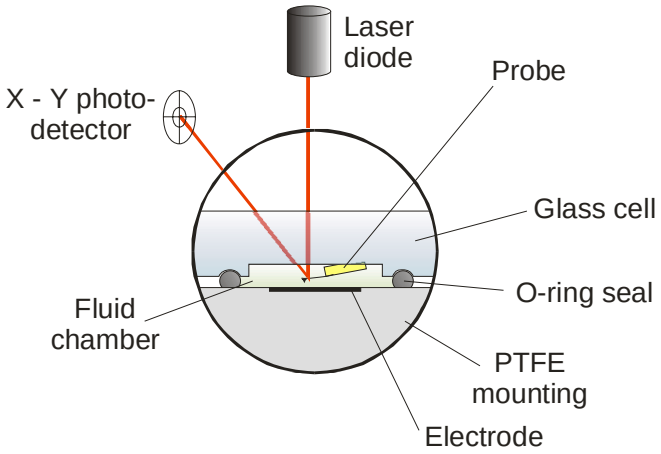

Figure 3.12: Schematic of the interior of the flow cell.

Solution was fed into the inlet using a syringe until the cell was full and no bubbles remained. The inside of the cell was then configured as illustrated in figure 3.12. The outlet and bleed tubes were then sealed using clips, with the outlet tube being sealed downstream from the counter electrode. The partly filled input syringe was then used as a reservoir, into which the reference electrode was placed.

3.4 References

[1] A. J. Bard, L. R. Faulkner, *Electrochemical Methods - Fundamentals and Applications*, 2nd ed., John Wiley & Sons, Inc., New York, **2001**.
[2] J. N. Israelachvili, *Intermolecular and Surface Forces*, 2nd ed., Academic Press, San Diego, CA, **1992**.
[3] F. O. Goodman, N. Garcia, *Phys. Rev. B* **1991**, *43*, 4728.
[4] B. Drake, D. C. Prater, A. L. Weisenhorn, S. A. C. Gould, T. R. Albrecht, C. F. Quate, D. S. Cannell, H. G. Hansma, P. K. Hansma, *Science* **1989**, *243*.
[5] A. L. Weisenhorn, P. K. Hansma, T. R. Albrecht, C. F. Quate, *Appl. Phys. Lett.* **1989**, *54*, 2651.
[6] P. A. Maurice, *Colloids Surfaces A* **1996**, *107*, 57.
[7] T. G. Lenihan, A. P. Malshe, W. D. Brown, L. W. Schaper, *Thin Solid Films* **1995**, *270*, 356.
[8] S. I. Lee, S. W. Howell, A. Raman, R. Reifenberger, C. V. Nguyen, M. Meyyappan, *Nanotechnology* **2004**, *15*, 416.
[9] C. V. Nguyen, C. So, R. M. Stevens, Y. Li, L. Delziet, P. Sarrazin, M. Meyyappan, *Journal of Physical Chemistry B* **2004**, *108*, 2816.
[10] A. Patil, J. Sippel, G. W. Martin, A. G. Rinzler, *Nano Letters* **2004**, *4*, 303.
[11] M. Ishikawa, M. Yoshimura, K. Ueda, *Applied Surface Science* **2002**, *188*, 456.

[12] C. L. Cheung, J. H. Hafner, C. M. Lieber, *Proceedings of the National Academy of Sciences of the United States of America* **2000**, *97*, 3809.
[13] J. Li, A. M. Cassell, H. Dai, *Surface and Interface Analysis* **1999**, *28*, 8.

4 Analysis of Multiple Nucleation with Diffusion Controlled Growth

This chapter outlines the derivation of several important models related to the analysis of the diffusion controlled growth of hemispheres on an electrode surface, as well as discussing the evolution of these analysis methods and their accuracy. The other currently used analysis methods are reviewed, including computer simulation and direct microscopic analysis of the growing nuclei. The principles discussed in this chapter underpin the work in most chapters of this thesis, and one of the derived models is used explicitly in chapters 6 and 7.

4.1 Introduction

Electrochemical deposition is an area of considerable interest, both from a fundamental and applied standpoint, with application to areas such as electroplating and solution analysis. As recent reviews indicate,[1, 2] much work has been done on investigating the mechanism of such deposition over the last fifty years. However, as the discussion in a recent Journal of Electroanalytical Chemistry[3-6] reveals, there is still considerable controversy over even the most basic principles involved in modelling such systems.

It has however become apparent that electrodeposition occurs by a process of nucleation and growth – nuclei appear at active sites on the substrate according to some nucleation rate law, and then grow via the incorporation of further ions from the solution. Given that this is the case, the study of nucleation via electrochemical methods has certain advantages over other methods of investigating heterogeneous

nucleation: the driving force of the nucleation can be varied simply by varying the applied potential. Nucleation and growth can be broadly classified into two categories: 'interfacial (or charge) controlled', in which the nucleus growth rate is limited by the rapidity with which ions can be incorporated into the new phase, and 'diffusion controlled', in which the nucleus growth is limited by the rate at which material is transported through the solution to the electrode surface. The former is favoured by high concentrations and low deposition overpotentials, while the latter is favoured by low concentrations and high overpotentials. Certain systems also tend to one or the other: due to its complex mechanism, PbO_2 is usually deposited under charge control[7] while mercury is a well established example of diffusion control[8] (see below).

With this in mind, this chapter assesses the current situation in one restricted area of electrodeposition: deposition with diffusion controlled growth, with a particular emphasis on the extraction of information about the nucleation process from electrochemical data. Three aspects of this are considered – theoretical modelling, computer simulation, and microscopic observation of electrode surfaces.

4.2 Transient Analysis on Macroelectrodes

4.2.1 Early work

Some of the earliest interest in the mechanism of nucleation and growth of electrodeposited materials was shown in the 1950s, by authors such as Fleischmann and Thirsk and Pangarov[9, 10]. Fleischmann and Thirsk published several papers relating to the formation of lead dioxide on lead and platinum electrodes,[11-13] pioneering the use of a 'constant overvoltage' method, in which a constant potential

after a potential step is applied to a cell and the resulting current measured as a function of time, as a method for extracting information about the nucleation process. The current-time transients they recorded showed maxima,[12] followed by approximately exponential decay, which suggested that the nuclei were formed according to the equation

$$\frac{dN}{dt} = AN_0 e^{(-At)} \tag{4.1}$$

or

$$N = N_0 \left(1 - e^{-At}\right) \tag{4.2}$$

in which t is the time since the potential was applied, N is the number of nuclei, N_0 is the number of active sites and A is the nucleation rate constant (a potential dependent constant with units nuclei s^{-1}).[12] This nucleation rate law is of great significance, as it is assumed as a basis for an entire family of more sophisticated models succeeding Fleischmann and Thirsk's original one.

In 1967, Astley, Harrison and Thirsk[8] investigated the electrodeposition of various metals, including mercury, on to glassy carbon. They attempted two experiments – a) measuring the potentiostatic current-time transient after a single potential step, and b) applying a short potential pulse at relatively high overpotential, before recording the transient as normal at a lower potential (a 'double potential step'). The aim of the double potential step was to rapidly saturate all active sites on the electrode surface during the pre-pulse so that the current response recorded at the second potential would result only from growth of present nuclei. In the case of mercury, they observed that at short times, the transients followed $I \propto t^{3/2}$ when no initial pulse was supplied, and $I \propto t^{1/2}$ when a pre-pulse was supplied. They explained this result by

observing that mercury has no crystalline lattice; it therefore presumably had no slow lattice incorporation step, and the rate of growth is presumably controlled by diffusion of mercury ions to the electrode surface, an explanation which has since been independently verified.[14, 15] Astley et al.[8] modelled this situation by considering a growing hemispherical nucleus of radius r, volume v, in a solution of depositing ions of concentration c, the ions having a diffusion coefficient D. If the nucleus is fed by planar diffusion to the surface, the current required for the growth of the hemisphere and the current due to material reaching the surface can be equated and then integrated to give a total current using

$$\int_0^t i(u)\left(\frac{dN(t)}{dt}\right)_{t=(t-u)} du \qquad (4.3)$$

in which i(u) is the current resulting from a single nucleus at the time after the appearance of that nucleus, u. In case a) above, N(t) is given by equation (4.2), known as 'progressive' nucleation and in case b), $N = N_0$, known as 'instantaneous' nucleation. In this sense, 'progressive' and 'instantaneous' nucleation can be considered as limits of equation (4.2) for large A and as $A \to 0$ respectively. The results of integrating (4.3) are exact for an array of entirely independent nuclei fed by planar diffusion, and give expressions with the required dependence of I on t. An improvement was suggested by Hills et al.,[16] who suggested that that each nucleus should be fed by hemispherical rather than planar diffusion, and adjusted the model accordingly. In fact, this model works well for single nuclei (as was confirmed by microelectrode studies).[17-19]

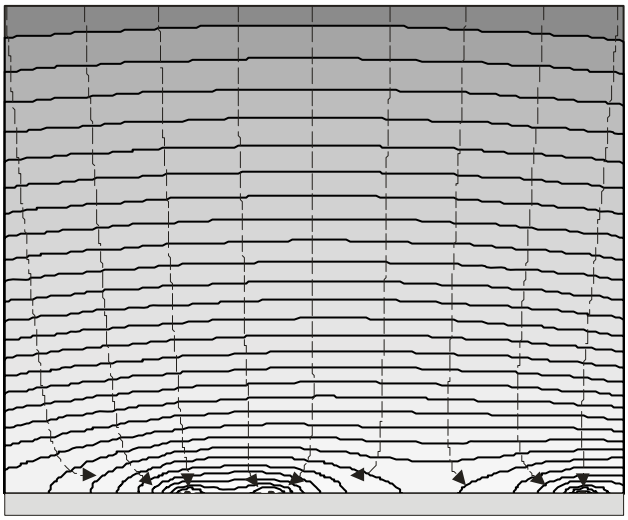

Figure 4-1: Schematic diagram of the growth of diffusion zones around growing nuclei on an electrode surface. Note the eventual overlap, inhibiting the total amount of material available to a given nucleus (illustrated by the dashed arrows).

A critical weakness of the above models is their failure to correctly reproduce the overlap of diffusion zones: in the case of multiple nucleation on a macroelectrode, individual nuclei will have a diffusion zone with a size dependent on the age/size of the nucleus. At some point, these diffusion zones will begin to overlap, as illustrated in figure 4.1, reducing the total amount of material available for incorporation into the growing hemispheres. The currents predicted by the above models are therefore too high, particularly at relatively long times.[20, 21]

4.2.2 Treatment of multiple nucleation

In fact, although nucleation occurs at the plane surface of the electrode, the nucleus growth and diffusion of depositing material extend into the bulk electrolyte. This generates a situation somewhere between a two dimensional and three dimensional problem, which is difficult to analyze mathematically. Scharifker and Hills[22, 23] attempted to do this by considering the hemispherical diffusion to a hemispherical nucleus, and re-expressing this as an equivalent area of plane surface fed by linear

diffusion. The overlap of diffusion fields is thus reduced to a true two dimensional problem, which is tractable via use of Avrami's theorem,[24, 25] which states that

$$\theta = 1 - e^{\left(-\theta_{ex}\right)} \tag{4.4}$$

in which θ is the area on which new nuclei can appear and θ_{ex} is the 'extended area', the theoretical fraction of the area θ which has been nucleated if overlap is ignored. (The derivation of Avrami's theorem is discussed in more detail in Appendix 2). Avrami's theorem allowed Scharifker and Hills to relate the radial flux density through the real diffusion zones to an equivalent diffusive flux to an electrode of area θ. By applying a mass/current balance, then integrating for the instantaneous or progressive cases (as before), expressions can be derived for the total current with respect to time in terms of a parameter, k, found to be $k = \left(8\pi cM/\rho\right)^{1/2}$ and $k = \frac{4}{3}\left(8\pi cM/\rho\right)^{1/2}$ respectively, in which c is the concentration, M the molar mass, and ρ the density of the depositing species. The equations are usually used in the form of dimensionless curves, in which I^2/I_m^2 is plotted against t/t_m, with I_m and t_m being the current maximum of the measured potentiostatic transient, and the corresponding time respectively. These dimensionless curves have a characteristic shape for instantaneous and progressive nucleation (see figure 4.2), and comparison with experimental data has been used widely to examine the 'progressive/ instantaneous' character of reactions; some examples are listed at the end of this chapter.

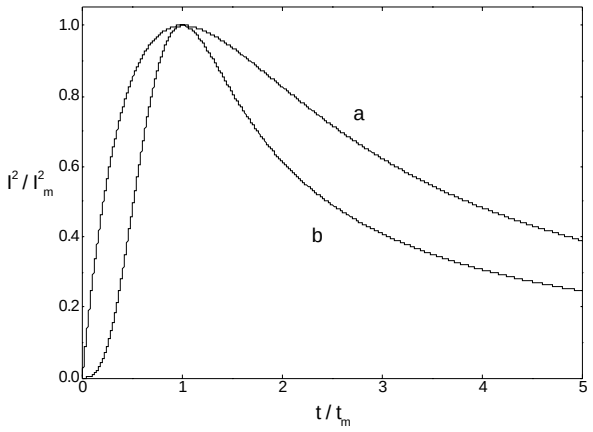

Figure 4-2: Theoretical non-dimensional plots of I^2/I_m^2 vs. t/t_m for a) instantaneous and b) progressive nucleation.

In practice, however, it is difficult to extract useful parameters from this model, and it suffers from the requirement that 'progressive' and 'instantaneous' cases be treated separately. It should be noted that a similar model, applying Avrami's theorem to discs generated by the overlap of nucleation hemispheres, was derived by Bosco and Rangaranjan at about the same time[26, 27]

The model of Scharifker and Mostany ('SM model')[28] essentially introduces the improvement that an a priori definition of k, $k = (8\pi cM/\rho)^{1/2}$ is used (in fact Scharifker and Hills' value for the instantaneous limit). The nucleation is described by equation (4.1), and the need for two separate cases to be considered is eliminated.
To derive an expression for the total current, the current as a result of hemispherical diffusion towards a 'free' hemispherical nucleus is considered. As with the Scharifker and Hills ('SH') model, this is then 'projected' to give a problem in terms of circular diffusion zones, having time dependent radii. The resulting diffusion cylinders are illustrated in figure 4.3A.

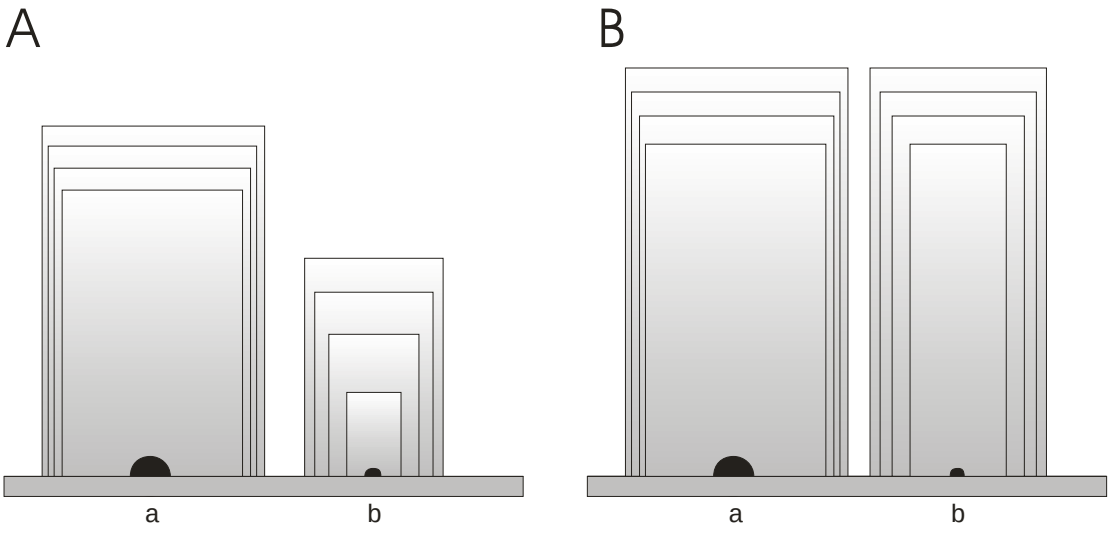

Figure 4-3: Schematic views of the hypothetical diffusion cylinders around a) an established nucleus and b) a newly appeared nucleus at successive time intervals after nucleus (b)'s appearance (smallest cylinders to largest cylinders). A) SM model, B) SRWBS model. Note that the top of the cylinders represent bulk solution concentration; the SRWBS model is formulated to ensure equal diffusion layer thicknesses for all nuclei.

Scharifker and Mostany state that the appropriate time variable for the consideration of the size of the diffusion zone at time t is the time since the appearance of a nucleus, $(t-u)$, and hence the expression for the radial flux, δ, is

$$\pi\delta_{SM}^2 = (2\pi)^{\frac{3}{2}} D\left(\frac{cM}{\rho}\right)^{\frac{1}{2}}(t-u) \tag{4.5}$$

Avrami's theorem may then be applied, giving the result

$$I_{SM} = \frac{1}{\alpha(At)^{1/2}}\left\{1-\exp\left[-\alpha\left(At-1+e^{-At}\right)\right]\right\} \tag{4.6}$$

in which

$$\alpha = (2\pi)^{\frac{3}{2}} D\left(\frac{cM}{\rho}\right)^{\frac{1}{2}}\frac{N_0}{A} \tag{4.7}$$

and D is the diffusion coefficient, c the concentration, M the molar mass, and ρ the density of the depositing species. Equation (4.6) is widely used as is it can be directly

compared to experimental data to extract the parameters N_0 and A. However, Hyde et al.[29] note that in fact direct least squares fitting to experimental transients is difficult because a range of values of N_0 and A give similarly shaped curves. A modification is suggested, in which only the rising part of the transient is analysed, allowing an unequivocal value of N_0A to be established. Another interesting solution to this problem is suggested by Yu et al.[30], who use a genetic algorithm to estimate A, N_0 and D. The Scharifker and Mostany method has also been modified for use under conditions of forced convection[31, 32], in which the Cottrell diffusion to the surface is replaced by an expression based on a constant diffusion layer thickness.

A modification of the Scharifker and Mostany model was attempted by Sluyters-Rehbach, Wijenberg, Bosco and Sluyters ('SRWBS').[33] They derived the exact result for independent nuclei in terms of the general nucleation rate law (equation (4.1)), and demonstrated that in the limit of no overlap the Scharifker and Mostany model is inconsistent with the exact result. In order to avoid this, they considered planar diffusion zones of uniform thickness (as shown in figure 4.3B), with the result that the concentration gradients are uniform over the substrate surface. The hypothetical radial flux δ is then a function of both $(t-u)$ and t itself:

$$\pi\delta_{SM}^2 = (2\pi)^{\frac{3}{2}} D\left(\frac{cM}{\rho}\right)^{\frac{1}{2}} (t-u)^{\frac{1}{2}} t^{\frac{1}{2}} \tag{4.8}$$

After applying the same reasoning as before, the current is found to be:

$$I_{SRWBS} = \frac{1}{\alpha(At)^{\frac{1}{2}}}\left\{1-\exp\left[-\alpha(At)^{\frac{1}{2}}\left\{(At)^{\frac{1}{2}} - e^{-At}\int_0^{\sqrt{At}} e^{\lambda^2} d\lambda\right\}\right]\right\} \tag{4.9}$$

in which λ is a dummy variable. This expression correctly reduces to the exact expression in the limit of no nuclear overlap and the Cottrell equation as $t \to \infty$, but

has been criticized[34] as expressing the radial flux in terms of $(t-u)$ and t is 'unphysical', in the sense that it implies later appearing nuclei will grow faster than early appearing ones.

Despite the similarities of the above two models, they generate quite different results.[34, 35] Heerman and Tarallo ('HT')[36] reconcile the two approaches. They note that Scharifker and Mostany's result for the extended coverage is correct (despite the objections of SRWBS), but that implicit in the SM model is the fact that the height of all the diffusion cylinders is equal to $(\pi Dt)^{1/2}$, which is the thickness of the Nernst diffusion layer for a simple redox reaction. However, they argue that the expansion of the diffusion layer should be a function of the nucleation rate constant as well as time and therefore it is inappropriate to use Cottrell's equation to describe the current density. Instead, a parameter $\overline{\delta}$, the thickness of the uniform diffusion layer in the case of overlap, should be introduced via a generalization of the reasoning of SRWBS's method. When treated as before using Avrami's theorem, this generates the result

$$I_{MN/HT} = \frac{(At)^{\frac{1}{2}} - e^{-At}\int_0^{\sqrt{At}} e^{\lambda^2} d\lambda}{\alpha\left(At - 1 + e^{-At}\right)}\left\{1 - \exp\left[-\alpha\left(At - 1 + e^{-At}\right)\right]\right\} \qquad (4.10)$$

which is notable for including terms from both Scharifker and Mostany and SRWBS's expressions for the current. In fact this result was derived earlier by Mirkin and Nilov,[37] who used a general solution in the form of integral equations which could be used to calculate the current response for an arbitrary dependence of the applied potential on time. Equation (4.10) was then derived as a special case in which the applied potential remained constant throughout the experiment. On the other hand,

Heerman and Tarallo's method is more easily related to earlier models. Márquez et al.[38] compare the accuracy of the HT/MN model with the SM model, and find that in practice the results of each are fairly similar, but point out that both deviate from experimental results to some extent. Mendoza-Huizar et al.[39, 40] reach similar conclusions; however, they warn against the use of such models without considering the possibility of additional reactions mechanisms such as initial Langmuir type adsorption of the depositing species. In addition, Langerock and Heerman[41] warn against the 'blind' use of pure diffusion controlled models: they use a quartz crystal microbalance to demonstrate that at relatively low overpotentials the electrodeposition of rhodium is characterized by very slow charge transfer kinetics.

Heerman, Matthijs and Langerock improve upon Heerman and Tarallo's theory[42] by observing that although the result is (arguably) correct, its derivation (along with that of SM and SRWBS) is wrongly based on the principle of a flux balance. They suggest an improved derivation, based on applying the concept of a planar diffusion zone to an ensemble of growing nuclei, rather than a single nucleus. This approach leads elegantly to the definition of HT's diffusion layer thickness, $\overline{\delta}$, which they then show is related to the 'mean concentration field' approximation used by Bobbert et al.[43] (see below), although Bobbert's earlier treatment was considerably more limited. Matthijs et al.[44] improve further upon the HT model, arguing that in some cases it produces unphysical results. A correction is proposed, based on a slightly different interpretation of the Avrami theorem.

One feature of the above models is that they allow estimation of the number of active sites and nucleation rate as a function of experimental conditions. This has been

attempted by many authors, a recent selection of which are listed in table 4.1. In particular it has been noted for a variety of systems that both N_0 and A are extremely sensitive to the applied potential, with increases in potential increasing the number of active sites and nucleation rate.[45-47]

Table 4.1: Selected recent examples of the application of theoretical models to the analysis of potentiostatic current transients: SH = Scharifker and Hills,[19] SRWBS = Sluyters-Rehbach, Wijenberg, Bosco and Sluyters,[33] SM = Scharifker and Mostany,[28] HT = Heerman and Tarallo,[36] MN = Mirkin and Nilov.[37]

Theoretical model used	Deposition system	Reference
SH	Bismuth oxide on polycrystalline bismuth	[48]
SH	Indium and zinc on vitreous carbon	[49]
SH	Mercury and silver on boron-doped diamond	[50]
SH	Copper on n-Si and TiN	[51]
SH	Indium on vitreous carbon	[52]
SH	Lead on n-Si(111)	[53]
SH	Mercury on HOPG	[54]
SH	Platinum on HOPG	[55]
SH	Cobalt on stainless steel	[56]
SH, SM	Silver on TiN	[57]
SH	Aluminium on gold and vitreous carbon	[58]
SH	Gold on n-Si(100)	[59]
SH	Gold on n-Si(100)	[60]
SH	Silver on ITO	[61]
SH	Nickel and cobalt on gold and vitreous carbon	[62]
SH	Copper on Si(100)	[63]
SH	Zinc on vitreous carbon	[64]
SH	Silver on HOPG and vitreous carbon	[65]
SH	Copper on vitreous carbon	[66]
SH	Lead on n-Ge(111)	[67]
SH	Copper on n-Si(111)	[68]
SH	Copper on n-Si(111) and n-Si(100)	[69]
SH	Rhenium on polycrystalline gold	[70]
SH	Copper on n-Si(111)	[71]
SH, HT/MN	Palladium on Au(111)	[72]
SH	Bismuth sulfide on bismuth	[73]
SH	Cobalt on vitreous carbon	[74]
SH	Copper on vitreous carbon	[75]
SH	Lead and copper on ITO	[76]
SH	Copper on vitreous carbon	[77]
SH	Copper on vitreous carbon	[78]
SH	Copper on chromium	[79]
SH	Zinc on HOPG	[80]

SH	Copper on ruthenium	[81]
SH	Silver on gold	[82]
SH	Platinum on vitreous carbon (in ionic liquid)	[83]
SH	Silver on vitreous carbon (in ionic liquid)	[84]
SH	Copper on platinum/sulfur modified platinum	[85]
SH	Zinc on steel	[86, 87]
SRWBS	Copper on poly-1-napthylamine	[88]
SM	Tin on vitreous carbon and HOPG	[89]
SM	Mercury on vitreous carbon	[90]
Modified SM	Zinc on vitreous carbon	[30]
SM	Lead on vitreous carbon	[29]
SM	Silver on boron doped diamond	[91]
SM, Modified SM	Cobalt on vitreous carbon	[31]
SM	Copper on nickel and tantalum	[92]
SM, HT/MN	Silver on vitreous carbon	[93]
SM, HT/MN	Cobalt on gold	[39, 40]
HT/MN	Platinum on titanium	[94]
HT/MN	Rhodium on gold	[95]
HT/MN	Rhodium on gold/thiolate modified gold	[96]
Modified HT/MN	Zinc on platinum	[97]
Modified HT/MN	Cobalt-molybdenum alloy on vitreous carbon	[98, 99]
D'Ajello, Munford and Pasa	Cobalt on n-Si	[100]
D'Ajello, Munford and Pasa	Copper and nickel on n-Si	[101]
D'Ajello, Munford and Pasa	Silver on vitreous carbon	[44]
Milchev	Mercury on platinum	[102]
Fletcher	Zinc and lead on random arrays of carbon fibre microdisks	[103]
Fletcher	Platinum on carbon	[104]

4.2.3 Related approaches

Isaev and Baraboshkin[105] derive a model similar to the three described in the previous section, applying Kolmogorov's theory[106] (equivalent to Avrami's; see above) to radial diffusion to an array of hemispheres. Both the instantaneous and progressive cases are considered, but Isaev and Baraboshkin's assumption that the hemispheres will be fed by radial diffusion throughout the deposition process appears to be incorrect.[34]

Recently, a model was developed by D'Ajello et al.[100, 101, 107, 108] using a stochastic approach. It introduces a new parameter, the 'reaction radius', which may be related to experimental variables such as the deposition potential, and approaches the Scharifker and Hills model[23] as a limiting case. It appears to describe experimental transients well, but has not been extensively tested in relation to the more established models.

The above methods all rely on Avrami's theorem to treat the overlap of diffusion zones. Other approaches have been attempted, with varying degrees of success. Bobbert et al.[43] criticized Scharifker and Hills' model, considering the physical significance of their 'diffusion zones' rather vague, a problem which afflicts all models based on this method. A different approach was suggested, in which diffusion to an assembly of hemispheres on a substrate is replaced by diffusion to an assembly of spheres in free space, with centres on a plane. The spherical nuclei are considered as point 'sinks' (a good approximation as long as the nuclei are relatively widely spaced). They derive an expression for the concentration field around an individual nucleus, and extend this to an equation in principle determining the time evolution of the entire system. However, in practice, this is intractable. To resolve this problem, it is shown that to a good approximation that the individual concentration fields of the nuclei can be replaced, at a small distance from each nucleus, by a 'mean concentration field'. They then compared the results from using the approximation with a numerical simulation, and observed that errors due to nucleus correlation effects were fairly small; the results obtained were similar to those of the Scharifker and Hills model, but Bobbert's model suffers from the fact that it is difficult to apply to anything other than instantaneous nucleation. Several other authors have

considered diffusion to arrays of growing hemispheres in various configurations,[109, 110] but the theory has not been developed further with the intent of extracting data about the nucleation and growth process from current transients.

Tokuyama also considered the case of diffusion to an array of hemispherical nuclei after instantaneous nucleation.[111] but attempted to systematically examine the correlation between nuclei using a statistical mechanical method. His extensive treatment allows the description of nucleus size distribution, average nucleus radius and average total current as a function of time, and it is concluded in a later paper[112] that in some cases (particularly at long times) nucleus correlation can have a significant effect on the current response. This theory has since been developed,[113] but again the focus of the authors is not explicitly on analysis of experimental data, and only considering the (theoretically simpler) instantaneous case limits its application to in this area.

4.2.4 Validity of the above results

A minor criticism of the application of Avrami's theorem is given by Mulder et al.,[114] who prove that in the case of slow nucleation with diffusion limited growth, the diffusion zone associated with a nucleus born inside another already present zone can expand outside it, an effect which for which the Avrami theorem cannot account. A modification to the Avrami theorem of the form

$$\theta = F\left\{\theta_{ex}(t)\right\}.\left(1-e^{(-\theta_{ex})}\right) \tag{4.11}$$

is suggested, in which $F\left\{\theta_{ex}(t)\right\}$ is a correction factor which Mulder et al. determined by simulation. In fact, however, these simulations also indicated that the

error introduced by using the traditional theorem is small in the case of diffusion controlled growth.

Another approach is considered by Milchev et al.,[93, 115, 116] who noted that in order to apply Avrami's (or equivalent) theorem it is necessary to assume that the nucleation rate has its initial value beyond a critical distance from a growing cluster, and is zero inside this radius: 'nucleation exclusion zones' are defined, in which no nucleation at all occurs. Clearly this is an approximation, as the nucleation rate (some function of concentration and overpotential) should vary continuously with the distance from the cluster. Milchev et al. therefore derive an exact expression for the nucleation rate as a function of the distance from a growing nucleus. The concentration, overpotential and nucleation rate distributions are shown to be continuous, and the current resulting from one nucleus is derived. In fact, studies of nuclei distributions have indicated that this method is fundamentally correct.[115, 117-121] However, the effects of an array of nuclei give rise to a rather complex problem for which there is at present no analytic solution; hence this approach cannot be used directly to extract nucleation parameters from transient data. This issue is discussed further by Gamburg.[122-124]

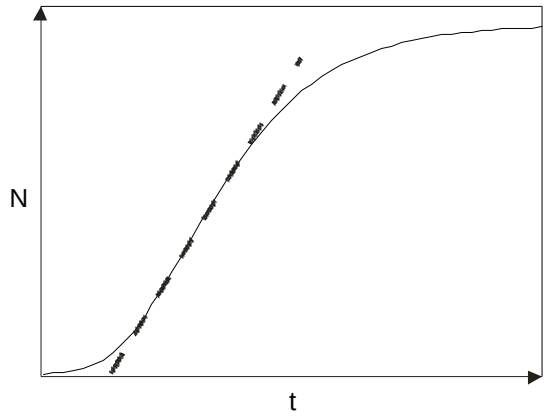

Figure 4-4: A typical plot of nucleus number, N, vs. time for a potentiostatic experiment. The dotted line indicates the 'stationary nucleation rate'.

Although the above two models expose flaws in the well-established models described above, they are based on essentially similar principles. More serious criticisms have been levelled at the assumptions implicit in these principles, particularly the validity of equation (4.1). Several authors have suggested models in which different active sites have different activities with respect to nucleus formation.[125-128] In 1986 Fletcher[129] considered the mathematical treatment of a system in which the number of active sites is time dependent. A system in which there is no fixed number of active sites (N_0 in equation (4.1)) is physically incompatible with those based on equation (4.1) – the existence of an N_0 implies that the electrode surface is energetically frozen, in the sense that the number of active sites is instantaneously fixed when a deposition overpotential is applied. Milchev (in a more recent set of papers to those described in the previous paragraph)[130] developed this approach, suggesting that independent electrochemical reactions, such as surface transformation phenomena, which occur concurrently with the nucleation process, may have the effect of making active sites appear or disappear. An expression was then derived for the stationary nucleation rate (where 'stationary' indicates the approximately linear part of the graph of the number of nuclei against time, as shown in figure 4.4) as a function of time and rate constants for active site activation, deactivation and occupation by a nucleus. This is further developed to some extent for situations under diffusion control,[131] using a nucleation exclusion zone method to calculate a total current. The resulting expression is interesting in that it contains two terms, one the consequence of stationary nucleation processes, and the other from non-steady state effects, but has not been more recently developed.

The use of equation (4.1), and all models based thereon, has been criticized most severely by Fletcher,[5, 6] who considers the use of a constant nucleation rate, A, to be entirely irreconcilable with the reality of electrochemical nucleation. The reasons stated for this are twofold: first that on any realistic electrode there will be a wide range of interfacial free energies across the surface, and therefore nucleation will occur at rates differing by several orders of magnitude at different sites on the electrode. This phenomenon is described as 'nucleation rate dispersion'.[132, 133] Second, equation (4.1) neglects non-steady state effects caused by rapid changes in potential, casting doubt on the validity of classical double potential step experiments. Deutscher and Fletcher describe this effect as 'nucleation persistence'.[103] Instead they recommend a method based on carrying out transient experiments on microelectrodes to determine the partial current due to one nucleus, then using the total current from an array of nuclei to deconvolute the number of nuclei as a function of time.[103, 134] In turn, Deutscher and Fletcher's results have been criticized by Abyaneh and Fleischmann,[3, 4] who believe that traditional theories provide satisfactory explanations for all observed phenomena.

It should also be noted that Abyaneh and Fleischmann[3] believe that the study of diffusion controlled nucleation (as opposed to 'slow' electrocrystallization phenomena) should be discouraged at this stage, considering that the presence of diffusion complicates the investigation of fundamental kinetic aspects of nucleation.

4.2.5 Use of computer simulation

Particularly in recent years, computer simulation has become an increasingly important method for gaining new insights into nucleation and associated processes. One of the earliest attempts was by Sluyters et al.[135, 136] They essentially considered

a critical nucleus capable of either decreasing in size, staying the same, or growing at each iteration with a defined probability for each of the occurrences. Repeating for many nuclei allowed the mean cluster size to be plotted as a function of time, providing some interesting qualitative results, particularly relating to the induction time (the time after the application of a potential step before nucleation can be observed).

More modern attempts at simulation have focussed on analysing the distribution of an array of growing nuclei. Scharifker et al.[121] carried out Monte Carlo simulations in which nuclei were randomly generated at regular intervals in a square region with a periodic boundary. At each time step, a nucleation exclusion zone was generated (or updated) for each nucleus. Any newly generated nuclei appearing within one of these zones was discarded, and the simulation continued until no new nuclei had been generated for 1000 consecutive steps. Various exclusion zone rate laws of the form $r = kt^s$ (where r is the exclusion zone radius and k and s are constants) were tried, and after correcting for boundary artefacts, nearest neighbour distributions were extracted from the resulting data. Essentially, it was concluded that information on surface energies could be determined using nearest neighbour distributions, or conversely that given information about the nucleation mechanism, the approximate form of the distribution could be calculated. In a later paper, Serryua et al.[120] used the same method in the analysis of lead nuclei deposited on glassy carbon.

The same method was again used by Scharifker et al.[34] to demonstrate that the Scharifker and Mostany model[28] provided better current transient fits that either the Mirkin and Nilov[37] model or the SRWBS model[33] (but see the work of Cao et al.,[35]

below). Fransaer and Penner[137] used a Brownian dynamics based simulation to show that the SM model showed serious deviations from the simulated system. However, this model was improved to more accurately reproduce the physics of a real system by Trias et al.,[138] who found that the SM model agreed in most respects with their simulation.

Scharifker's method (as described above) introduces three significant simplifications – first, nucleation exclusion zones were defined a priori, with a discontinuous distribution. Second, the rate law was assumed to be a simple power law. Third, the already present nuclei were assumed to grow independently during the simulation. Milchev et al.[115] to complement their theoretical approach involving continuous nucleation rate distributions (see above), corrected this, using a modified probability distribution. However, given the complexity of the local concentrations and potentials within an assembly of nuclei, only certain special cases were considered: instantaneous nucleation in an array of independently growing clusters and progressive nucleation with the probability of a new nucleus being formed dependent on the oldest nearest neighbour. An extension of the latter case was also investigated, in which the probability of a new nucleus being formed is dependent on all the nuclei present.

In fact, using all the nuclei to calculate the nucleation probability overestimates the effects of inhibition; it appears that closer nuclei screen the effect of more distant ones. The nucleus number densities and spatial distributions calculated were therefore incompatible with experimental results. An improvement was suggested by Kruijt et al.[116], in which between 1 and 5 nearest neighbours were considered.

Despite better agreement with experiment, the choice of number of neighbours seemed somewhat arbitrary, leading to a method proposed by García-Pastoriza et al.:[139] the nuclei which are not screened by others are identified using the Dirichlet tessellation procedure, providing a systematic method for identifying the 'natural neighbours'. They simulated nucleation with the effects of all natural neighbours compounded, and also considering only the most influential neighbour, then derived nearest neighbour distributions. Comparison with experiment indicated that using only the most influential neighbour was actually more accurate. It was also established that the nucleus distribution was effectively independent of the size of a critical nucleus, and surprisingly little affected by different dependencies of the nucleation rate as a function of distance from the growing centre.

Interest has also been shown in modelling diffusion to electrodes of various geometries using 'brute force' methods, so called because Fick's laws are essentially re-derived in each simulation, leading to considerable computational inefficiency. Nagy et al.[140] proposed a simple model in which a number of particles are moving on a random walk in a three-dimensional box with periodic boundary conditions on the x and y axes, and a system designed to emulate the behaviour of the bulk solution at the top of the box. Particles moving within a critical radius from a nucleation point are incorporated into the nucleus, and its size increased correspondingly. This was performed for a hemispherical electrode, a disc shaped electrode and a growing hemisphere. It was found that despite the model's simplicity it agreed well with analytical expressions for the current to and concentration profiles. This method was used again to model an ordered array of instantaneously nucleated hemispheres.[110] The simulation was compared to some analytical theories, and good agreement was

found at certain concentrations; the authors used this to define the concentration ranges in which the theories were acceptable. Heerman and Tarallo later evaluated the method used by Nagy et al.;[141] they noted that there were certain flaws in the way the growing nucleus was handled, but concluded that although the results produced were noisy, the method was useful under certain conditions. Some improvements were also suggested. Also, a method based on the same principles was later used by Frasnaer and Penner[137, 142] using much larger simulation volumes and random or hexagonal arrays of instantaneous nuclei. The results were comparable with the Scharifker and Mostany model, and in addition could be used to study particle size dispersions.

A related method was used by Vilaseca et al.[143] to analyze both diffusion and nucleation. A two-dimensional lattice represented the solution, with particles distributed randomly throughout. At each time step, a particle could move to one of its four neighbouring sites (assuming it was empty). Particles neighbouring the planar electrode at the bottom of the lattice were aggregated according to a probability law designed to simulate progressive nucleation. Again, the model appeared to work well, the main conclusion of the paper being that the coverage of nuclei on the surface deviated from a Poisson distribution by significant amounts, and hence the Avrami theorem is not satisfied, again casing doubt on the validity of the major models.

A different approach is used by Cao et al.,[35] who use a method based on three-dimensional Green's functions. This has the advantages that a) it solves exactly for the mass transfer to an array of nuclei without the explicit introduction of diffusion zones, b) the concentration at non-nucleated active sites can be directly determined,

and c) it can predict the distribution of nuclei sizes. Nucleation itself was simulated using a Monte Carlo method. Use of this process allowed the authors to conclude that the Mirkin and Nilov[37] model agreed significantly better with the simulation than competing models[28, 33]. Zheng et al.[144] used similar simulations to compare the SM, SRWBS and MN models, as well as analyzing the distribution of particle sizes. This method has also been applied to growth of deposits on disk microelectrodes.[145]

Other interesting numerical models have recently been proposed by Sochnikov and Efrima,[146] although they only consider two-dimensional metal deposition, and Pricer et al.,[147] who simulate the electrodeposition of copper on to a flat copper surface using a Monte Carlo method linked to a finite difference model.

4.2.6 Surface analysis

All the models described above rely at some point on simplifying assumptions or approximations; although computer simulation may be used to test the validity of the models, there is no substitute for independent verification of the parameters derived from a model. Towards this end, various attempts to directly study the number, size and distribution of developing nuclei have been made. One of the earliest approaches used was by Markov and Stoycheva[128] who used a double potential step technique to initially nucleate mercury onto a platinum electrode, and then grow the droplets until they could be counted using an optical microscope. The same method was recently used by Milchev,[130] using a modified version of the double potential step.

Optical microscopy has remained popular, as it allows measurements to be collected in-situ with relative ease. Serruya et al.[120] used a single potential step, applied long

enough to ensure saturation of the surface, followed by microscopic observation of the surface to investigate the distribution of lead depositing on glassy carbon.

Scanning probe microscopy (SPM) is also a popular analysis tool, its much higher resolution proving useful for example in the analysis of early stages of nucleation. Recently, ex-situ AFM and SEM have been frequently used to study the morphology of deposits.[38, 41, 77, 80, 148] For example, Correia et al.[62] investigate the deposition of nickel and cobalt nuclei on to gold using both of these methods. Liu and Penner[149] also used SEM to investigate the spatial and size distribution of gold and silver nuclei on HOPG. Knake et al.[150] have studied the nucleation of gold at a liquid-liquid interface using AFM and TEM.

A newer approach is the use of in-situ SPM techniques; these provide significant advantages over ex-situ microscopy, including avoiding the possibility of morphological changes on removal of the electrode from solution. Also, changes in the properties of a single area as a function of time may be studied. An extensive review of the use of in-situ SPM has been presented by Gewirth and Niece;[151] most nucleation studies involve crystallographic metal planes as electrodes, and focus on the atomic scale appearance of electrochemically deposited adatoms, rather than the determination of nucleation parameters. However, in 1996, Mao et al.[152] imaged a single nucleus of silver growing on a carbon microelectrode in-situ, demonstrating the possibility of using AFM to study these properties.

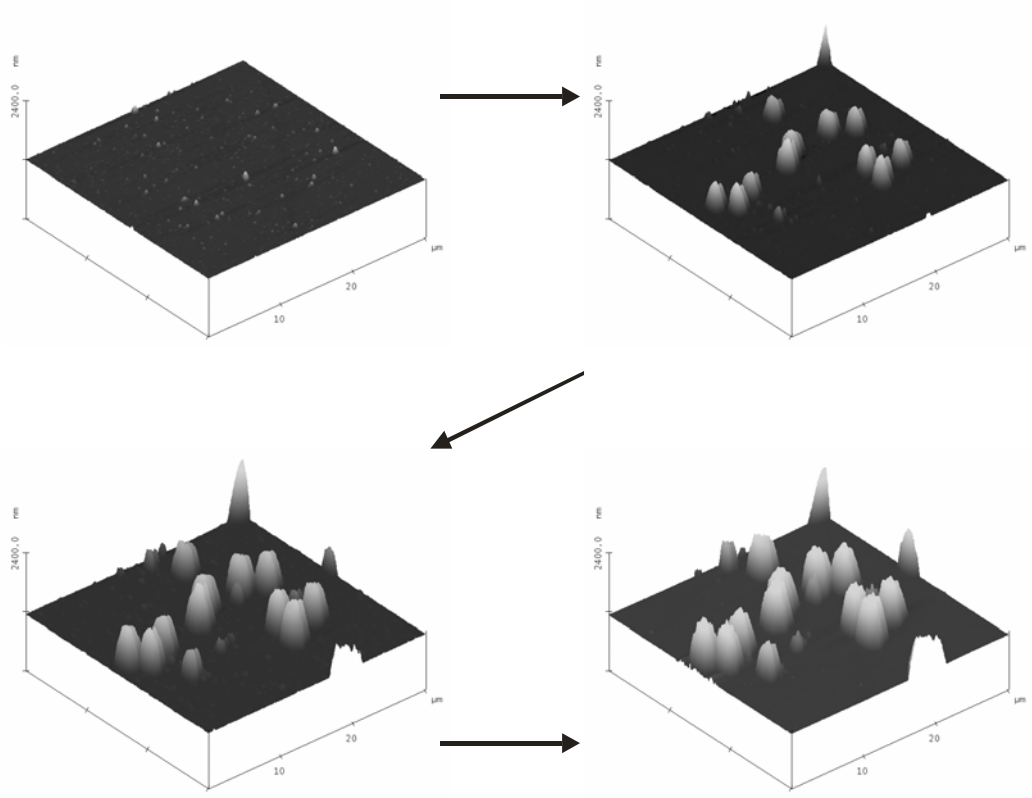

Figure 4-5: In-situ tapping mode AFM images of lead nuclei deposited from a solution containing 500µM $Pb(NO_3)_2$ and 1M KNO_3 on a boron doped diamond electrode at –0.7V vs. SCE. Successive images are separated by a deposition interval of 40s, with the first showing a clean electrode. Scan size 30µm x 30µm, z range 1200nm.

The present author recently used in-situ AFM to study lead nuclei on a boron doped diamond surface,[29] directly observing the appearance and growth of individual nuclei. An example sequence of the images obtained are illustrated in figure 4.5: analysis of topography maps such as these allowed the direct calculation of N_0A and the volume of the nuclei as a function of time without recourse to modelling of any kind.

4.3 Conclusions

During the development of models for the multiple nucleation and diffusion controlled growth of electrodeposited materials, two main schools of thought have emerged. The first consider the use of equations (4.1) and (4.2) to be a well-

established principle, and generally apply the Avrami theorem to treat the overlap of diffusion zones. This has led to three relatively widely discussed models; those of Scharifker and Mostany, Sluyters-Rehbach, Wijenberg, Bosco and Sluyters, and Mirkin and Nilov/ Heerman and Tarallo. A range of other models based on similar principles also exist, with recent attempts focussing on modifications designed to better represent the underlying physical processes occurring. The second school of thought questions the validity of equation (4.1); in particular Fletcher recommends an independent method based on studying single nuclei on microelectrodes, while Milchev questions the principle of assuming a frozen energetic state of the electrode throughout the deposition process.

Computer simulation has also provided some useful insights, with the sophistication of the models used rapidly increasing. These have focussed on two areas: first, analysing the distribution of nuclei on a surface, including factors such as local nucleation exclusion zones, as well as more complex methods attempting to explicitly consider local concentration and potential profiles. Second, the diffusion to a growing nucleus has been modelled, using both 'brute force' and, increasingly, numerical methods.

In essence, the usefulness of any model depends on its ability to correctly model a real system, and by extension extract useful data from it. Methods are therefore required to directly analyse the processes occurring on the electrode surface. Traditionally, optical microscopy has been used, but recently the popularity of SPM techniques has increased, their increased resolution allowing determination of the size of deposits.

All three of these areas are the subject of considerable investigation, and hopefully a combination of the three methods combined with further advances should in the future provide a better understanding of the way in which materials nucleate and grow on electrodes.

4.4 References

[1] E. Budevski, G. Staikov, W. J. Lorenz, *Electrochim. Acta* **2000**, *45*, 2559.
[2] B. R. Scharifker, J. Mostany, *Encyclopedia of Electrochemistry* **2003**, *2*, 512.
[3] M. Y. Abyaneh, M. Fleischmann, *J. Electroanal. Chem.* **2002**, *530*, 108.
[4] M. Y. Abyaneh, M. Fleischmann, *J. Electroanal. Chem.* **2002**, *530*, 123.
[5] S. Fletcher, *J. Electroanal. Chem.* **2002**, *530*, 105.
[6] S. Fletcher, *J. Electroanal. Chem.* **2002**, *530*, 119.
[7] J. González-García, F. Gallud, J. Iniesta, V. Montiel, A. Aldaz, A. Lasia, *J. Electrochem. Soc.* **2000**, *147*, 2969.
[8] D. J. Astley, J. A. Harrison, H. R. Thirsk, *Trans. Faraday Soc.* **1967**, *64*, 192.
[9] N. A. Pangarov, S. Rashkov, *Compt. rend. acad. bulgare sci.* **1960**, *13*, 555.
[10] N. A. Pangarov, S. Rashkov, *Compt. rend. acad. bulgare sci.* **1960**, *13*, 439.
[11] M. Fleischmann, M. Liler, *Trans. Faraday Soc.* **1958**, *54*, 1370.
[12] M. Fleischmann, H. R. Thirsk, *Trans. Faraday Soc.* **1955**, *51*, 71.
[13] M. Fleischmann, H. R. Thirsk, *Electrochim. Acta* **1958**, *1*, 146.
[14] M. E. Hyde, R. G. Compton, *J. Electroanal. Chem.* **2002**, *531*, 19.
[15] S. Fletcher, C. S. Halliday, D. Gates, M. Westcott, T. Lwin, G. Nelson, *J. Electroanal. Chem.* **1983**, *159*, 267.
[16] G. J. Hills, D. J. Schiffrin, J. Thompson, *Electrochim. Acta* **1974**, *19*, 657.
[17] G. J. Hills, I. Montenegro, B. R. Scharifker, *J. Appl. Electrochem.* **1980**, *10*, 807.
[18] G. J. Hills, A. K. Pour, B. R. Scharifker, *Electrochim. Acta* **1982**, *28*, 891.
[19] B. R. Scharifker, G. J. Hills, *J. Electroanal. Chem.* **1981**, *130*, 81.
[20] A. Milchev, B. Scharifker, G. Hills, *J. Electroanal. Chem.* **1982**, *132*, 277.
[21] S. Toschev, A. Milchev, E. Vassileva, *Electrochim. Acta* **1976**, *21*, 1055.
[22] G. A. Gunawardena, G. Hills, I. Montenegro, B. Scharifker, *J. Electroanal. Chem.* **1982**, *138*, 225.
[23] B. Scharifker, G. Hills, *Electrochim. Acta* **1983**, *28*, 879.
[24] M. Avrami, *J. Chem. Phys.* **1939**, *7*, 1103.
[25] M. Avrami, *J. Chem. Phys.* **1940**, *8*, 212.
[26] E. Bosco, S. K. Rangarajan, *J. Electroanal. Chem.* **1982**, *134*, 213.
[27] E. Bosco, S. K. Rangarajan, *J. Electroanal. Chem.* **1982**, *134*, 225.
[28] B. Scharifker, J. Mostany, *J. Electroanal. Chem.* **1984**, *177*, 13.
[29] M. E. Hyde, R. Jacobs, R. G. Compton, *J. Phys. Chem. B.* **2002**, *106*, 11075.
[30] J. Yu, H. Cao, Y. Chen, L. Kang, H. Yang, *J. Electroanal. Chem.* **1999**, *474*, 69.
[31] M. E. Hyde, O. V. Klymenko, R. G. Compton, *J. Electroanal. Chem.* **2002**, *534*, 13.
[32] M. E. Hyde, R. G. Compton, *J. Electroanal. Chem.* **2005**, in press; doi: 10.1016/j.jelechem.2005.04.020.

[33] M. Sluyters-Rehbach, J. H. O. J. Wijenberg, E. Bosco, J. H. Sluyters, *J. Electroanal. Chem.* **1987**, *236*, 1.
[34] B. R. Scharifker, J. Mostany, M. Palomar-Pardave, I. Gonzalez, *J. Electrochem. Soc.* **1999**, *146*, 1005.
[35] Y. Cao, P. C. Searson, A. C. West, *J. Electrochem. Soc.* **2001**, *148*, C376.
[36] L. Heerman, A. Tarallo, *J. Electroanal. Chem.* **1999**, *470*, 70.
[37] M. V. Mirkin, A. P. Nilov, *J. Electroanal. Chem.* **1990**, *283*, 35.
[38] K. Márquez, G. Staikov, J. W. Schultze, *Electrochimica Acta* **2003**, *48*, 875.
[39] L. H. Mendoza-Huizar, J. Robles, M. Palomar-Pardave, *Journal of Electroanalytical Chemistry* **2003**, *545*, 39.
[40] L. H. Mendoza-Huizar, J. Robles, M. Palomar-Pardave, *Journal of the Electrochemical Society* **2005**, *152*, C265.
[41] S. Langerock, L. Heerman, *Journal of the Electrochemical Society* **2004**, *151*, C155.
[42] L. Heerman, E. Matthijs, S. Langerock, *Electrochim. Acta* **2001**, *47*, 905.
[43] P. A. Bobbert, M. M. Wind, J. Vlieger, *Physica A* **1987**, *146*, 69.
[44] E. Matthijs, S. Langerock, E. Michailova, L. Heerman, *Journal of Electroanalytical Chemistry* **2004**, *570*, 123.
[45] A. Milchev, E. Michailova, I. Lesigiarska, *Electrochem. Comm.* **2000**, *2*, 407.
[46] J. Mostany, J. Mozota, B. Scharifker, *J. Electroanal. Chem.* **1984**, *177*, 25.
[47] J. Mostany, J. Parra, B. R. Scharifker, *J. Appl. Electrochem.* **1986**, *16*, 333.
[48] Z. Grubac, M. Metikoš-Hukovic, *Electrochim. Acta* **1998**, *43*, 3175.
[49] A. G. Muñoz, S. B. Saidman, J. B. Bessone, *J. Appl. Electrochem.* **1999**, *29*, 1297.
[50] N. Vinokur, B. Miller, Y. Avyigal, R. Kalish, *J. Electrochem. Soc.* **1999**, *146*, 125.
[51] G. Oskam, P. M. Vereecken, P. C. Searson, *J. Electrochem. Soc.* **1999**, *146*, 1436.
[52] A. G. Muñoz, S. B. Saidman, J. B. Bessone, *J. Electrochem. Soc.* **1999**, *146*, 2123.
[53] J. C. Ziegler, R. I. Wielgosz, D. M. Kolb, *Electrochim. Acta* **1999**, *45*, 827.
[54] D. R. Salinas, E. O. Cobo, S. G. Garcia, J. B. Bessone, *J. Electroanal. Chem.* **1999**, *470*, 120.
[55] F. Gloaguen, J. M. Léger, C. Lamy, A. Marmann, U. Stimming, R. Vogel, *Electrochim. Acta* **1999**, *44*, 1805.
[56] E. Barrera, M. Palomar-Padarvé, N. Batina, I. Gonzalez, *J. Electrochem. Soc.* **2000**, *147*, 1787.
[57] H. Cesiulis, M. Ziomek-Moroz, *J. Appl. Electrochem.* **2000**, *30*, 1261.
[58] M. C. Lefebvre, B. E. Conway, *J. Electroanal. Chem.* **2000**, *480*, 46.
[59] G. Oskam, P. C. Searson, *J. Electrochem. Soc.* **2000**, *147*, 2199.
[60] G. Oskam, P. C. Searson, *Surf. Sci.* **2000**, *446*, 103.
[61] G. Sandmann, H. Dietz, W. Plieth, *J. Electroanal. Chem.* **2000**, *491*, 78.
[62] A. N. Correia, S. A. S. Machado, L. A. Avaca, *J. Electroanal. Chem.* **2000**, *488*, 110.
[63] P. M. Hoffmann, A. Radisic, P. C. Searson, *J. Electrochem. Soc.* **2000**, *147*, 2576.
[64] G. Trejo, H. Ruiz, R. Ortega Borges, Y. Meas, *J. Appl. Electrochem.* **2001**, *31*, 685.
[65] M. Miranda-Hernández, I. González, N. Batina, *J. Phys. Chem. B* **2001**, *105*, 4214.

[66] A. Ramos, M. Miranda-Hernández, I. Gonzalez, *J. Electrochem. Soc.* **2001**, *148*, C315.
[67] C. Ehlers, U. König, G. Staikov, J. W. Schultze, *Electrochim. Acta* **2001**, *47*, 379.
[68] C. Ji, G. Oskam, P. C. Searson, *Surf. Sci.* **2001**, *492*, 115.
[69] C. Ji, G. Oskam, P. C. Searson, *J. Electrochem. Soc.* **2001**, *148*, C746.
[70] R. Schrebler, P. Cury, M. Orellana, H. Gómez, R. Córdova, E. A. Dalchiele, *Electrochim. Acta* **2001**, *46*, 4309.
[71] A. Radisic, A. C. West, P. C. Searson, *J. Electrochem. Soc.* **2002**, *149*, C94.
[72] M. E. Quayam, S. Ye, K. Uosaki, *J. Electroanal. Chem.* **2002**, *520*, 126.
[73] Z. Grubac, M. Metikoš-Hukovic, *Thin Solid Films* **2002**, *413*, 248.
[74] S. Floate, M. E. Hyde, R. G. Compton, *J. Electroanal. Chem.* **2002**, *523*, 49.
[75] D. Grujicic, B. Pesic, *Electrochim. Acta* **2002**, *47*, 2901.
[76] L. O. S. Bulhoes, L. H. Mascaro, *Journal of Solid State Electrochemistry* **2004**, *8*, 238.
[77] D. Grujicic, B. Pesic, *Electrochimica Acta* **2002**, *47*, 2901.
[78] M. Gu, L. Huang, F.-Z. Yang, S.-B. Yao, S.-M. Zhou, *Transactions of the Institute of Metal Finishing* **2002**, *80*, 183.
[79] S. B. Kim, K. T. Kim, C. J. Park, H. S. Kwon, *Journal of Applied Electrochemistry* **2002**, *32*, 1247.
[80] A. E. Alvarez, D. R. Salinas, *Journal of Electroanalytical Chemistry* **2004**, *566*, 393.
[81] O. Chyan, T. N. Arunagiri, T. Ponnuswamy, *Journal of the Electrochemical Society* **2003**, *150*, C347.
[82] A. N. Correia, M. C. dos Santos, S. A. S. Machado, L. A. Avaca, *Journal of Electroanalytical Chemistry* **2003**, *547*, 53.
[83] P. He, H. Liu, Z. Li, J. Li, *Journal of the Electrochemical Society* **2005**, *152*, E146.
[84] P. He, H. Liu, Z. Li, Y. Liu, X. Xu, J. Li, *Langmuir* **2004**, *20*, 10260.
[85] S. Lichusina, E. Ivaskevic, D. Simkunaite, A. Steponavicius, *Chemija* **2004**, *15*, 29.
[86] K. Raeissi, A. Saatchi, M. A. Golozar, *Transactions of the Institute of Metal Finishing* **2003**, *81*, 186.
[87] K. Raeissi, A. Saatchi, M. A. Golozar, *Journal of Applied Electrochemistry* **2003**, *33*, 635.
[88] F. D'Eramo, J. M. Marioli, A. H. Arevalo, L. E. Sereno, *Talanta* **2003**, *61*, 341.
[89] E. Gómez, E. Guaus, F. Sanz, E. Vallés, *J. Electroanal. Chem.* **1999**, *465*, 63.
[90] A. Serruya, J. Mostany, B. Scharifker, *J. Electroanal. Chem.* **1999**, *464*, 39.
[91] M. E. Hyde, R. M. J. Jacobs, R. G. Compton, *Journal of Electroanalytical Chemistry* **2004**, *562*, 61.
[92] S. B. Emery, J. L. Hubbley, D. Roy, *Journal of Electroanalytical Chemistry* **2004**, *568*, 121.
[93] A. Milchev, L. Heerman, *Electrochimica Acta* **2003**, *48*, 2903.
[94] A. Milchev, D. Stoychev, V. Lazarov, A. Papoutsis, G. Kokkinidis, *J. Crystal Growth* **2001**, *226*, 138.
[95] M. Arbib, B. Zhang, V. Lazarov, D. Stoychev, A. Milchev, C. Buess-Herman, *J. Electroanal. Chem.* **2001**, *510*, 67.
[96] S. Langerock, H. Menard, P. Rowntree, L. Heerman, *Langmuir* **2005**, *21*, 5124.

[97] P. Diaz-Arista, Y. Meas, R. Ortega, G. Trejo, *Journal of Applied Electrochemistry* **2005**, *35*, 217.
[98] E. Gomez, Z. G. Kipervaser, E. Valles, *Journal of Electroanalytical Chemistry* **2003**, *557*, 9.
[99] E. Gomez, Z. G. Kipervaser, E. Pellicer, E. Valles, *Physical Chemistry Chemical Physics* **2004**, *6*, 1340.
[100] P. C. T. D'Ajello, M. L. Munford, A. A. Pasa, *J. Chem. Phys.* **1999**, *111*, 4267.
[101] P. C. T. D'Ajello, M. A. Fiori, A. A. Pasa, Z. G. Kipervaser, *J. Electrochem. Soc.* **2000**, *147*, 4562.
[102] A. Milchev, E. Michailova, *Electrochem. Comm.* **2000**, *2*, 15.
[103] R. L. Deutscher, S. Fletcher, *J. Chem. Soc., Faraday Trans.* **1998**, *94*, 3527.
[104] S. Chen, A. Kucernak, *Journal of Physical Chemistry B* **2003**, *107*, 8392.
[105] V. A. Isaev, A. N. Baraboshkin, *J. Electroanal. Chem.* **1994**, *377*, 33.
[106] A. N. Kolmogorov, *Bull. Acad. Sci. URSS Sci. Math. Nat.* **1937**, *3*, 355.
[107] P. C. D'Ajello, *Journal of Electroanalytical Chemistry* **2004**, *573*, 29.
[108] P. C. T. D'Ajello, A. Q. Schervenski, *Journal of Electroanalytical Chemistry* **2004**, *573*, 37.
[109] B. Scharifker, *J. Electroanal. Chem.* **1998**, *458*, 253.
[110] G. Nagy, G. Denuault, *J. Electroanal. Chem.* **1997**, *433*, 175.
[111] M. Tokuyama, *Physica A* **1990**, *169*, 147.
[112] M. Tokuyama, Y. Enomoto, *J. Chem. Phys.* **1990**, *94*, 8234.
[113] M. Tokuyama, Y. Enomoto, *Physica A* **1995**, *220*, 261.
[114] W. H. Mulder, J. H. O. J. Wijenberg, M. Sluyters-Rehbach, J. H. Sluyters, *J. Electroanal. Chem.* **1989**, *270*, 7.
[115] A. Milchev, W. S. Kruijt, M. Sluyters-Rehbach, J. H. Sluyters, *J. Electroanal. Chem.* **1993**, *362*, 21.
[116] W. S. Kruijt, M. Sluyters-Rehbach, J. H. Sluyters, A. Milchev, *J. Electroanal. Chem.* **1994**, *371*, 13.
[117] V. Tsakova, A. Milchev, *J. Electroanal. Chem.* **1998**, *451*, 211.
[118] J. Mostany, A. Serruya, B. R. Scharifker, *J. Electroanal. Chem.* **1995**, *383*, 37.
[119] A. Milchev, *J. Chem. Phys.* **1994**, *100*, 5160.
[120] A. Serruya, J. Mostany, B. R. Scharifker, *J. Chem. Soc., Faraday Trans.* **1993**, *89*, 255.
[121] B. Scharifker, J. Mostany, A. Serruya, *Electrochim. Acta* **1992**, *37*, 2503.
[122] Y. D. Gamburg, *Russian Journal of Electrochemistry (Translation of Elektrokhimiya)* **2003**, *39*, 318.
[123] Y. D. Gamburg, *Russian Journal of Electrochemistry (Translation of Elektrokhimiya)* **2004**, *40*, 78.
[124] Y. D. Gamburg, *Russian Journal of Electrochemistry (Translation of Elektrokhimiya)* **2004**, *40*, 215.
[125] R. Kaischev, B. Mutaftschiev, *Electrochim. Acta* **1964**, *9*, 1203.
[126] I. Markov, *Thin Solid Films* **1976**, *35*, 11.
[127] I. Markov, D. Kashchiev, *J. Crystal Growth* **1972**, *16*, 170.
[128] I. Markov, E. Stoycheva, *Thin Solid Films* **1976**, *35*, 21.
[129] S. Fletcher, *J. Electroanal. Chem.* **1986**, *215*, 1.
[130] A. Milchev, *J. Electroanal. Chem.* **1998**, *457*, 35.
[131] A. Milchev, *J. Electroanal. Chem.* **1998**, *457*, 47.
[132] R. L. Deutscher, S. Fletcher, *J. Electroanal. Chem.* **1988**, *239*, 17.
[133] R. L. Deutscher, S. Fletcher, *J. Electroanal. Chem.* **1990**, *277*, 1.

[134] S. Fletcher, in *Microelectrodes: Theory and Applications* (Eds.: M. I. Montenegro, M. A. Queiros, J. L. Daschbach), Kluwer Academic Publishers, Dordrecht, **1991**, pp. 341.
[135] J. H. Sluyters, E. Bosco, M. Sluyters-Rehbach, *J. Electroanal. Chem.* **1988**, *241*, 79.
[136] J. H. Sluyters, J. H. O. J. Wijenberg, W. H. Mulder, M. Sluyters-Rehbach, D. Bedeaux, *J. Electroanal. Chem.* **1989**, *261*, 263.
[137] J. L. Frasnaer, R. M. Penner, *J. Phys. Chem. B* **1999**, *103*, 7643.
[138] M. Trias, E. Vilaseca, *Journal of Electroanalytical Chemistry* **2004**, *569*, 95.
[139] E. García-Pastoriza, J. Mostany, B. Scharifker, *J. Electroanal. Chem.* **1997**, *441*, 13.
[140] G. Nagy, Y. Sugimoto, G. Denuault, *J. Electroanal. Chem.* **1997**, *433*, 167.
[141] L. Heerman, A. Tarallo, *J. Electroanal. Chem.* **1998**, *455*, 265.
[142] R. M. Penner, *J. Phys. Chem. B* **2001**, *105*, 8672.
[143] E. Vilaseca, P. Pablo Trigueros, J. Lluis Garces, F. Mas, *J. Electroanal. Chem.* **1998**, *458*, 55.
[144] M. Zheng, A. C. West, *Journal of the Electrochemical Society* **2004**, *151*, C502.
[145] Y. Cao, A. C. West, *J. Electroanal. Chem.* **2001**, *514*, 103.
[146] V. S. Sochnikov, S. Efrima, *J. Phys. Chem. B* **2002**, *106*, 11993.
[147] T. J. Pricer, M. J. Kushner, R. C. Alkire, *J. Electrochem. Soc.* **2002**, *149*, C396.
[148] U. Hasse, K. Wagner, F. Scholz, *Journal of Solid State Electrochemistry* **2004**, *8*, 842.
[149] H. Liu, R. M. Penner, *J. Phys. Chem. B* **2000**, *104*, 9131.
[150] R. Knake, W. Fahmi Amir, A. M. Tofail Syed, J. Clohessy, M. Mihov, J. Cunnane Vincent, *Langmuir* **2005**, *21*, 1001.
[151] A. A. Gewirth, B. K. Niece, *Chem. Rev.* **1997**, *97*, 1129.
[152] M. B.W., L. H. Xiong, X. W. Cai, *J. Electroanal. Chem.* **1996**, *416*, 145.

5 Anodic Stripping Voltammetry: An AFM Study of Some Problems and Limitations

This chapter cannot be made freely available via ORA for copyright reasons. The content has been published as Hyde, M. E., Banks C. E. & Compton, R. G. (2004). 'Anodic stripping voltammetry: an AFM study of some problems and limitations', Electroanalysis, 16(5), 345-354. [Available at http://dx.doi.org/10.1002/elan.200302863].

6 Nucleation and Growth of Silver on Boron-Doped Diamond Electrodes

6.1 Introduction

The use of boron-doped diamond (BDD) electrodes is of considerable interest in areas such as anodic stripping voltammetry, as the extreme flatness and hardness of the electrode surface provides potentially better reliability and reproducibility for analytical studies than for example glassy carbon electrodes (see Compton et al.[1] and references therein). BDD also allows use of a wider potential window. Relatively few fundamental studies of metal deposition on BDD have been attempted.[2-5] The same features that make BDD a useful analytical substrate also favour such studies; the flatness of the surface has previously been exploited in in-situ AFM (atomic force microscopy) studies of growing nuclei,[2] while, as the present study shows, the relatively uniform appearance and reflectivity of the surface facilitates optical microscopic investigation.

The aim of the work presented in this chapter was to deposit silver on to the BDD electrode, and to characterize the deposition process using voltammetric and optical methods. The deposition of silver on to carbon electrodes has been extensively studied on glassy carbon macroelectrodes[6, 7] as well as HOPG (highly ordered pyrolytic graphite) surfaces[8, 9] and carbon fibre microelectrodes.[10-12] Particularly, silver is a popular system when investigating fundamental aspects of nucleation theory as its deposition has been shown to be under diffusion control (at concentrations and potentials similar to those studied in this chapter).[13-15]

Optical microscopy is a common method for studying the properties of nuclei on electrode surfaces, as it allows direct observation of the number and distribution of particles. It has therefore been commonly used to investigate the nucleation rate (e.g. [16]) and the spatial distribution of deposited clusters, in particular nearest neighbour distances[17-19] and pair correlation functions.[20] In the work reported in this chapter, we attempt to determine nucleation rates using this method and compare them with values derived using voltammetric methods. Nearest neighbour distances are studied as a function of time.

Analyses of silver particle size distributions have been carried out ITO (indium tin oxide) electrodes,[21] hydrogen terminated silicon (100),[22] and on HOPG.[23] In the case of HOPG, however, the aim of the experiments was to develop methods for depositing uniformly sized particles (depositing in the 'uncoupled limit'). In the present work we attempt an analysis of the distribution of nucleus sizes under conditions typical of nucleation / growth experiments, in which nucleus growth rates may be limited by inhibition from surrounding interacting clusters.

The distribution of nearest neighbour distances has been studied by the use of stochastic simulations of varying complexity.[24-26] Finally in the following work, we develop a simple two-dimensional model of the appearance and growth of nuclei on an electrode surface and use it to qualitatively interpret the area distributions found in the deposited silver particles.

6.2 Experimental Details

The reagents used were: silver nitrate (Sigma, 99%+) and nitric acid (Aldrich, 70%, AR grade). Three aqueous based solutions were used: 1mM $AgNO_3$ / 0.1M HNO_3, 500μM $AgNO_3$ / 0.1M HNO_3, and 250μM $AgNO_3$ / 0.1M HNO_3. These concentrations of silver nitrate were chosen as follows: it was observed that solutions having concentrations of higher than 1mM $AgNO_3$ deposited silver to such an extent that resolving individual nuclei was difficult, while concentrations much lower than 250μM generated no visible deposits on the timescale of the experiments (see below for more precise details).

In all experiments, a silver wire was used as the reference electrode. The potential of the silver wire was measured vs. a SCE over a range of $AgNO_3$ concentrations between 250μM and 5mM, and showed a potential response of ca 61mV per decade at 25°C. All potentials reported in this chapter are therefore measured vs. the equilibrium potential for Ag/Ag^+ in the particular concentration of Ag^+ employed.

All optical images were obtained using a Digital Instruments OMV-PAR microscope based on a Sony XC-999P CCD (charge coupled device) camera, having a maximum resolution of 752 x 582 pixels over an area of 540 x 400 μm, connected to a Hauppauge video capture card. All images used in the following analyses were of the maximum size allowed by the camera, in order to minimize any loss of resolution.

6.3 Nucleus Number as a Function of Time

In order to examine the rate of nucleation, in-situ deposition was performed as described in chapter 3. The potentiostat was first held at open circuit after which the working electrode was set at a potential in the range –0.05 V and –0.25 V vs. Ag/Ag^+ (see experimental section, above). Video capture of 8 bit greyscale images was started simultaneously at a rate of 1 frame per second. In each case the potential was applied for 60s. The experiment was repeated at all three concentrations of $AgNO_3$ studied (1mM, 500μM and 250μM). An example of the images obtained is shown in figure 6.1.

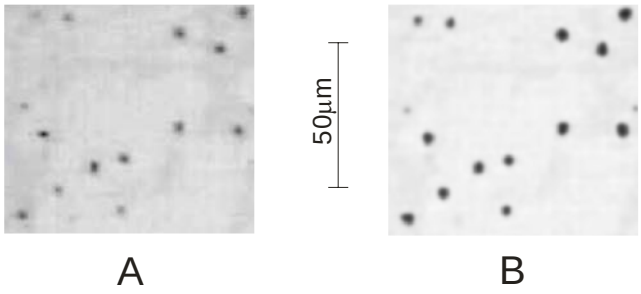

Figure 6.1: A) Part of an in-situ image of silver electrochemically deposited on BDD after deposition at –100mV for 60s in a 1mM $AgNO_3$ solution. B) The same area of the electrode after removal from the deposition solution, rinsing and drying. Note the lack of any perceptible change in the number or positions of nuclei, but the improved image clarity.

A baseline image (the first in each set) was subtracted from each image in order to enhance the contrast of the silver nuclei and reduce any error due to colouration of the clean electrode surface. The total number and position of each visible nuclei in each image was then determined, using home-designed software (copies available from the authors on request) employing a procedure in which continuous areas of the image darker than a manually set threshold were counted as a nucleus. The centre of the nucleus was determined simply by finding the mean of the maximum and minimum x

and y points in the continuous area. This method produces accurate numbers and positions if the nuclei have an approximately circular profile, and are separated enough to be resolvable.

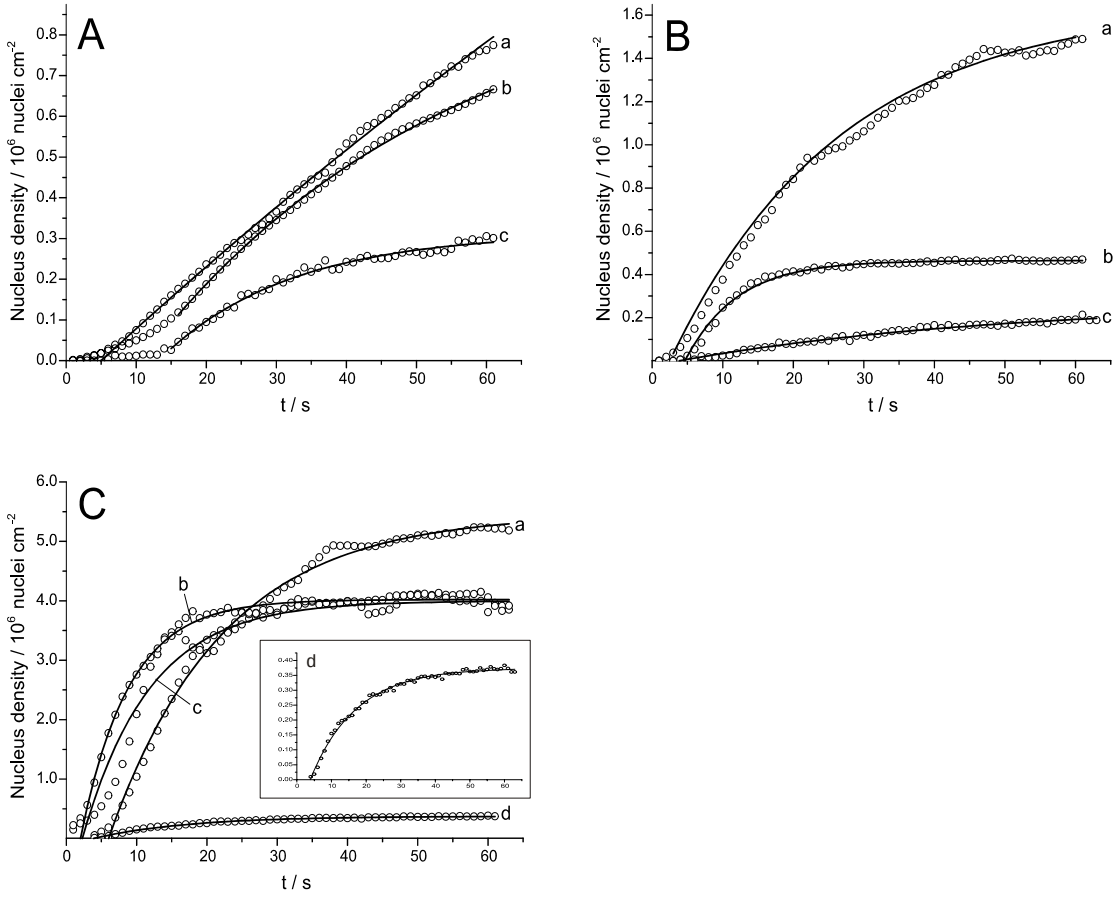

Figure 6.2: Nucleus number density as a function of time extracted from analysis of electrode images. Open circles show experimental data, solid lines show optimized fits. Conditions: A) 250µM $AgNO_3$ solution, a) -200mV, b) –150mV, c) –100mV. B) 500µM solution, a) -200mV, b) –150mV, c) –100mV. C) 1mM solution a) -200mV, b) –150mV, c) –100mV, d) –50mV. The inset in C) shows the -50mV data on an extended scale; note that similar experiments were performed at 250µM and 500µM but not enough nuclei were generated for meaningful analysis.

As figure 6.1 shows, the nuclei observed were in fact mostly circular, and the threshold was empirically determined to give maximum nucleus sizes, while still ensuring both removal of image noise and sufficient separation of the nuclei. The threshold was set to the same value for the analysis of all experiments.

The nucleus numbers extracted by this procedure are plotted as a function of time in figure 6.2. In all cases, the general trend is the same; after an induction period of up to 15 seconds, there is a steep increase in nucleus number, followed by a plateau. The first of these features, the induction time, is commonly observed in nucleation experiments. It corresponds to nucleation before a steady state is achieved (the linear section of the curve),[27, 28] possibly resulting from changes in the energetic state of the electrode surface during the process of nucleus formation.[29, 30] The plateau corresponds to the saturation nucleus density, N_{sat}. In cases where saturation was not observed on the time scale of the experiment, the values of N_{sat} were determined by extrapolation using Microcal Origin software (solid lines on figure 6.2). These observed values of N_{sat} are plotted as solid points and dashed lines on figure 6.4.

An interesting feature of N_{sat} is that it allows an estimate to be made of the total number of active sites available for nucleation on the electrode surface, N_0. Qualitatively, we expect N_{sat} to be lower than N_0, because as nuclei appear on active sites, diffusion to them decreases the local concentration of depositing species. 'Exclusion zones' are generated, in which further nucleation is inhibited. The number of sites available for nucleation at any time $t > 0$ is therefore less than would be predicted solely from the progressive occupation of active sites. Gunawardena et al.[31] show that N_{sat} can be related to N_0 by finding the probability that a given nucleation site is not covered by a diffusion zone, then integrating this result up to time t. In the limit $t \to \infty$, this gives

$$N_{sat} = \left(\frac{N_0 A}{2k'D} \right)^{\frac{1}{2}} \qquad (6.1)$$

in which $k' = (4/3)(8\pi cM/\rho)^{1/2}$. A is the nucleation rate constant, expressed as a rate per active site. D is the diffusion coefficient, c the concentration of depositing species, M the molar mass, and ρ the density. Equation (6.1) suggests an additional way of determining N_{sat}: at small times, the effects of diffusion zones may be unimportant, and hence the initial gradients of the curves in figure 6.2 may correspond to N_0A. Linear best fits were therefore found for the initial rising section of the curves, and the corresponding N_{sat} calculated using, as in all subsequent calculations, a value of 1.7×10^{-5} cm^2 s^{-1} for D,[32] and 10.49 g cm^{-3} for ρ. These values of N_{sat} are plotted in figure 6.4 as open points and solid lines. We find that in all cases, the values of N_{sat} calculated from initial gradients are much lower than the observed values, implying that inhibition of active sites becomes an important factor very rapidly on the timescale of the experiment.

Another well established method for estimating N_0 and A is via the analysis of potentiostatic current transients associated with the deposition process.[31, 33-37] Transients corresponding to each set of deposition conditions shown in figure 6.2 were each recorded 5 times for averaging purposes. All voltammograms showed common features: an induction time (see above), followed by an increase to a maximum, followed by decay towards a limiting current. This current profile suggested that analysis using, for example, the Scharifker and Mostany equation[38] may be appropriate. However, as observed previously,[2] although good fits to the data could be achieved by optimizing parameters related to N_0 and A, it was impossible to extract unique values for the two parameters because a range of pairs of values of N_0 and A gave curves with essentially the same shape. The following

approximation, valid in the absence of nucleation inhibition, was therefore used to attempt to extract values of the global nucleation rate, N_0A:

$$j = \left[\sqrt{2} zF\pi (Dc)^{3/2} \left(\frac{M}{\rho} \right)^{1/2} N_0 A \right] . (t - t_0)^{3/2} \qquad (6.2)$$

in which j is the current density, z is the ionic charge of the depositing species, F is the Faraday constant, and t_0 is the induction time. For each of the voltammetric datasets, ln (j) was plotted against ln ($t-t_0$), and the gradient of the linear, rising section determined (as shown in figure 6.3). If equation (6.2) is valid, a gradient of 1.5 should be observed. In fact, at -0.20V, the gradient was found to be around 1 at each concentration, rising to roughly 1.5 at -0.05V. This lowered gradient implies inhibition is reducing the current density at a given time, and that equation (6.2) will not accurately predict N_0A. To test this conclusion, N_{sat} was again calculated, this time from the values of N_0A found from the intercept of the ln (j) – ln ($t-t_0$) plots, and the resultant values of N_{sat} plotted on figure 6.4 (crossed points and dotted lines). We find that again the N_{sat} values are lower than the observed values, but that they are in fair agreement with the values computed from initial gradients. Interestingly, at 1mM and -0.05V, the observed and voltammetric values of N_{sat} are in good agreement, implying that equation (6.2) works well in this case; this is consistent with the corresponding ln (j) – ln ($t-t_0$) plot having a gradient of close to 1.5.

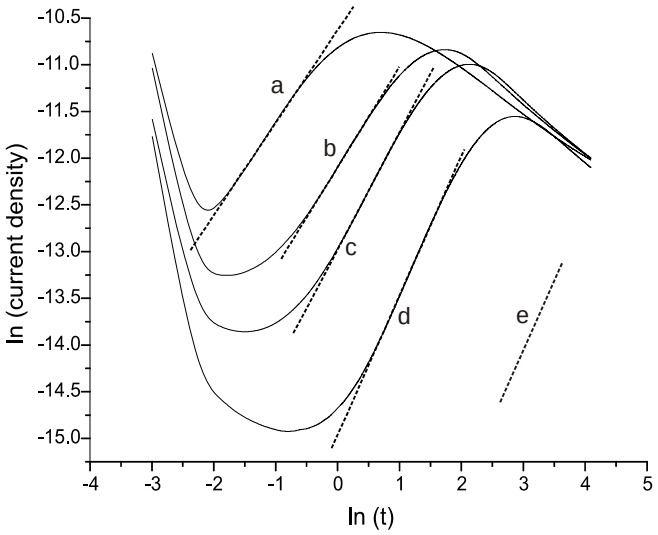

Figure 6.3: Example ln (j) vs. ln (t) plot for potentiostatic current transients recorded during the experiments generating the data shown in figure 6.2. Solid lines show experimental data, dashed lines show optimized fits to the linear part of the transient. Conditions: 250µM $AgNO_3$ solution, a) -200mV, b) –150mV, c) –100mV, d) –50mV. e) shows a line having a gradient 1.5 for comparison purposes.

Another observation of interest is the variability of the deposition transients; as is evident from the error bars for the voltammetric data in figure 6.4, the values of N_0A extracted from the 5 electrochemical experiments were erratic, sometimes varying from the mean by factors of 10 or more. It appears that these fluctuations were the result of the polishing process used on the working electrode before each scan; when the voltammetry was repeated without removing the electrode from the solution between scans, instead removing the deposited silver using anodic stripping (ASV), much more consistent results were observed. However, it was also observed that not all the visible deposits on the electrode could be removed using ASV, making this method of electrode pre-treatment unsuitable for the optical experiments.

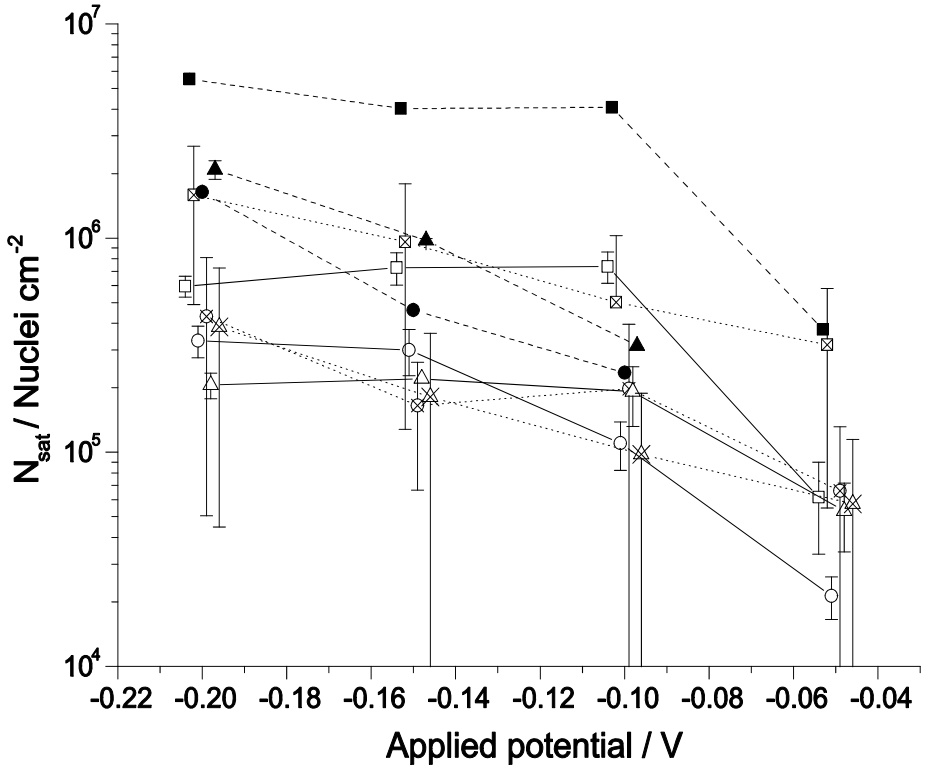

Figure 6.4: Saturation nucleus number density, N_{sat}, plotted as a function of applied potential. Squares – 1mM solution, circles – 500µM solution, triangles – 250µM solution. Solid points and dashed lines show observed values. Open points and solid lines show values derived from the initial gradients in figure 6.2. In these cases, the error bars show the error computed from the optimization calculation. Crossed points and dotted lines show values derived from voltammetric data. In this case, the error bars show ±1 standard deviation. Note that the points are staggered to clarify the position of the error bars; in fact all measurements were made at -0.20, -0.15, -0.10 and -0.05V.

6.4 In-Situ Analysis of Nearest Neighbour Distances

Using the nucleus position data collected in the analysis of the experiments described in section 1, nearest neighbour distances (NNDs) for each nucleus were calculated. In order to prevent any artefacts resulting from nuclei outside the image appearing, those nuclei closer to the edge of the image than $(\pi\nu)^{-1/2}$ were excluded, a distance corresponding to twice the most probable distance between Poisson nearest neighbours, in which ν is the number density of particles in the image.[24] Typically, nearest neighbour distances are compared with those arising from a Poisson distribution having the same number density of particles: a Poisson distribution

implies that the position of any particle is entirely independent of that of its neighbours, and any deviations from this in the observed distribution indicate correlation of some kind between the nuclei.

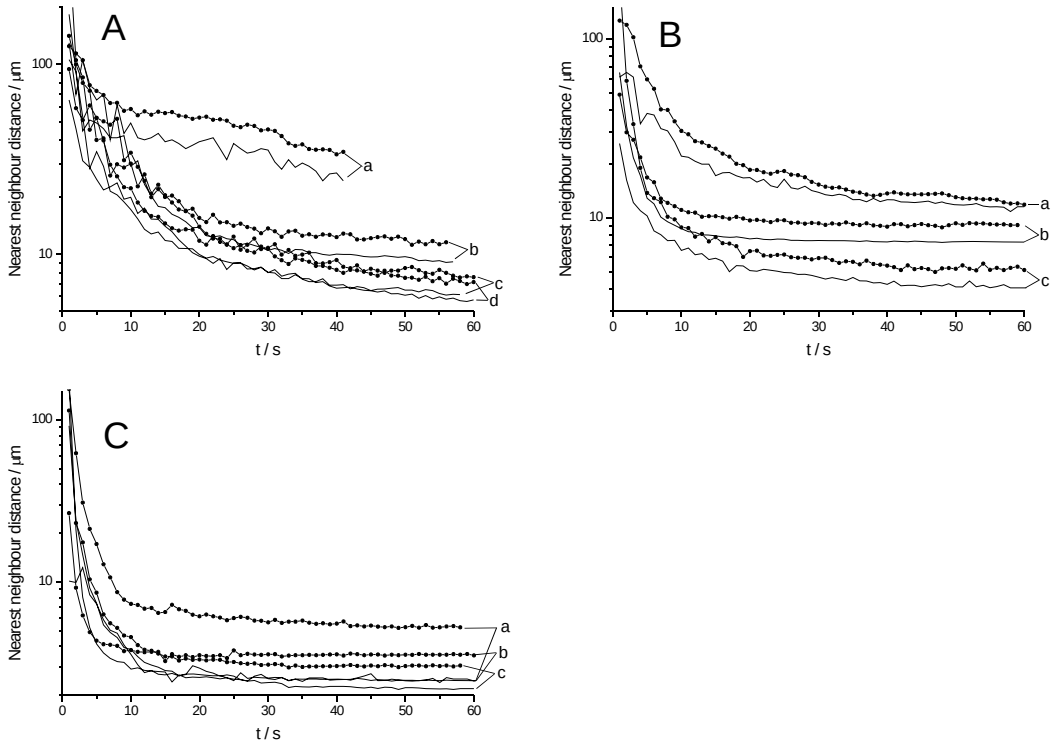

Figure 6.5: Mean nearest neighbour distances plotted as a function of time under conditions A) 250μM $AgNO_3$ solution, a) -200mV, b) –150mV, c) –100mV, d) –50mV. B) 500μM solution, a) -200mV, b) –150mV, c) –100mV, d) –50mV. C) 1mM solution a) -200mV, b) –150mV, c) –50mV. Lines with data points show experimental data; solid lines show the mean nearest neighbour distances for a Poisson distribution with the same number density of particles as the corresponding experimental point.

The mean NNDs extracted from the experimental data are plotted as a function of time in figure 6.5, and compared with the Poisson expression for the mean NND:[24]

$$\bar{d} = \frac{1}{2\nu^{1/2}} \tag{6.3}$$

where the values of ν used were those collected in the previous section (figure 6.2). It can be seen that in every case (after the initial fluctuations caused by low nucleus

densities at small times) the observed nearest neighbour distance are larger than those calculated for a Poisson distribution having the same number density. This indicates a skew in the distribution: fewer nuclei appear at small separations, and more at larger separations, which is precisely what would be expected if 'exclusion zones' were appearing around growing nuclei, impeding the appearance of new nuclei close to established ones. This correlation is investigated further in the next section.

6.5 Ex-Situ Analysis of NNDs

In order to study the final distribution of nuclei in more detail, deposition was repeated for the sets of conditions described above. This time, however, instead of imaging in-situ, the electrode was removed from the solution, rinsed with UHQ water and dried with nitrogen before being examined in air. The absence of solution and glass between the electrode and microscope allowed clearer images to be obtained, and in this case it was possible to calculate not only the NNDs after 60s, but also the approximate nucleus areas (see the next section). In each case, 10 images were collected from different points on the electrode and the results averaged to ensure that the results were representative of the electrode as a whole.

A concern when using ex-situ methods is the possibility that removing the surface to be studied from solution will alter the morphology of the deposits in some way (for example, by washing away poorly adherent nuclei during rinsing). To investigate this, silver was deposited on to the electrode in-situ, and an image captured. The electrode was rinsed and dried as normal, and then the same area imaged ex-situ. Parts of the two images are compared in figure 6.1; it would appear that there is no change to the number or distribution of nuclei during removal from the solution, and

that the results presented below are therefore likely to be a true representation of the electrode surface during deposition.

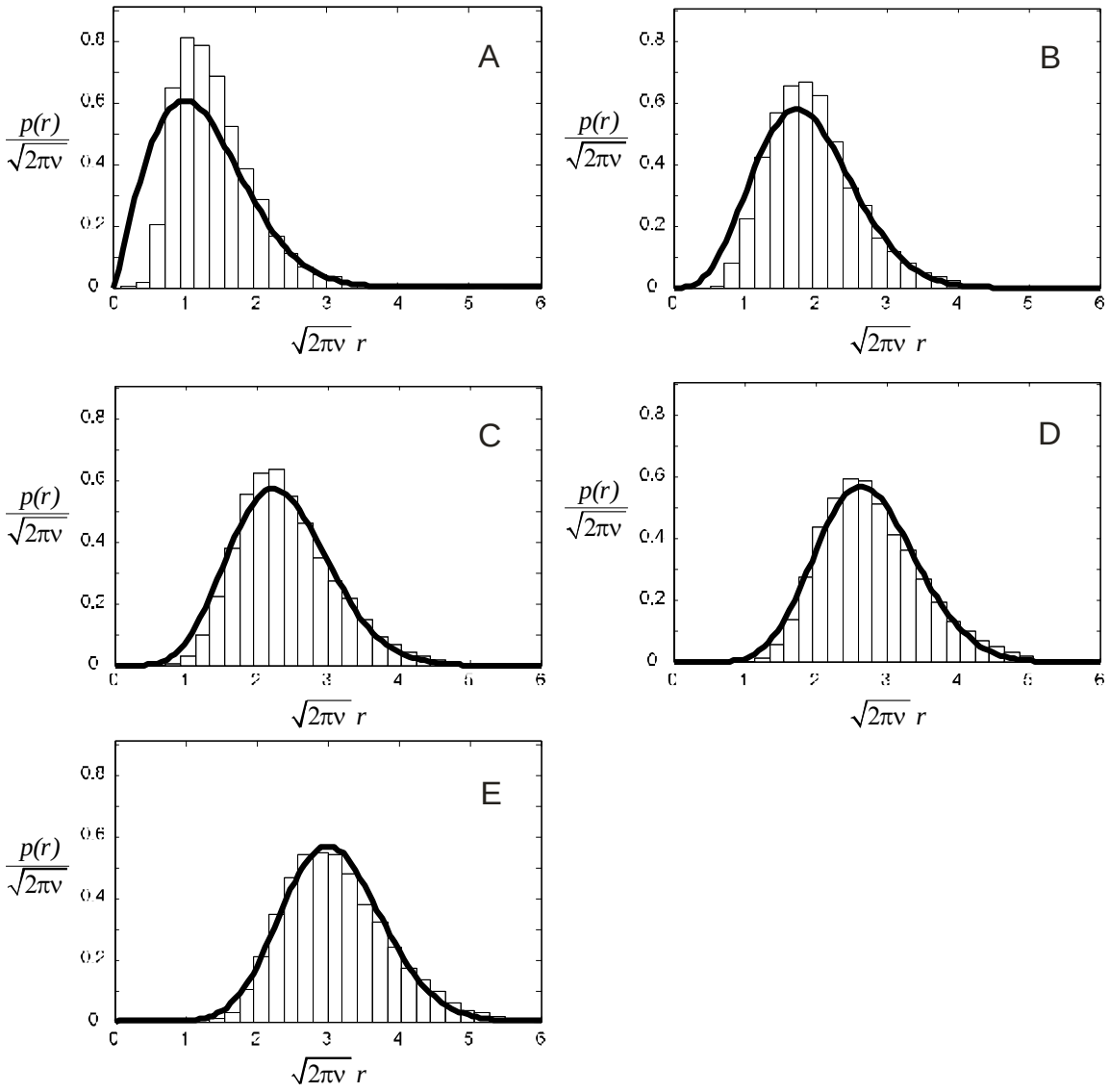

Figure 6.6: Histograms showing reduced nearest neighbour distributions for nuclei deposited on BDD from a 500μM solution of $AgNO_3$ at -0.2V for 60s. Figures A-E show the 1st through 5th nearest neighbour distribution; bars show the experimental data, while the line shows a Poisson distribution for the same number density of nuclei. p(r) is the probability of a nucleus having a nearest neighbour at a distance r.

Plotted in figure 6.6 are the first through fifth nearest neighbour distributions after 60s deposition from a 500μM $AgNO_3$ solution at -0.2V. Note that the distributions have been reduced to units of $(2\pi\nu)^{-1/2}$, following the convention of Scharifker et al.[24] This removes any effect of total particle density from the distribution, representing

only the way in which the particles are arranged relative to each other in the plane of the electrode, simplifying the process of comparing the sets of data collected at different concentrations and potentials. For comparison purposes, a reduced Poisson distribution, corresponding to the equation

$$\frac{1}{\sqrt{2\pi\nu}}\,p(r)=\sqrt{2\pi\nu}\,r\exp\left[-\frac{1}{2}\left(\sqrt{2\pi\nu}\,r\right)^2\right] \tag{6.4}$$

is also shown. Again, it was necessary to exclude from the distributions those particles which were too close to the image edge to ensure all nearest neighbours were also in the image. The definition of 'too close' is now (for the nth nearest neighbour):[20]

$$\left(\frac{2n-1}{\pi\nu}\right)^{1/2} \tag{6.5}$$

The form of the reduced distribution obtained for each dataset was essentially independent of applied potential between -0.05V and -0.2V and concentration between 250μM and 1mM, except that higher potentials and concentrations produced smoother curves due to the larger total number of particles analyzed (see the section on simulation below). In terms of the shape of the distribution, it can be seen that there is a significant skew towards larger distances in the first NND, confirming that inhibition of new nuclei appearing close to established nuclei is occurring. The second NND shows a similar, but reduced effect, while the third through fifth NNDs show little or no deviation from the Poisson curve. This resembles closely the observations of Kruijt et al.,[17] who studied the deposition of mercury on glassy carbon. They found that given an excess of supporting electrolyte, the most probable nearest neighbour distance was significantly greater than that for a Poisson distribution, and appeared with approximately a 60% higher probability, compared to roughly 45% greater in the present experiments. The correlations they observed

decreased rapidly, until the third nearest neighbour distribution was Poissonian, again as observed in the present experiments. On the other hand, the nucleation of lead on glassy carbon has been studied by Mostany et al.,[20] who found that the mean nearest neighbour distributions for the first to fifth nearest neighbours had most probable distances which were all significantly larger than predicted by a Poisson distribution. This effect was also shown to extend to the 15th nearest neighbour, potentially implying some kind of long-range order in the deposit. However, their analysis of pair correlation functions showed no evidence for this, a conclusion that our analysis supports.

6.6 Ex-Situ Analysis of Nucleus Areas

In the analysis of nucleus area, a slightly different experimental technique was employed. Clearly the area of a nucleus is a function of time, even after the number of nuclei has saturated (unlike the nearest neighbour distribution, which remains the same after saturation). The length of time for which deposition occurs is therefore more critical. It was decided to deposit until the current maximum appeared in the potentiostatic transient, a time characteristic of the specific deposition conditions. The distributions shown in figure 6.7 are therefore those after a significant number of nuclei have appeared, but while the appearance rate is near maximal - figures 6.7A and B respectively show histograms of the nucleus areas at a silver concentration of 250μM and 500μM and potentials between 50mV and 200mV. Note that the two datasets show similar features – at 50mV, both have large populations close to $a/a_{mean} = 0$, decreasing steadily to zero with increasing a/a_{mean} (where a/a_{mean} is the nucleus area reduced with respect to the mean area for the relevant dataset). With increasing potential, the peak broadens and starts to move towards larger values of a/a_{mean}.

Unlike the NND, there is no simple expression to which these distributions can be compared; not only are they time dependent, but they are a function of local concentration and overpotential distributions around individual nuclei. In order to better understand the qualitative nature of the distribution, it was therefore decided to employ a simple stochastic simulation of growing discs on a surface, the principles of which are described below.

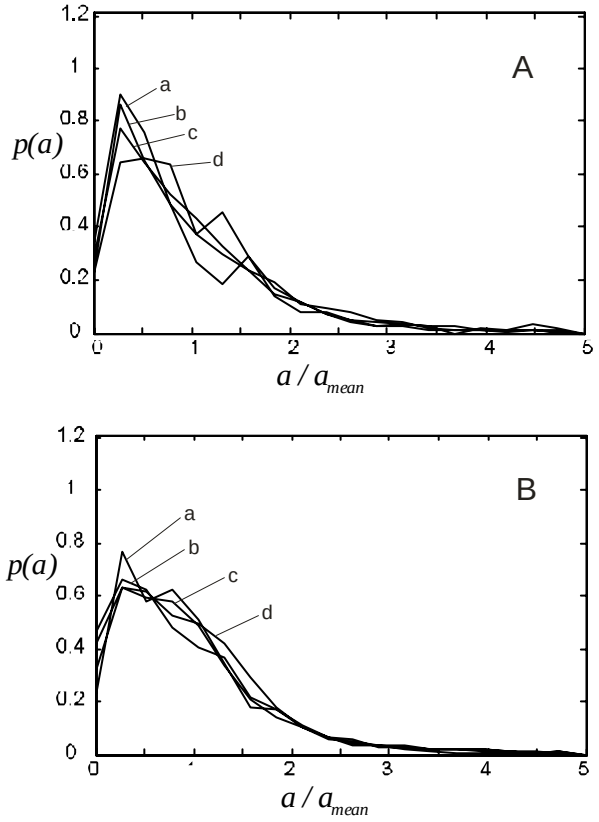

Figure 6.7: Histograms showing nucleus area distributions reduced with respect to the mean area for that dataset (shown as lines for clarity). A) Deposition from A) a 250µM $AgNO_3$ and B) a 500µM solution until a current maximum was achieved (see text). In both cases, deposition was performed at a) -0.5V, b) -0.1V, c) -0.15V, and d) -0.2V. p(a) is the probability of a specific nucleus having area a and a_{mean} is the mean area for that dataset.

The simulation was carried out in a region of size 1 x 1, with periodic boundary conditions in both directions. The simulation region was given a maximum number of active sites on which nuclei could appear, N_0. Nuclei were defined by a position, an age (u) and a radius (r). At each timestep (of size 1) the ages and radii of all the

existing nuclei were updated. The expression for the radius of an isolated hemispherical cluster growing as a result of a reaction in which the exchange current density is sufficiently large is:[17, 25]

$$r(u) = \left[2Dc_0 \left(\frac{M}{\rho} \right) \left\{ 1 - \exp\left(-z \frac{F\eta}{RT} \right) \right\} u \right]^{\frac{1}{2}} \tag{6.6}$$

The overpotentials considered in this chapter are sufficiently large that the term in braces in the above equation may be approximated by 1, implying pure diffusion control. To simulate the effect of nearby clusters depleting the concentration around the particular nucleus under consideration, c_0 (the bulk concentration) was replaced in this case by c_i, a concentration due to the depleting effect of the nearest neighbour. Clearly for a given set of conditions, every term in equation (6.6) is a constant except c_i and u. The expression used for the purposes of simulation was therefore:

$$r_{u+1} = r_u + G\sqrt{c_i} \left[(u+1)^{\frac{1}{2}} - u^{\frac{1}{2}} \right] \tag{6.7}$$

where G is a parameter representing the rate of uninhibited growth of the nucleus, given by (from equation (6.6))

$$G = \left[2D \left(\frac{M}{\rho} \right) \right]^{\frac{1}{2}} \tag{6.8}$$

Assuming a stationary concentration distribution, a full expression for c_i is:[17, 25]

$$c_i(d) = c_0 \left[1 - \frac{r_i}{d} \left(1 - \frac{c_s}{c_0} \right) \right] \tag{6.9}$$

in which d is the centre to centre distance between the inhibiting and growing nuclei, r_i is the radius of the inhibiting nucleus, and c_s is the concentration at the surface of the growing cluster. Note that equation (6.9) is a limiting expression, valid for small

nuclei and long times, used as an approximation to the exact result for simplicity. Assuming equation (6.6) is valid,

$$\frac{c_s}{c_0} = \exp\left[-z\frac{F\eta}{RT}\right] \tag{6.10}$$

Again, the overpotentials used in this chapter are such that we can use the approximation $c_s/c_0 = 0$, implying total depletion of the depositing ion at the surface of the hemisphere. Every term in equation (6.9) is therefore constant except r_i and d, so for the purposes of simulation, the following was used:

$$c_i(d) = c_0\left[1-\frac{r_i}{d}\right] \tag{6.11}$$

In addition, at each timestep a 'potential' new nucleus was generated at a random position on the surface (where 'potential' means the new nucleus could either be accepted as a growing nucleus or rejected by the tests described below). In reality, there are two processes retarding the rate of nucleation as time progresses: filling of active sites, and inhibition zones forming around established nuclei due to decreased concentration (and local overpotential). To represent these, two tests were performed before the potential nucleus was accepted. First, to represent the effect of filling of active sites, a random number between 0 and 1 was generated, and compared to the formula[26]

$$P = \frac{N_0 - N}{N_0} \tag{6.12}$$

in which P is the probability of the active site under consideration being unoccupied (i.e. not already nucleated) and N is the number of currently occupied active sites. If the random number was less than P, the site upon which the new nucleus had appeared was considered unoccupied; otherwise, the potential nucleus was

immediately rejected. Second, the nearest neighbour to this potential nucleus was found, and the size of an 'exclusion zone' around the neighbour determined. If the potential nucleus was outside the exclusion zone, it was accepted as a new nucleus, having $r = 0$ and $u = 0$. An exclusion zone is a discrete approximation to the continuous distribution of nucleation rate around a growing nucleus, a circular area inside of which no nucleation can occur, and outside of which nucleation occurs at the initial rate, A_0. The radius of this exclusion zone, d_c, is set to be the distance at which some selected proportion of the full nucleation rate is achieved. The full expression for the local nucleation rate at a distance d from a cluster is:[17, 25]

$$\frac{A}{A_0} = \left[1 - \left(\frac{2Dc_0M}{\rho} \right)^{\frac{1}{2}} \left(1 - \exp\left[-z\frac{F\eta}{RT} \right] \right)^{\frac{3}{2}} \frac{u_i^{\frac{1}{2}}}{d} \right]^{n_k+1} \tag{6.13}$$

If A/A_0 is replaced by a threshold proportion, A_c, then $d = d_c$. Substitution of d_c from equation (6.13) and r from equation (6.6) into equation (6.9) expresses A_c in terms of an equivalent critical concentration:

$$c_c = c_0 A_c^{\frac{1}{n_k+1}} \tag{6.14}$$

Thus, by rearranging equation (6.11), we find the following expression for d_c in terms of the inhibiting nucleus radius:

$$d_c = \frac{r_i}{1 - A_c^{\frac{1}{n_k+1}}} \tag{6.15}$$

Note that at the start of the simulation, no active sites are filled and there are no inhibiting nuclei, so the initial nucleation rate is 1. This process of generating new potential nuclei and updating their ages and radii is then repeated for as long as required.

Some comments on this model follow: The principles upon which the model is based draw from ideas by Tsakova et al.[26] and Scharifker et al.[24] Scharifker's earlier system implicitly used an infinite number of active sites – the rate of nucleation could only be retarded by inhibition by other nuclei. Exclusion zones were used to determine the extent of this inhibition, with the zone radius dependent only on the age of the inhibiting nucleus; nucleus radii were not calculated. Tsakova's model used the same treatment of active sites as that described above. Nucleus radii were computed at each timestep, but were used only to calculate inhibition of new nuclei, and each was computed independently. A continuous probability distribution was used rather than exclusion zones. Using an exclusion zone is clearly less physically correct than Tsakova's continuous distribution.[17, 25] However, methods based on exclusion zones have been shown to generate results in good agreement with experimental NNDs in the case of lead deposited on glassy carbon.[19, 20]

When determining whether a new nucleus should be generated, the exclusion zone of only the nearest neighbour was considered. In reality, the effects of several neighbours (or, in the limit, every other nucleus) might be considered. This was attempted by Milchev et al.,[25] who considered the effect of all other nuclei, Kruijt et al.,[17] who considered the effects of 2, 3, 4 or 5 nearest neighbours, and García-Pastoriza et al.,[18] who considered the effect of only 'natural neighbours'. However, in each case it was found that considering the effects of only a single most influential neighbour produced a better agreement with experiment. Again, presumably the effects of all other nuclei should be considered when calculating the effects of inhibition on nucleus radii. In practice, only the nearest neighbour was considered for simplicity.

Clearly, the model of growth used here is crude in the sense that two dimensional concentration distributions are being used to modify the growth rate of three dimensional nuclei, having finite radii; equations (6.7) and (6.9) can only be exactly applied in the case when the growing nucleus has a radius (and hence height) of zero. In all simulations, G was fixed such that the mean nearest neighbour distance was always greater than the mean nucleus radius. As figure 6.1 shows, this corresponds qualitatively with the experimental observations, and ensured the generation of artefacts caused by overlapping nuclei was minimized.

There are two independent ways in which a 'potential' nucleus can be rejected: the 'active site' being already occupied, and the active site being in a nucleation exclusion zone of another nucleus. In practice when running the simulation we find two limiting cases. When the number of active sites is large (in the sense that the mean distance between them is small compared to the size of the growing nucleus exclusion zones), every nucleation failure results from the chosen active site being inside an exclusion zone. When the number of active sites is very low, most failures result from lack of empty active sites. Between these two limits, as the number of active sites increases there is a corresponding shift from mostly nucleation failures to mostly inhibition failures.

Simulations were run until a new nucleus failed to be generated for 10 successive timesteps, indicating that the rate of successful nucleation was just starting to slow – this position on the N vs. time graph corresponds roughly with that at which the electrochemical experiments were stopped, allowing a comparison to be made. The

number of nuclei generated before this point in any specific simulation depended on the values of A_c and n_k chosen, but for averaging purposes each simulation was repeated until a minimum of 10000 nuclei in total had been generated.

Initially, n_k was set to 0, and N_0 set to 1 x 10^{10} (an effectively 'infinite' number of active sites in the sense that all nucleation failures were due to inhibition rather than lack of active sites). Simulations were run with values of A_c varying from 5% of c_0 to 95% of c_0, with the results shown in figure 6.8A. Note that to allow meaningful comparisons with the experimental data, all datasets are plotted in units reduced with respect to the mean area of that dataset. A clear pattern is visible – at small values of A_c, we see a large proportion of nuclei having a relative size close to 0, with a steady decrease in number until $a/a_{mean} \approx 3.5$. At large values of A_c, a broader peak is observed with a maximum at about 1.5, and a decrease to zero at approx $a/a_{mean} \approx 2$. In between these two limits, characteristics of both limiting cases are visible.

Next, the effect of varying n_k between 0 and 3 was investigated for various values of A_c. The results for $A_c=0.1c_0$ are plotted in figure 6.8B. As might be expected from equation (6.15), we find that increasing n_k has the same effect as increasing A_c, broadening the peak and skewing it towards $a/a_{mean} \approx 1.5$.

Finally, the number of active sites was decreased by factors of 100 for $n_k=0$ and various values of A_c. Figure 6.8C shows the results for $A_c=0.1c_0$ between $N_0 = 100$ and $N_0 = 1x10^{10}$. We can see that decreasing the number of active sites has the same effect as increasing A_c, again broadening the peak and moving its centre to approximately $a/a_{mean} \approx 1.5$. At large values of A_c, decreasing the number of active

sites has no effect on the distribution; it appears that the distribution in figure 6.8A(c) and 8C(a) is the limiting shape for large A_c, large n_k, and small N_0.

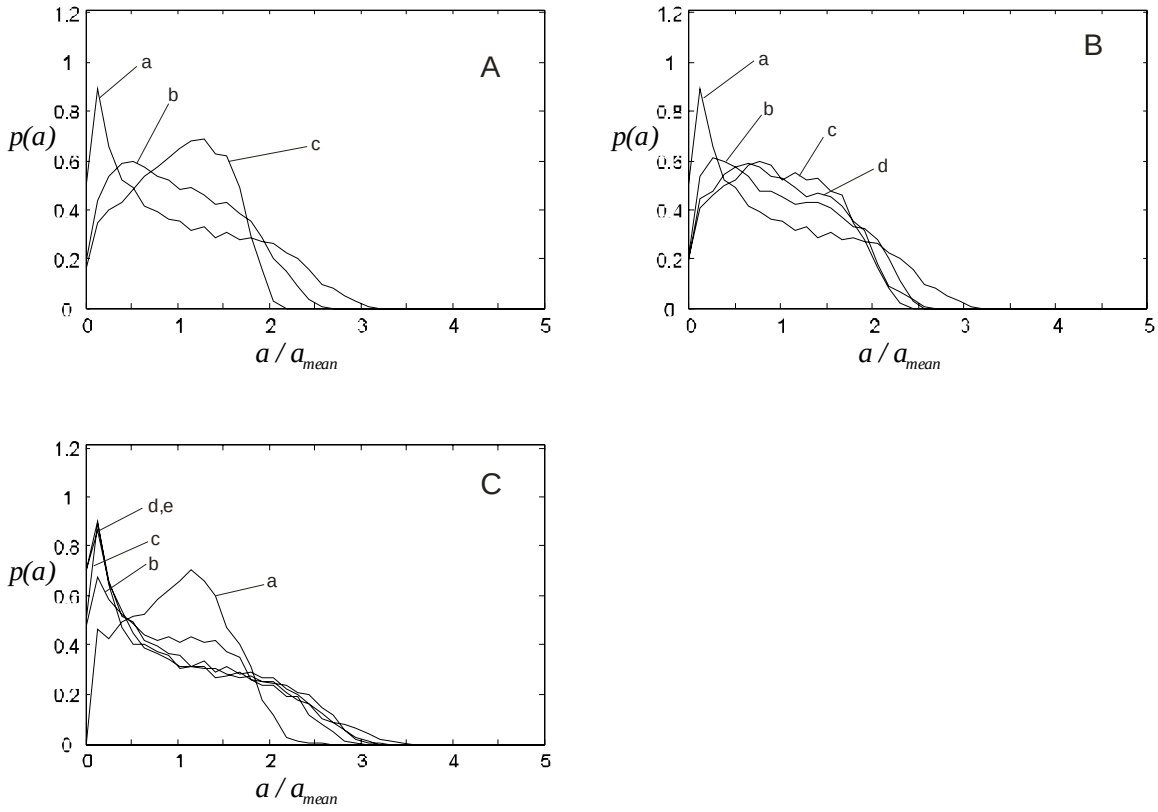

Figure 6.8: Simulated area distributions showing the effect of varying the parameters A_c, n_k, and N_0 (see text for further details on simulation conditions). A) $N_0 = 10^{10}$, $n_k = 0$, a) $A_c = 0.1\ c_0$, b) $A_c = 0.5\ c_0$, c) $A_c = 0.9\ c_0$. B) $N_0 = 10^{10}$, $A_c = 0.1\ c_0$, a) $n_k = 0$, b) $n_k = 1$, c) $n_k = 2$, d) $n_k = 3$. C) $n_k = 0$, $A_c = 0.1\ c_0$, a) $N_0 = 10^2$, b) $N_0 = 10^4$, c) $N_0 = 10^6$, d) $N_0 = 10^8$, e) $N_0 = 10^{10}$. Note that in cases d and e, essentially all nucleation failures are due to inhibition, so the distributions are very similar.

Comparison of figures 6.7 and 6.8 show that the simulations generate histograms with similar features to those observed in the experimental data. Assuming that the critical nucleus size is small,[17] the experimental data for 50mV matches the simulations at low A_c and large N_0 quite well. As the potential increases towards 200mV, the experimental distributions broaden and move to larger a/a_{mean}, in a manner similar to that observed for the simulated distributions on increasing A_c (or increasing n_k, or decreasing N_0). The simulation does not provide enough information to isolate the

cause of the distribution change in the experimental data; however, the larger nucleus densities observed at higher overpotentials suggest that nucleation failures due to lack of active sites may become more important (equivalent to reducing N_0 in the simulation).

As well as area information, the simulation described above generated data on the nearest neighbour distributions of the nuclei at the point when simulation stopped. In order to further investigate the validity of the model on which it was based, simulations were next run until a new nucleus failed to be generated for 100 successive timesteps, corresponding to almost complete saturation of the active sites (or almost total inhibition), followed by some growth. This allowed comparison of the simulated nearest neighbour distances with the experimental data shown in figure 6.6.

It was observed that when plotted in reduced units, the shape of the distributions again had two limits; at values of $N_0 > 1x10^6$ and $0.05\ c_0 < A_c < 0.95\ c_0$, the nearest neighbour distribution showed a sharp peak at a value of $\sqrt{2\pi\nu}r = 1.5$, which was independent of A_c (and n_k). With $N_0 < 1x10^3$, the distribution followed a Poisson distribution, again independent of A_c. In between these two N_0 limits, intermediate distributions were found, with large A_c favouring the former case, and small A_c the latter. This is illustrated in figure 6.9, along with comparisons to some experimental data. We find that the data for 500μM is a good match for the large N_0 simulated result, an observation consistent with the analysis of nucleus areas above. However, at 250μM, the experimental distribution is closer to a Poisson distribution. Comparison with the simulation suggests that a reduced number of active sites at

lower concentration is responsible, although the nucleus area data provides no evidence for this.

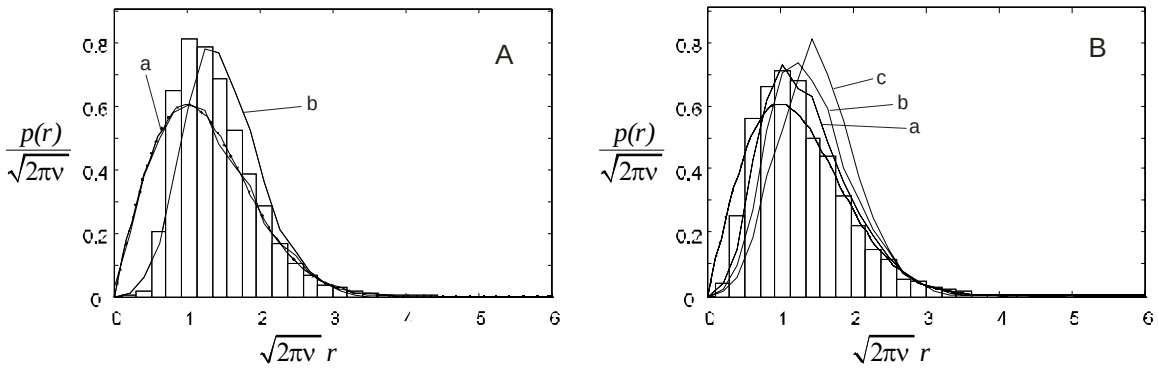

Figure 6.9: Comparison of experimental and simulated reduced nearest neighbour distributions. A) Bars show data for nuclei deposited on BDD from a 500µM solution of $AgNO_3$ at -0.2V for 60s. Simulations: $A_c = 0.1\ c_0$, $n_k = 0$, line a) $N_0 = 10^2$, b) $N_0 = 10^{10}$. B) Bars show data for nuclei deposited from a 250µM solution of $AgNO_3$ at -0.2V for 60s. Simulations: $N_0 = 10^4$, $n_k = 0$, line a) $A_c = 0.05\ c_0$, a) $A_c = 0.5\ c_0$, a) $A_c = 0.95\ c_0$. In both cases, the dotted line shows a reduced Poisson distribution.

6.7 Conclusions

The deposition of silver on boron-doped diamond has been studied using standard voltammetric techniques and also optical microscopy. It has been demonstrated voltammetrically that, as expected from similar studies on carbon electrodes, the deposition proceeds via nucleation and diffusion controlled growth. The saturation nucleus number densities were recorded, and compared with those derived from voltammetric analysis, and analysis of the initial gradient of the N vs. t curves. As expected, both of these methods significantly underestimated the value of N_{sat}, implying that inhibition of active sites by diffusion zones around growing nuclei is an important factor at all times during the deposition. It was also found that the potentiostatic transients recorded were rather variable; this inconsistency was shown to be the result of the manner in which the electrode had been polished in between measurements, and no such effect was found when scans were repeated without

removal from solution. On the other hand, electrochemical stripping was found by microscopy to be insufficient to remove all observable deposits from the electrode surface.

The influence of concentration and potential was investigated by using optical microscopy to determine the mean nearest neighbour distance as a function of time, and also by plotting the first through fifth nearest neighbour distributions after deposition for 60s. Under all conditions, the mean nearest neighbour distance was found to be larger than that predicted by a Poisson distribution having the same number density, indicating the presence of zones around established nuclei inhibiting the appearance of new nuclei. The effect of these zones was shown to extend only to approximately the second nearest neighbour; further neighbours had distributions very similar to Poisson distributions.

The distribution of nucleus areas was also studied after deposition for a given amount of time. A simple model based on appearance and inhibited growth of nuclei was shown to give nucleus area distributions in good qualitative agreement with the experimental data. Nearest neighbour information from the simulations were also shown to agree qualitatively with experimental nearest neighbour distributions. Although too simplistic to generate any quantitative insights into the nucleation and growth processes of silver on BDD, the qualitative agreement between simulation and experiment suggests that the foundations of the model used are essentially correct, and that further work in this area may be fruitful.

6.8 References

[1] R. G. Compton, J. S. Foord, F. Marken, *Electroanalysis* **2003**, *15*, 1349.
[2] M. E. Hyde, R. Jacobs, R. G. Compton, *J. Phys. Chem. B.* **2002**, *106*, 11075.
[3] O. Enea, B. Riedo, G. Dietler, *Nano Letters* **2001**, *2*, 214.
[4] N. Vinokur, B. Miller, Y. Avyigal, R. Kalish, *J. Electrochem. Soc.* **1999**, *146*, 125.
[5] J. Zak, M. Kolodziej-Sadlok, *Electrochim. Acta* **2000**, *45*, 2803.
[6] M. Palomar-Padarvé, M. T. Ramírez, I. González, A. Serruya, B. Scharifker, *J. Electrochem. Soc.* **1996**, *143*, 1551.
[7] M. Miranda-Hernández, *J. Electroanal. Chem.* **1998**, *443*, 81.
[8] D. J. Astley, J. A. Harrison, H. R. Thirsk, *Trans. Faraday Soc.* **1967**, *64*, 192.
[9] M. Miranda-Hernández, I. González, N. Batina, *J. Phys. Chem. B* **2001**, *105*, 4214.
[10] J. Golas, J. Osteryoung, *Anal. Chim. Acta* **1987**, *192*, 225.
[11] J. P. Sousa, S. Pons, M. Fleischmann, *J. Chem Soc. Faraday Trans.* **1994**, *90*, 1923.
[12] B. W. Mao, L. H. Xiong, X. W. Cai, *J. Electroanal. Chem.* **1996**, *416*, 145.
[13] A. Milchev, E. Vassileva, V. Kertov, *J. Electroanal. Chem.* **1980**, *107*, 323.
[14] A. Milchev, E. Vassileva, *J. Electroanal. Chem.* **1980**, *107*, 337.
[15] G. A. Gunawardena, G. Hills, I. Montenegro, *J. Electroanal. Chem.* **1982**, *138*, 241.
[16] A. Milchev, *J. Electroanal. Chem.* **1998**, *457*, 35.
[17] W. S. Kruijt, M. Sluyters-Rehbach, J. H. Sluyters, A. Milchev, *J. Electroanal. Chem.* **1994**, *371*, 13.
[18] E. García-Pastoriza, J. Mostany, B. Scharifker, *J. Electroanal. Chem.* **1997**, *441*, 13.
[19] A. Serruya, J. Mostany, B. R. Scharifker, *J. Chem. Soc., Faraday Trans.* **1993**, *89*, 255.
[20] J. Mostany, A. Serruya, B. R. Scharifker, *J. Electroanal. Chem.* **1995**, *383*, 37.
[21] W. Plieth, H. Dietz, G. Sandmann, A. Meixner, M. Weber, P. Moyer, J. Schmidt, *Electrochim. Acta* **1999**, *44*, 3659.
[22] R. M. Stiger, S. Gorer, B. Craft, R. M. Penner, *Langmuir* **1999**, *15*, 790.
[23] H. Liu, R. M. Penner, *J. Phys. Chem. B* **2000**, *104*, 9131.
[24] B. Scharifker, J. Mostany, A. Serruya, *Electrochim. Acta* **1992**, *37*, 2503.
[25] A. Milchev, W. S. Kruijt, M. Sluyters-Rehbach, J. H. Sluyters, *J. Electroanal. Chem.* **1993**, *362*, 21.
[26] V. Tsakova, A. Milchev, *J. Electroanal. Chem.* **1998**, *451*, 211.
[27] D. Kashchiev, *Nucleation: Basic Theory with Applications*, Butterworth Heinemann, Oxford, **2000**.
[28] A. Milchev, *Contemp. Phys.* **1991**, *32*, 321.
[29] A. Milchev, *Electrochim. Acta* **1986**, *31*, 977.
[30] A. Milchev, *Electrochim. Acta* **1985**, *30*, 125.
[31] G. A. Gunawardena, G. Hills, I. Montenegro, B. Scharifker, *J. Electroanal. Chem.* **1982**, *138*, 225.
[32] H. S. Harned, C. L. Hildreth, *Chem. Rev.* **1947**, *40*, 3292.
[33] M. Sluyters-Rehbach, J. H. O. J. Wijenberg, E. Bosco, J. H. Sluyters, *J. Electroanal. Chem.* **1987**, *236*, 1.
[34] M. V. Mirkin, A. P. Nilov, *J. Electroanal. Chem.* **1990**, *283*, 35.
[35] L. Heerman, A. Tarallo, *J. Electroanal. Chem.* **1999**, *470*, 70.

[36] L. Heerman, A. Tarallo, *Electrochem. Comm.* **2000**, *2*, 85.
[37] B. Scharifker, G. Hills, *Electrochim. Acta* **1983**, *28*, 879.
[38] B. Scharifker, J. Mostany, *J. Electroanal. Chem.* **1984**, *177*, 13.

7 Theoretical and Experimental aspects of Electrodeposition under Hydrodynamic Conditions

7.1 Introduction

The electrodeposition of metals, described by a process of nucleation followed by diffusion limited three dimensional growth, is an area of considerable interest. Modelling of deposition potentiostatic current transients is an informative method of analysis, potentially revealing parameters such as the nucleation rate, saturation nucleus density, and number of active sites. There are presently several competing models, in particular those of Scharifker and Mostany,[1] Sluyters-Rehbach, Wijenberg, Bosco and Sluyters,[2] and Mirkin and Nilov,[3] based on slightly differing assumptions. One common feature of all these models is that they use Cottrellian diffusion to describe the total flux to the electrode surface, an assumption that is only valid under quiescent conditions. Under hydrodynamic conditions, these models are therefore inapplicable. At present, little attention has been paid to the theoretical treatment of this area. However, we have recently derived a model describing the potentiostatic current response to deposition under conditions of forced convection.[4] This chapter extends this previous work, and demonstrates the applicability of the model to the nucleation and growth of lead under two sets of hydrodynamic conditions. In the first, a propeller is used to direct solution flow over the electrode surface, and in the second a wall tube electrode is used.

7.2 Theory

We have shown[4] that given a constant diffusion layer thickness, the potentiostatic current response of a three-dimensional nucleation and growth process can be expressed by:

$$J = zFc\frac{D}{\delta}\left[1-\exp\left\{-B\sqrt{t}\left(1-e^{-At}\sum_{n=0}^{\infty}\frac{(At)^n}{n!(2n+1)}\right)\right\}\right] \qquad (7.1)$$

in which

$$B = 2\sqrt{2}\pi\left(\frac{Mc}{\rho}\right)^{\frac{1}{2}} D^{\frac{1}{2}}\delta N_0 \qquad (7.2)$$

The meanings of all symbols are given in appendix 1. For the purposes of data fitting and parameter optimization, it is convenient to approximate equation (7.1) by:

$$J = zFc\frac{D}{\delta}\left[1-\exp\left(-Bt^{\frac{1}{2}}\left\{1-e^{-At}\left[1+\frac{At}{3}+\frac{(At)^2}{10}+\frac{(At)^3}{42}+...\right]\right\}\right)\right]+j_0 \qquad (7.3)$$

where terms above t^3 are assumed to be negligible, and A, B and j_0 are parameters to be optimized (this expression is derived more fully in appendix 3). Note that an induction time, t_0 could have been included as with the corresponding expression under silent conditions (equation (7.6)), but was found to be unnecessary in the present experiments. This result implies that the current response is a monotonic rising function, with the limiting current (for a given species) dependent only on the diffusion layer thickness, i.e. the strength of the external agitation. Plots showing the effect of some values of A and B on J are shown in figure 7.1. Clearly, for a constant value of A, larger values of B increase the rate of current increase, and decrease the time until current saturation. As $B \to \infty$ the time until current saturation tends to zero. However, as $A \to \infty$ the bracketed term in equation (7.1) tends to 1, and the curve shape becomes dependent only on B. This reveals a possible weakness in using

equation (7.3) to extract values of A and B: although optimization should be effective for relatively small values of A and/or B, it may be impossible to determine the value of A when A is large. This is discussed further below.

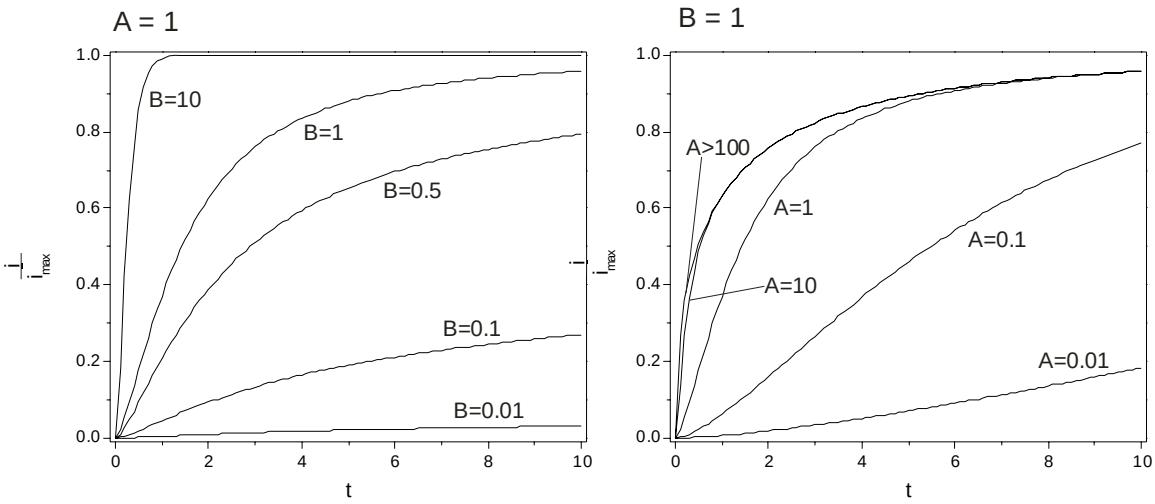

Figure 7.1: Plots of equation (7.3) for a) A=1 with various values of B and b) B = 1 with various values of A. See text for the significance of these parameters.

7.3 Experimental Details

Aqueous lead solutions were made using: lead (II) nitrate (BDH AnalaR, 99.5%+), and potassium nitrate (Aldrich, 99%+). Ferrocyanide solutions were made using potassium hexacyanoferrate(II) (BDH AnalaR, 99%+). All solutions were thoroughly degassed using argon between experiments. All experiments were performed on the glassy carbon electrode described in chapter 2.

The electrochemical cells used and all relevant dimensions are illustrated in figure 7.2; the stirred cell, A, had a total volume of approximately 800mL, while the wall tube cell, B, had a volume of approximately 500mL. In the stirred cell, hydrodynamic conditions were generated using a Gallenkamp model SS420 stirrer with propeller attachment, which allowed continuous variation in propeller rotation speed between 0

and 600 rpm. The propeller was shaped and positioned such that solution flow was directly towards the electrode surface. The flow cell used an elevated reservoir with a control tube of variable width allowing flow rates between 3.9 and 19.3 mLs^{-1}. Quiescent experiments were performed in the stirred cell with the rotation rate set to zero. Experiments were performed at 298K ± 5K.

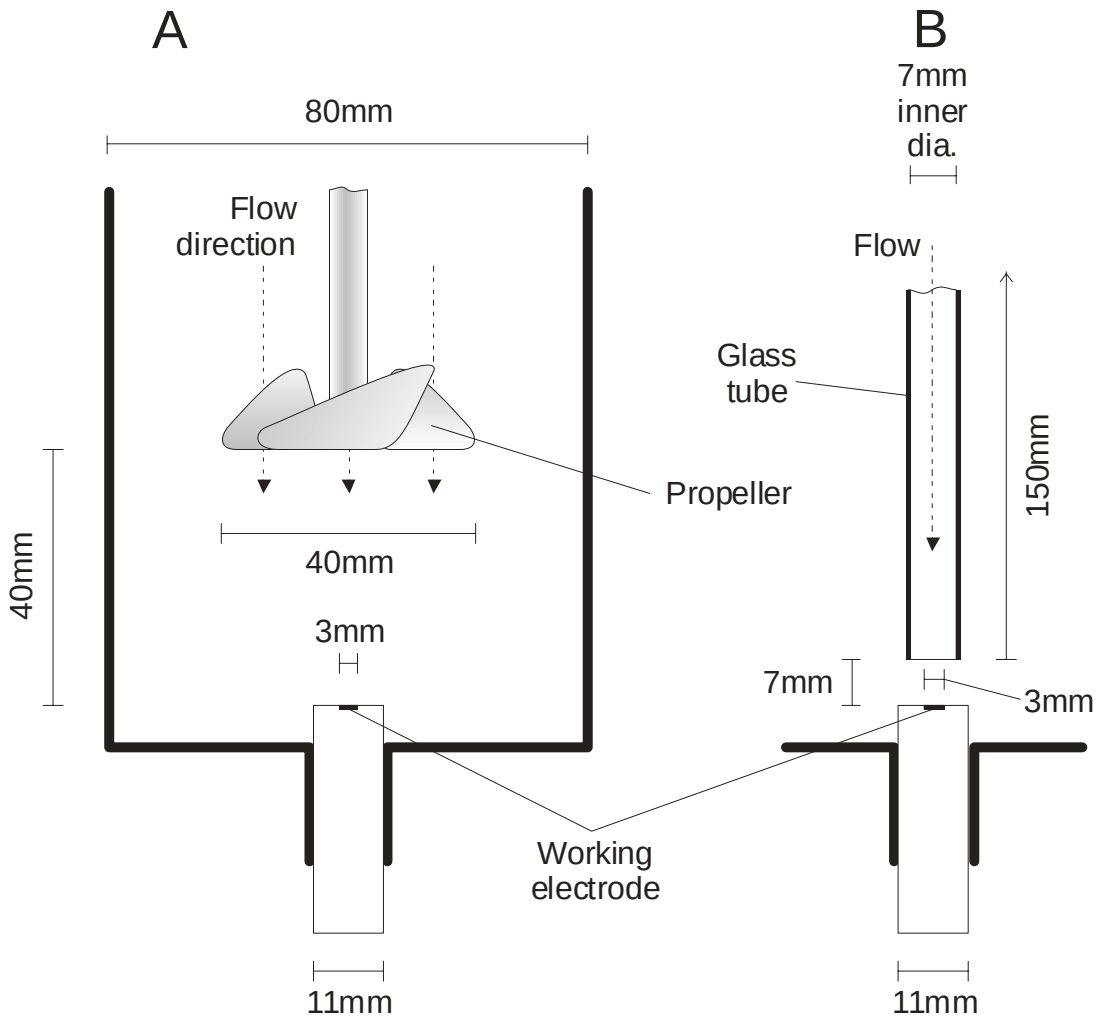

Figure 7.2: Cross section diagrams showing the configurations of a) the stirred cell and b) the flow cell used, as well as all relevant dimensions.

7.4 Cell Calibration

Experiments designed to produce diffusion layer thicknesses between approx. 20 and 40μm were performed in the propeller cell. Electrochemical cells using stirring to agitate the solution are rarely employed for analytical work owing to the relative difficulty in rigorously modelling solution flow to the electrode compared to, for example, rotating disk electrodes (RDEs). In addition, RDEs give larger currents; however such cells are widely employed in practical metal plating. Another issue is the uniformity of the flow generated; it may be difficult to ensure that the electrode is uniformly accessible in the sense that the flux of electroactive species is the same to all parts of the electrode. On the other hand, it has been demonstrated that a carefully constructed stirred cell using a propeller can provide well defined mass transport to the electrode.[5] It was therefore important to ensure that the electrode was uniformly accessible in the configuration illustrated in figure 7.2A; to this end the following experiments were performed.

Part of the electrode was covered using thin adhesive tape, and the exposed electrode area determined microscopically. Using this partially covered electrode, a solution containing 1mM ferrocyanide and 1M potassium nitrate was oxidized at +500mV and the limiting current recorded. This procedure was repeated for various electrode exposed areas (see figure 7.3) and at various propeller rotation rates. The results are plotted in figure 7.3A: we find that the limiting current is approximately proportional to the electrode area at the intermediate five stirring rates. At the lowest rate there is little increase, presumably as the jet does not reach the electrode surface. At the two highest rotation rates, localized hydrodynamic cavitation occurred and there are also

significant deviations from linearity. The intermediate stirring rates were therefore used in all the following experiments.

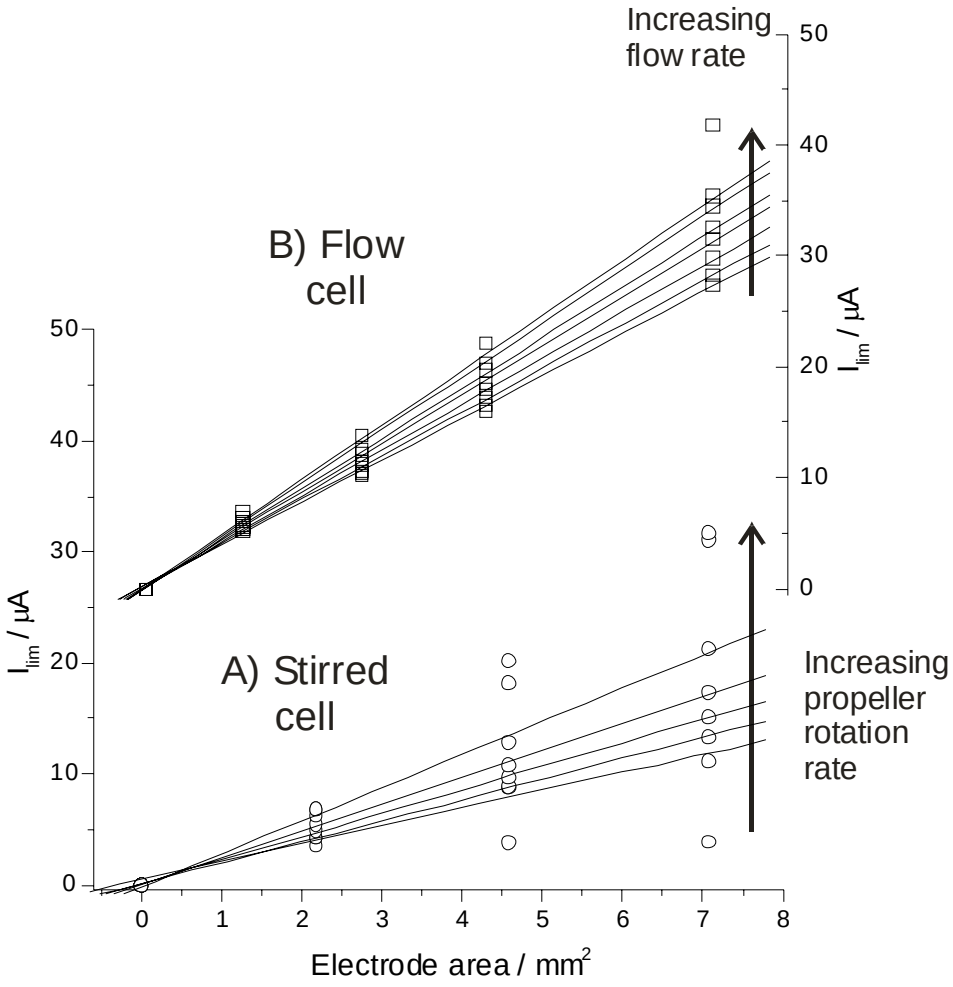

Figure 7.3: Plots of the limiting current for ferrocyanide oxidation at +500mV vs. working electrode surface area. A) Stirred cell data (left axis, circles). Increasing limiting currents correspond to arbitrary increases in the propeller rotation rate. B) Flow cell data (right axis, squares). From bottom to top the lines correspond to flow rates of 3.9, 4.9, 6.9, 8.3, 9.7, 12.2, 14.4 and 19.3 mLs^{-1}.

In contrast, the behaviours of wall-tube and wall-jet flow cells are well understood.[6-11] The configuration used in the experiments described below is a wall-tube electrode: the electrode radius is less than the nozzle diameter. In fact the electrode is less than half the nozzle diameter, and it has been shown[6] that with this configuration the electrode is uniformly accessible under conditions of both laminar and turbulent

flow. This is confirmed by experiments similar to those described above: figure 7.3B shows that the limiting ferrocyanide oxidation current varies approximately linearly with electrode exposed area. The data illustrated show flow rates between 3.9 and 19.3 mLs^{-1}. The Reynolds number is given by:

$$Re = \frac{d.\bar{u}}{\nu} \tag{7.4}$$

in which the meaning of each symbol is defined in appendix 1; the flow rates above correspond to Reynolds numbers of between 3900 and 96400. Turbulence occurs at Reynolds numbers of approximately 4000 and above,[6] indicating that all the flow rates (except possibly the lowest) were within the turbulent regime.

Having confirmed the uniform accessibility of the electrode in both cells, the next step is to quantify the effect of the electrolyte flow by calculating the diffusion layer thickness under each set of conditions. The following equation is used:[12]

$$J_{lim} = zFc\frac{D}{\delta} \tag{7.5}$$

in which the meaning of each symbol is defined in appendix 1. Using the ferricyanide data from the completely exposed electrode, values of δ under each set of conditions were computed. The expected limiting currents for Pb were then calculated by substitution of the appropriate parameters in equation (7.5). The values of D used for ferrocyanide and Pb^{2+} were 6.32 x 10^{-6} cm^2s^{-1} and 9.0 x 10^{-6} cm^2s^{-1} respectively at 298K.[13] These expected limiting currents for Pb are plotted as a function of diffusion layer thickness in figure 7.4.

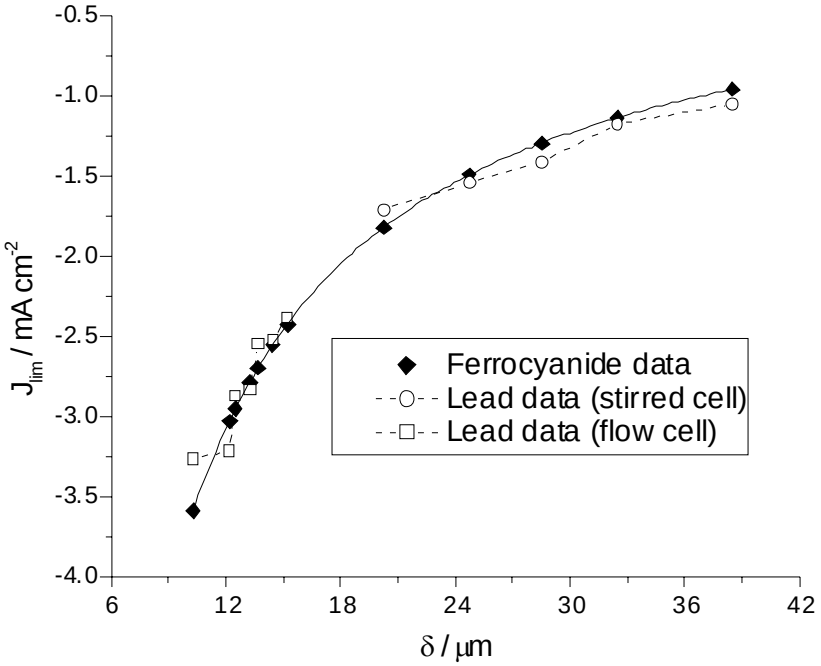

Figure 7.4: Plot of the limiting currents for Pb^{2+} vs. the diffusion layer thickness. The expected values for Pb^{2+} computed from the values of δ derived from the ferrocyanide data in figure 7.3 are shown as a solid line (see text). Observed values are plotted as open circles (stirred cell) and open diamonds (flow cell).

7.5 Lead Deposition

Equation (7.1) indicates that the limiting current for the lead deposition should be the same as that given by equation (7.5). In order to test this, lead was deposited from a solution containing 2.1mM $Pb(NO_3)_2$ and 1M KNO_3 under conditions corresponding to each diffusion layer thickness in figure 7.4. A suitable deposition potential was determined by performing cyclic voltammetry under quiescent conditions to estimate the crossover potential for the system, then using an overpotential of 60mV for 10s. In every case, the current stabilized within approximately 2 seconds, and the limits determined from these data are shown in figure 7.4. We find that there is good agreement with the values computed from the ferrocyanide data.

Next, similar depositions were performed at a variety of lower overpotentials under each set of flow conditions: between 3 and 38 mV in the case of the stirred cell, and between 5 and 30 mV in the case of the flow cell. In each case, ten datasets were collected and analyzed. Typical examples of the transients obtained are shown as open circles in figure 7.5.

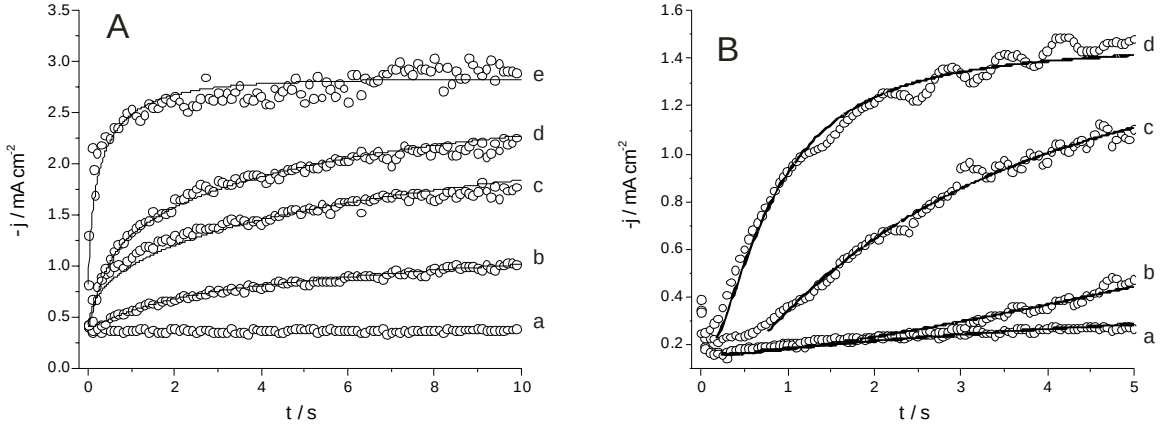

Figure 7.5: Typical transients recorded for the nucleation of Pb^{2+}. A) Flow cell data with δ=13.2μm: η= a) -10mV, b) -15mV, c) -20mV, d) -25mV, e) -30mV. B) Stirred cell data with δ=28.5μm: η= a) -8mV, b) -18mV, c) -28mV, d) -38mV. Open circles show experimental data; solid lines show optimized fits to equation (7.3).

These transients were then fitted to equation (7.3) using the 'non-linear curve fitting' feature of Microcal Origin (illustrated as solid lines in figure 7.5). Excellent fits to the experimental data could be achieved with certain exceptions: in figure 7.5A dataset (a), for example, we find that the applied overpotential is not large enough to encourage nucleation and growth (at least on the timescale of the experiment); meaningful values of the parameters A and B could therefore not be determined. The same effect was observed at low overpotentials in the stirred cell; this data is not illustrated in figure 7.5B for clarity. Another problem occurred when employing large overpotentials. As discussed in the theory section above, equation (7.1) tends to indistinguishable curves at large values of A. It was therefore impossible to determine the exact value of A in cases such as figure 7.5A, dataset (e). However, we

may conclude that the rate of nucleation was 'fast' compared to those experiments performed at lower overpotentials.

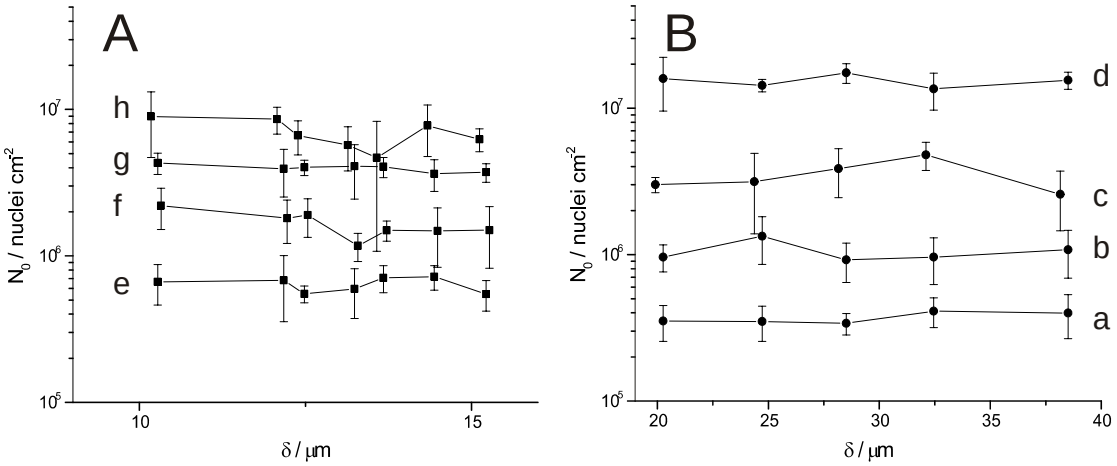

Figure 7.6: Plots of N_0 as a function of diffusion layer thickness computed from optimized fits such as those illustrated in figure 7.5. In each case, the values of N_0 derived from ten datasets were averaged; error bars show ± 1 standard deviation. Circles (B) show stirred cell data: η= a) -8mV, b) -18mV, c) -28mV, d) -38mV. Squares (A) show flow cell data: η= e) -15mV, f) -20mV, g) -25mV h) -30mV. Note that some points have been staggered to clarify the position of the error bars.

Figure 7.6 shows the values of N_0 determined from the optimized values of B (see equation (7.2)) as a function of diffusion layer thickness at the studied overpotentials. At each data point, the ten optimized values of B have been averaged; note that the error bars reflect only the standard deviation in the optimized values of B, not any underlying uncertainty in the values of B. Several features are apparent: there is no dependence of N_0 on diffusion layer thickness. This is as might be expected; the number of active sites is a property of the electrode surface and should therefore be independent of the hydrodynamic conditions in the solution. Figure 7.7 shows the mean of all N_0 values at each δ plotted against the applied overpotential. We find that increasing the overpotential results in an approximately exponential increase in N_0. This is consistent with previous measurements under sonicated conditions.[4] Such a dependence is well established under quiescent conditions and is the result of the distribution of the deposit-substrate surface energy over the electrode surface.[14, 15]

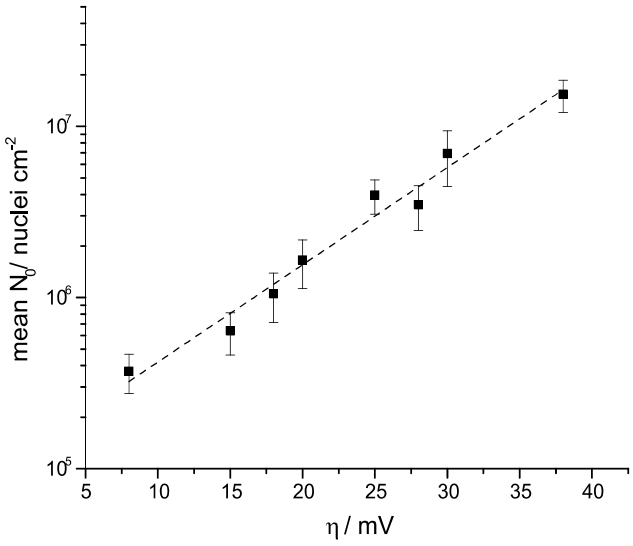

Figure 7.7: Plot of the mean of N_0 over all values of δ vs. overpotential. Error bars show ±1 standard deviation. The dotted line shows an optimized exponential fit to the data.

Figure 7.8 shows the values of A determined from the optimized values of A as a function of diffusion layer thickness and overpotential. In this case the same procedure as above was used: the ten values of A at each set of conditions were averaged. However, no error bars are shown for clarity. We find that A is approximately exponentially dependent on overpotential. This is in agreement with the observations under sonicated conditions.[4] δ also appears to affect A: at larger values of δ (figure 7.8B) there is no dependence within the error of the measurements, while there is a significant step to the smaller values of δ (figure 7.8A), then a further general increase within this dataset. This probably reflects a break down of the diffusion layer model; clearly reducing the 3-dimensional problem of hydrodynamic flow to the electrode surface to a single parameter is an oversimplification, and below a certain value of δ (approximately 20μm) this weakness becomes more evident as a result of the increased mass transport rate.

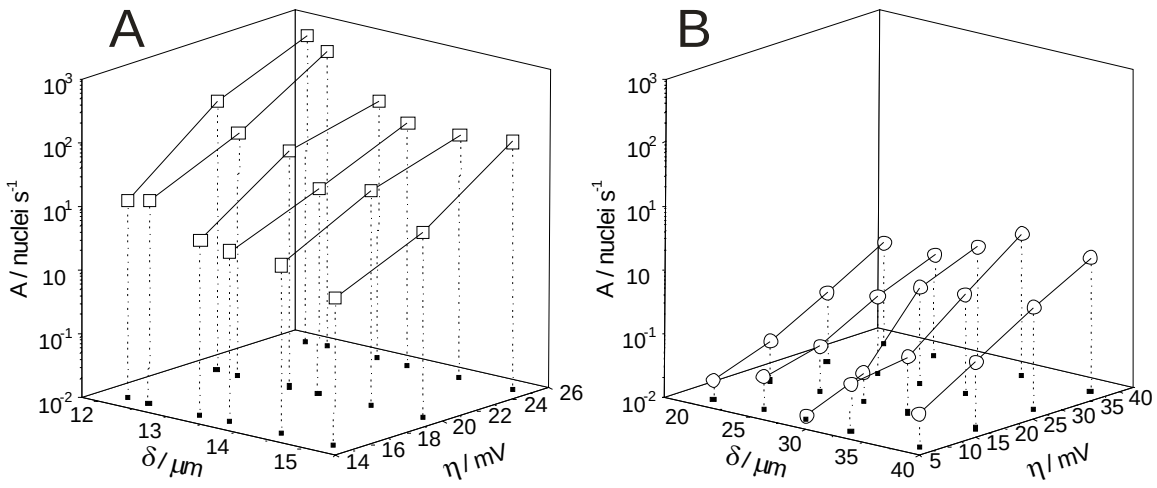

Figure 7.8: Plot of A as a function of diffusion layer thickness and overpotential. A) Flow cell data, B) Stirred cell data.

In order to compare the parameters extracted from the hydrodynamic data with quiescent data, further lead deposition experiments were performed. Lead was deposited at overpotentials of between 42 and 77 mV for 5 seconds, and ten transients recorded under each set of conditions. It was found that overpotentials below 42 mV did not produce the current increase associated with nucleation and growth. Transient analysis of silent data can be used to determine N_0A (although N_0 and A cannot be determined separately using this method). For simplicity, the method used to extract N_0A was that of initial gradients. In the absence of nucleation inhibition (i.e. the decrease in nucleation rate at longer times owing to local concentration decreases around developing nuclei),[16] the following expression describes the current response of nucleation and growth:[17]

$$J = \left[\sqrt{2} z F \pi (Dc)^{\frac{3}{2}} \left(\frac{M}{\rho} \right)^{\frac{1}{2}} N_0 A \right] . (t - t_0)^{\frac{3}{2}} \qquad (7.6)$$

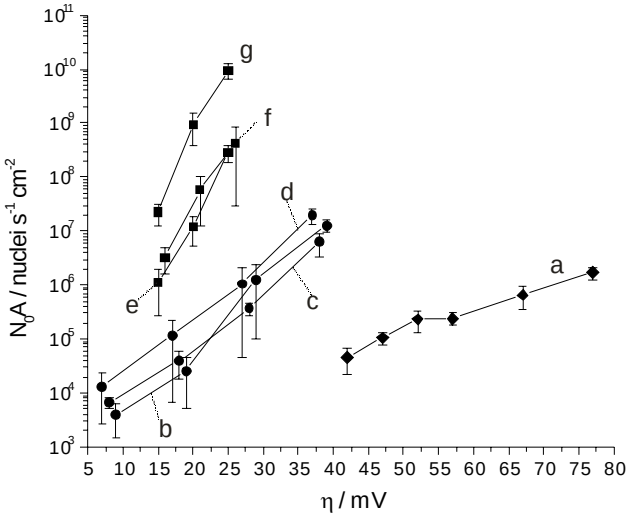

Figure 7.9: Plot of N_0A vs. overpotential at selected values of δ and under quiescent conditions. Diamonds (a): quiescent conditions. Circles show stirred cell data: δ= b) 38.5μm, c) 28.5 μm, d) 20.3 μm. Squares show flow cell data: δ= e) 15.2 μm, f) 13.2 μm, g) 10.2 μm.

Thus, a plot of log(J) vs. log(t – t_0) should have an initial gradient of 1.5, and N_0A may be determined from the intercept. In fact, this method is inaccurate at large overpotential because nucleation inhibition becomes immediately important and a gradient of 1.5 (corresponding to uninhibited growth) is never achieved. This effect was observed during the analysis of the current data set, with the gradient of the log-log plot decreasing to approximately 1.2 at the highest overpotentials; the parameters extracted should therefore be considered estimates.

Figure 7.9 shows selected N_0A (i.e. the global nucleation rate in nuclei s^{-1} cm^{-2}) values from the flow cell and the stirred cell compared to the silent values. Two important trends are evident: first, the use of hydrodynamic conditions decreases significantly the overpotential required for nucleation and growth to occur: an overpotential of around 40mV is required for nucleation to occur significantly under quiescent conditions, while less than 10mV is required under all the hydrodynamic conditions studied. Second, the use of the flow and stirred cells appear to increase the

global nucleation rate at a given overpotential compared to quiescent conditions. As we have shown that N_0 is independent of δ, this can be attributed to the *apparent* increase in A shown in figure 7.8 (see above). It is interesting to compare these observations with previous experiments in which cobalt was deposited under sonicated conditions.[4] Under sonicated conditions, it was found that again a lower overpotential was required to initiate nucleation. However, N_0A values were found to *decrease* under sonication compared to the quiescent values at the same potential. This was explained by a decrease in N_0 owing to the ablative effect of ultrasound[18] preventing nucleation on some sites or effectively reducing the number of active sites.

7.6 Conclusions

The above results confirm that equation (7.1) can be accurately fitted to the transients resulting from the potentiostatic deposition of lead under hydrodynamic conditions provided by a wall-tube electrode and a stirred cell (as well as those in which the forced convection is provided by sonication)[4] and that values for the nucleation rate, A, and the number of active sites, N_0 can be determined under most conditions; a weakness of equation (7.1) is revealed when A is large, when we find that the shape of the transient becomes independent of A. From the values of N_0 and A determined from the hydrodynamic data, we conclude that N_0 is essentially independent of the diffusion layer thickness, while it increases exponentially with increasing overpotential. As N_0 is independent of the flow conditions, this also suggests a method for determining A under quiescent conditions: N_0 may be directly determined under hydrodynamic conditions, then the quiescent value of N_0A divided by N_0 derived at the relevant overpotential.

A appears to increase with both decreasing δ and increasing η. The increase with decreasing δ may be illusory, caused by the diffusion layer approximation breaking down, particularly at values of δ less than approximately 20μm. The global nucleation appears to increase under hydrodynamic conditions compared to quiescent conditions, an observation which contrasts to that when ultrasound is used to provide forced convection.[4] This discrepancy is explained by the ultrasonic ablation effectively reducing the number of active sites.

We have demonstrated that a system involving multiple diffusion-controlled nucleation under hydrodynamic conditions can be effectively parameterized and used to extract values of N_0 and A, but in fact these are likely to deviate from the correct values, particularly as δ is decreased. This is ascribed to the failure of the diffusion layer model: we have thus begun to expose the danger inherent in using a simple parameter to approximate a complex 3-dimensional flow system.

7.7 References

[1] B. Scharifker, G. Hills, *Electrochim. Acta* **1983**, *28*, 879.
[2] M. Sluyters-Rehbach, J. H. O. J. Wijenberg, E. Bosco, J. H. Sluyters, *J. Electroanal. Chem.* **1987**, *236*, 1.
[3] M. V. Mirkin, A. P. Nilov, *J. Electroanal. Chem.* **1990**, *283*, 35.
[4] M. E. Hyde, O. V. Klymenko, R. G. Compton, *Journal of Electroanalytical Chemistry* **2002**, *534*, 13.
[5] L. N. Nekrasov, T. N. Khomchenko, V. N. Alekseev, B. M. Grafov, S. A. Martem'yanov, *Russ. J. Electrochem.* **1999**, *35*, 966
[6] D. T. Chin, C.-H. Tsang, *J. Electrochem. Soc.* **1978**, *125*, 1461.
[7] W. J. Albery, S. Bruckenstein, *J. Electroanal. Chem.* **1983**, *144*, 105.
[8] N. V. Rees, O. V. Klymenko, B. A. Coles, R. G. Compton, *J. Phys. Chem. B* **2003**, *107*, 13649.
[9] J. Melville, N. Simjee, P. R. Unwin, B. A. Coles, R. G. Compton, *Journal of Physical Chemistry B* **2002**, *106*, 2690.
[10] J. L. Melville, B. A. Coles, R. G. Compton, N. Simjee, J. V. Macpherson, P. R. Unwin, *Journal of Physical Chemistry B* **2003**, *107*, 379.
[11] J. L. Melville, N. Simjee, P. R. Unwin, B. A. Coles, R. G. Compton, *Journal of Physical Chemistry B* **2002**, *106*, 10424.

[12] A. J. Bard, L. R. Faulkner, *Electrochemical Methods - Fundamentals and Applications*, 2nd ed., John Wiley & Sons, Inc., New York, **2001**.
[13] R. N. Adams, *Electrochemistry at Solid Electrodes*, Marcel Dekker Inc., New York, **1969**.
[14] B. R. Scharifker, *Electrochem. Transition* **1992**, 499.
[15] M. Palomar-Padarvé, M. T. Ramírez, I. González, A. Serruya, B. Scharifker, *J. Electrochem. Soc.* **1996**, *143*, 1551.
[16] M. E. Hyde, R. G. Compton, *Journal of Electroanalytical Chemistry* **2003**, *549*, 1.
[17] M. E. Hyde, R. Jacobs, R. G. Compton, *Journal of Physical Chemistry B* **2002**, *106*, 11075.
[18] S. Floate, M. E. Hyde, R. G. Compton, *J. Electroanal. Chem.* **2002**, *523*, 49.

8 The Correlation of Lead Dioxide Electrocatalytic Activity with Observed Morphology

This chapter cannot be made freely available via ORA for copyright reasons. The content has been published as Hyde, M. E., Jacobs, R. M. J. & Compton, R. G. (2004). 'An AFM study of the correlation of lead dioxide electrocatalytic activity with observed morphology', Journal of Physical Chemistry B , 108(20), 6381-6390. [Available at http://dx.doi.org/10.1021/jp031263t].

This chap

9 An Electrochemical Cell for Surface Analysis

This chapter cannot be made freely available via ORA for copyright reasons. The content has been published as Davies, T. J. et al. (2005). 'Nanotrench arrays reveal insight into graphite electrochemistry', Angewandte Chemie International Edition, 44(32), 5121-5126. [Available at http://dx.doi.org/10.1002/anie.200462750].

10 Fabrication and Electrochemistry of Nanotrench Arrays on HOPG

This chapter cannot be made freely available via ORA for copyright reasons. The content has been published as Hyde, M. E., Davies, T. J. & Compton, R. G. (2005). 'Fabrication of random assemblies of metal nanobands: a general method', Angewandte Chemie International Edition, 44(40), 6491-6496. [Available at http://dx.doi.org/10.1002/anie.200502128].

11 Fabrication of Random Assemblies of Metal Nanoband Arrays: a General Method.

11.1 Introduction

Nanoscale electrodes have several advantages over their macroscopic counterparts. They are well suited to applications requiring high sweep rates, low iR drops and low capacitance.[1] A significant disadvantage of such electrodes however is that they generate extremely small currents. One useful compromise is to use a band electrode, in which the electrode is small enough in one dimension to give rise to non-linear diffusion, while its size in the other dimension is maximized in order to maximize the current output. Band electrodes are particularly favoured when attempting to achieve very low analytical detection limits: the part of the residual current associated with the double layer charging is reduced in proportion to the surface area of the electrode, while the Faradaic current is not.[2]

Nanoband electrodes are usually fabricated using one of two general methods. The simpler of these is to generate an insulator-metal-insulator sandwich and then expose one of the edges by polishing or cutting the material. If vacuum evaporated films are used, extremely narrow bands (potentially down to ~1nm) may be created. However, the technique suffers from some difficulties: the band width is defined by the deposited film thickness, which may be difficult to determine accurately. In addition, polishing of such small electrodes is likely to cause significant variations in its final shape, surface area, etc. Even when no polishing step is used, there may be significant

doubts about the real surface area of the band.[3] This method is best suited to the creation of single bands.

The second commonly used method involves using lithography. In this case there are two possibilities. First, a metal film may be evaporated on to a substrate. Photoresist is then applied and patterned lithographically. The unprotected metal is etched, and finally the remaining photoresist removed. Second, a 'lift-off' technique may be employed, in which the photoresist is applied directly to the substrate and patterned. The metal film is then applied on top. When the remaining photoresist is removed, the corresponding metal film is also removed, leaving only the metal attached directly to the substrate.[4] These methods are highly reproducible and allow precise control of the electrode geometry. Recently bandwidths and gap widths of down to 30nm have been achieved using a lift-off procedure combined with high resolution electron beam lithography.[5] Lithographic methods however require specialized equipment and are relatively complex to implement.

A related approach to the modification of surfaces with conductive bands has been explored by Penner et al.[6-8] who have shown that metal nanowires may be obtained by selective electrodeposition of conducting metal oxides on to the step edges present at highly ordered pyrolytic graphite (HOPG) surfaces, followed by reduction in hydrogen (although the direct deposition of metals on to the step edges is possible and conceptually simpler, the resulting wires are usually of poorer quality for various reasons).[8] This effect results from the specialized structure of HOPG: it consists of atomically flat basal plane graphite terraces separated by defects exposing relatively thin (335 pm or multiples thereof) bands of edge plane graphite. Given the correct

deposition potential, these edges are strongly favoured owing to their much greater electrochemical activity.[9-11]

The previous chapter extended this methodology in a three-step electrochemical process to generate nanotrenches.[9] In the following chapter, this method is further developed: a simple, general, mostly solution phase method for generating assemblies of metal nanobands using the original MoO_2 nanowires as a template is presented.

11.2 Experimental Details

The reagents used were sodium molybdate (Aldrich, 98+%), potassium chloride (≥ 99.5 %, Reidel-de-Haen), sodium chloride (BDH, AnalaR®), ammonium chloride (BDH, GPR), sodium hydroxide (Acros, ≥98 %), hexaammineruthenium(III) chloride (98 %, Aldrich), sulphuric acid (sp. gr. 1.84, BDH, AnalaR®), sodium sulphide (Aldrich, 98+%), tetrabutylammonium perchlorate (Fluka, puriss electrochemical grade) and divinylbenzene (DVB, Aldrich, 80%, mixture of isomers). DVB solutions were prepared using acetonitrile (Fischer Scientific, anhydrous synthesis grade). In all experiments the temperature was 294 ± 2 K.

The metal layers were prepared on the HOPG by metal vapour deposition in a BOC Edwards Auto 306 vacuum coater with Cryo-pumping system (giving a base pressure of $2x10^{-7}$ mBar). The metals were evaporated from an alumina coated molybdenum boat (R. D. Mathis, Long Beach, CA), using a 3.2V 300A power supply. The current was controlled so that the rate of deposition on the sample was maintained at about 1nm/s monitored using a quartz crystal microbalance (FTM5 thickness monitor, BOC Edwards) which was mounted adjacent to the sample, both 120 mm from the evaporation source. During the evaporation the sample was rotated at about 5 rpm,

around a circle of radius 50 mm centred directly above the source, with the pressure maintained below $1x10^{-6}$ mBar. The evaporation was stopped once the film had reached the required thickness and the system was allowed to cool to room temperature before venting and removing the sample. Gold and silver were obtained from Alfa, purity 99.99%. Copper was obtained from Goodfellow, purity 99.999%.

11.3 Nanoband Fabrication

The process for fabricating these nanoband assemblies is illustrated conceptually in figure 11.1. Using a solution containing 1.1mM sodium molybdate, 1M sodium chloride and 1M ammonium hydroxide adjusted to pH 8.5 with sodium hydroxide, MoO_2 nanowires were electrodeposited on to the freshly cleaved HOPG surface (figure 11.1a). The mean thickness of the nanowires has been shown to be dependent on the deposition time, allowing the preparation of wires with controlled diameters; this is discussed further below. In the present case, deposition was performed at -1.0V (*vs.* SCE) for 130s (figure 11.1b). An AFM image of the resulting nanowires is shown in figure 11.2a. In order to test the homogeneity of the nanowire coverage, AFM images were collected at several separated points on the electrode; this image (and those presented below) were found to be representative of the whole electrode.

The second step is again to cover the remaining exposed carbon with a layer of polymer. Instead of using 4-nitrobenzenediazonium however, we use an acetonitrile solution containing 50 mM divinylbenzene and 0.1 M tetrabutylammonium perchlorate. Divinylbenzene has been shown to readily polymerize under oxidizing conditions,[12] and we find that applying +1.6V for 30s reproducibly generates an even, insulating film with a thickness of approximately 5-10 nm (figure 11.1c).

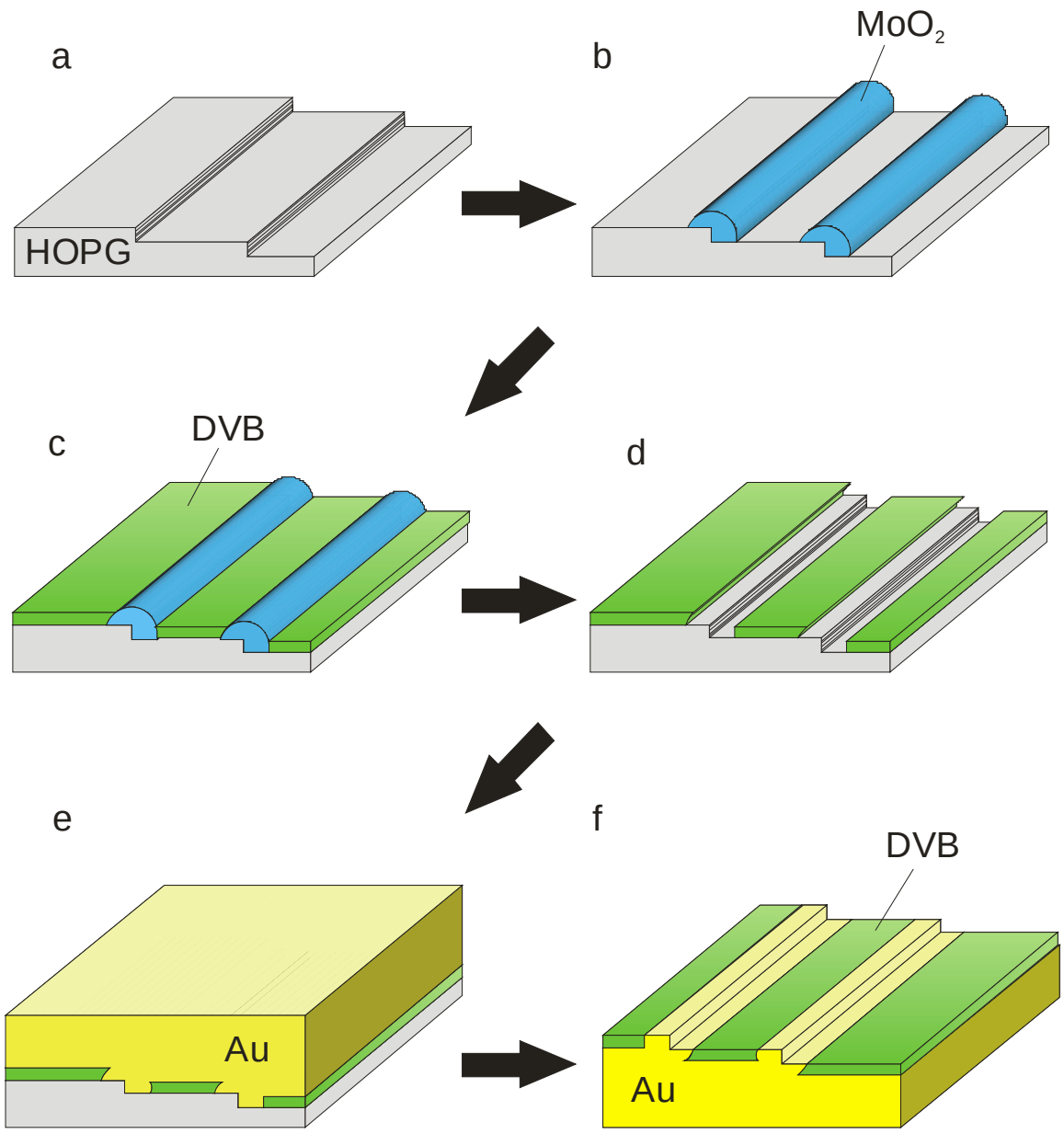

Figure 11.1: Schematic diagram showing the six stages involved in the metal nanoband fabrication.

The nanowires are removed and nanotrenches created by immersing the HOPG electrode in a stirred solution of 1M hydrochloric acid for 300s (figure 11.1d). An AFM image of these nanotrenches is shown in figure 11.2b; the texture of the DVB film is clearly visible when compared to the background HOPG in figure 11.1a, and the nanotrenches have a mean depth of approximately 6 nm.

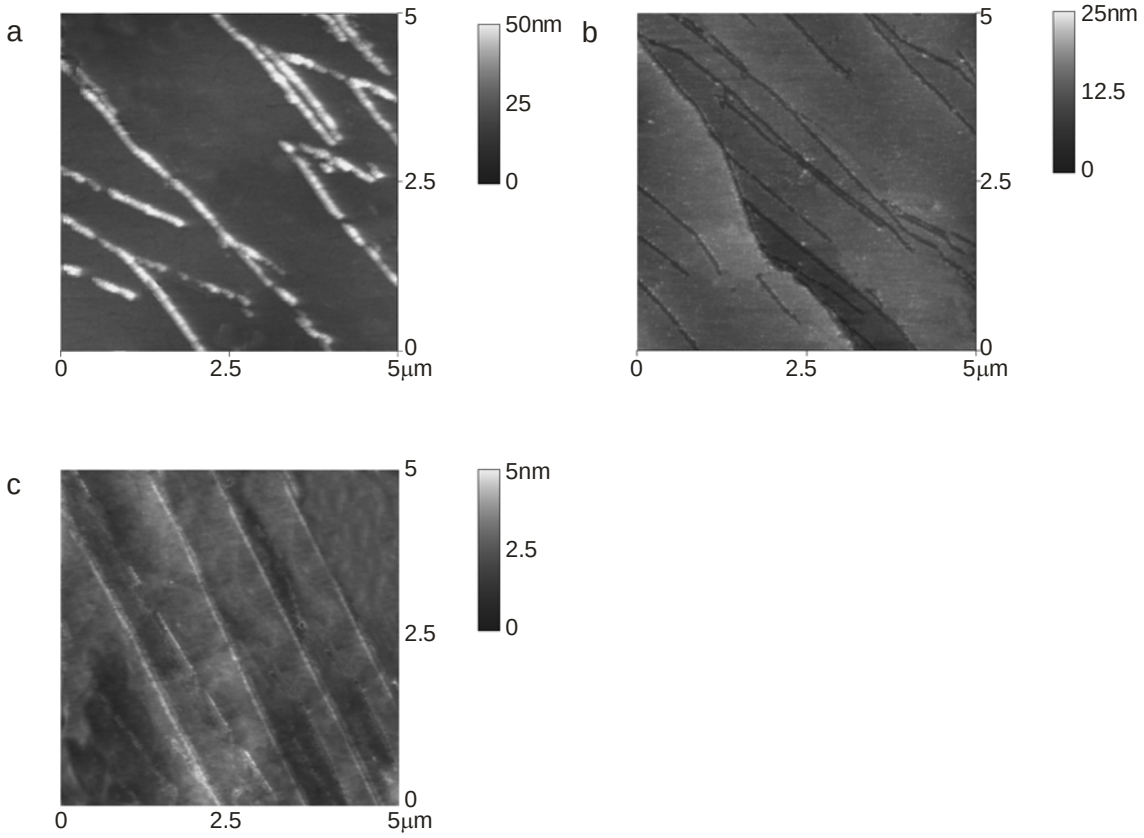

Figure 11.2: AFM images showing steps in nanoband fabrication. a) MoO_2 nanowires, corresponding to figure 11.1b. b) Nanotrenches, corresponding to figure 11.1d. c) Completed gold nanobands, corresponding to figure 11.1f. See the main text for full details.

The electrode is removed from the acid, rinsed and dried. A layer of gold 200nm thick is then evaporated on top of the nanotrenches using the conditions described in the experimental section, and a supporting stub attached to the gold layer using cyanoacrylate adhesive (figure 11.1e). Finally the HOPG is cleaved using a knife as close to the gold layer as possible. The original HOPG block is regenerated and any thin layer of HOPG remaining on top of the gold layer may be removed with adhesive tape, leaving what was originally the underside of the gold layer exposed. We find that the DVB layer adheres preferentially to the gold (rather than the HOPG), leaving the structure illustrated in figure 11.1f, with exposed gold nanobands surrounded by

an insulating layer of polymer.* An AFM image of these bands is shown in figure 11.2c. Note the decreasing Z scale in figure 11.2a-c; the nanobands are somewhat difficult to resolve owing to the very small height difference between the DVB layer and the exposed gold. This small height difference might be predicted from figure 11.1f; in theory the edges of the bands should be flush with the top of the DVB layer.

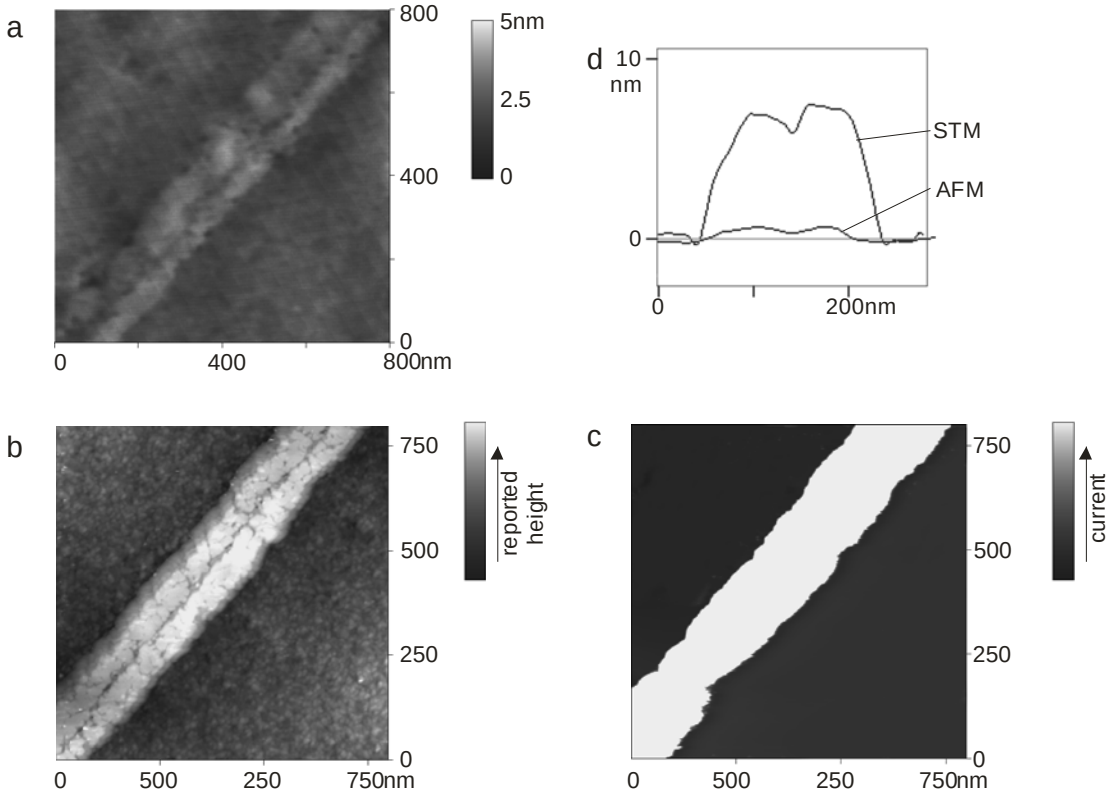

Figure 11.3: A single gold nanoband shown at a scan range of approximately 800nm. a) AFM image (height). b) Constant current STM image (height). c) Constant height STM image (current). d) Section analyses perpendicular to the band axis from the AFM and constant current STM images. See text for further details.

In order to study the nanobands in more detail, a representative band was chosen and examined at a scan range of approximately 800nm. An AFM image of this band is shown in figure 11.3a, along with a section analysis of a line perpendicular to the nanoband axis in figure 11.3d. Some important features are apparent: the width of the

* AFM on the HOPG surface separated from the gold showed no sign of nanotrenches, confirming that the polymerised DVB deposit adheres to the gold.

nanoband is around 180 nm and the maximum height of the nanoband above the polymer layer is approximately 700 pm. The band also has a characteristic 'm' shape. The depth of the central 'v' is approximately 300 pm, suggesting that this is related to the shape of the original HOPG step edge. The sample was next analyzed using STM. Initially the scan feedback parameters were increased as much as possible ('constant current' mode). On typical surfaces (in which the conductivity is uniform), this procedure gives the most accurate reproduction of the real surface. However, in the current case we find that although the texture of the background and the band itself are well resolved, the height of the band is over-reported by a factor of 10 (figure 11.3d). In addition, when the feedback parameters are minimized ('constant height' mode), the STM current appears as in figure 11.3c. Together these observations are direct evidence of the presence of the DVB film. In constant height mode, the bias is set high enough for electrons to tunnel through the DVB film. When the tip reaches a nanoband, the hugely higher conductivity of the gold causes the tip to overcompensate, moving a large distance away to maintain the same current. For this reason, the absolute heights recorded in constant current STM mode should be considered unreliable, and have been omitted from the relevant figures. In constant height mode, the tip remains at a fixed height (irrespective of any surface features) and the tunnelling current is recorded. Clearly we would expect the gold areas, with their higher conductivity, to pass a much greater current at a given bias potential, exactly as observed.

In principle, the method described above for the generation of nanobands should be effective for any material that can be evaporated on to the nanotrenches. In order to test this, the procedure described above was repeated exactly, except silver was used

instead of gold in the evaporation step. It was found that the resulting nanobands were impossible to resolve using AFM, owing to the small height of the bands compared to the roughness of the surface. Again, however, the bands are clearly visible when constant current STM is used. STM images at two scan ranges are shown in figure 11.4.

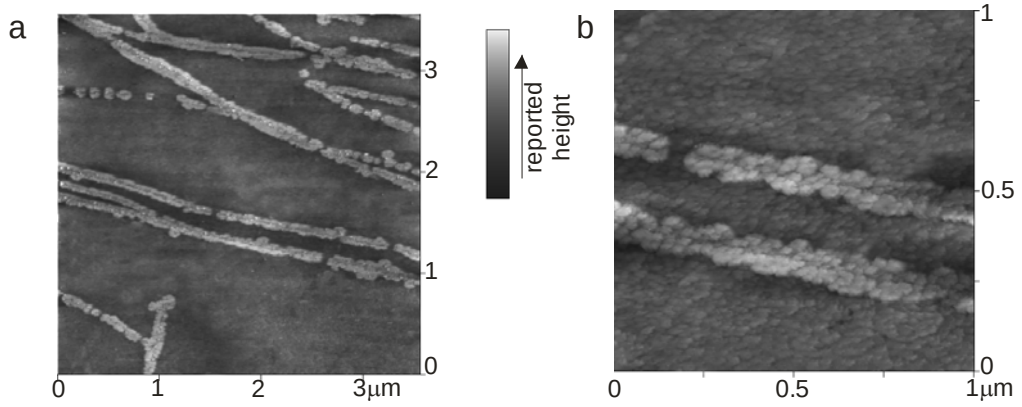

Figure 11.4: Constant current STM images of silver nanobands.

Again, the 'm' shape is visible, and the bands shown in figure 11.4b have a width of around 150 nm, consistent with the results for the gold nanobands (given that some variation in nanowire/nanotrench width over the whole electrode is always observed).

As stated above, it should also be possible to control the mean nanoband width by adjusting the length of time for which MoO_2 is deposited. To test this, the above procedure was again repeated. However, this time MoO_2 was deposited at -1.0V for 30s. The result is shown in figure 11.5a: finer nanowires are produced, in this case having a mean diameter of approximately 80-90 nm. Nanotrenches were produced as usual from these wires, and 200 nm of copper evaporated on to the surface. After cleaving, again no nanobands could be distinguished using AFM, but STM clearly reveals their presence (figure 11.5b and c). As expected, the bands are narrower than

in the two previous cases: the zoomed image in figure 11.5c shows a typical band having a width of 100 nm.

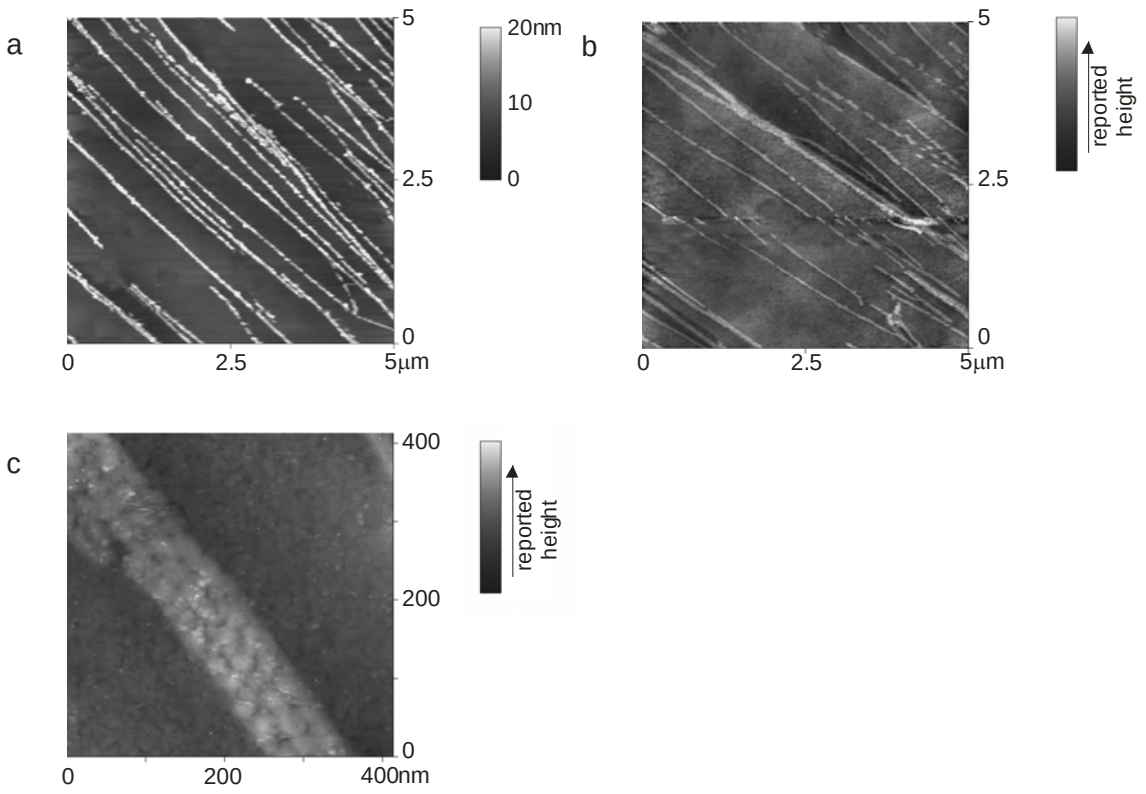

Figure 11.5: a) AFM image of MoO_2 nanowires after deposition for 30s. b) and c) Constant current STM images of copper nanobands made using the nanowires in a).

11.4 Voltammetric Analysis

The nanoband arrays produced using this method were then analysed voltammetrically. An important parameter for any type of electrode array is the global coverage, Θ, defined by equation (11.1):

$$\Theta = \frac{A_{ins}}{A_{array}} \tag{11.1}$$

where A_{ins} is the area of insulating material and A_{array} is the total surface area of the array. It follows that the area of electrode material is given by $A_{array}(1-\Theta)$. Now consider the case where we perform cyclic voltammetry at an electrode of material *i* in a simple one electron redox couple given by pathway A:

$$A + e \underset{\leftarrow}{\overset{k^{\circ},\alpha}{\rightarrow}} B \qquad \text{(A)}$$

where k^o is the electron transfer rate constant and α is the symmetry coefficient for the heterogeneous reaction. The observed response is dependent on a number of system parameters such as the diffusion coefficient, D, the area of the electrode, A_{elec}, and k^o. For the purpose of this argument, we label the whole response as [I-E(k^o)]. Now consider the case where we have a nanoband array of material i and global coverage Θ in the same redox couple, and $A_{array} = A_{elec}$. Previous work has shown that if the spacing between the individual bands is considerably smaller than the diffusion layer thickness, δ, the CV response will be given by [I-E(k^o(1-Θ))].[10, 13] That is, the I-E response of the array will be equal to that of a naked electrode of the same area, in the same redox couple but with an electron transfer rate constant of k^o(1-Θ).

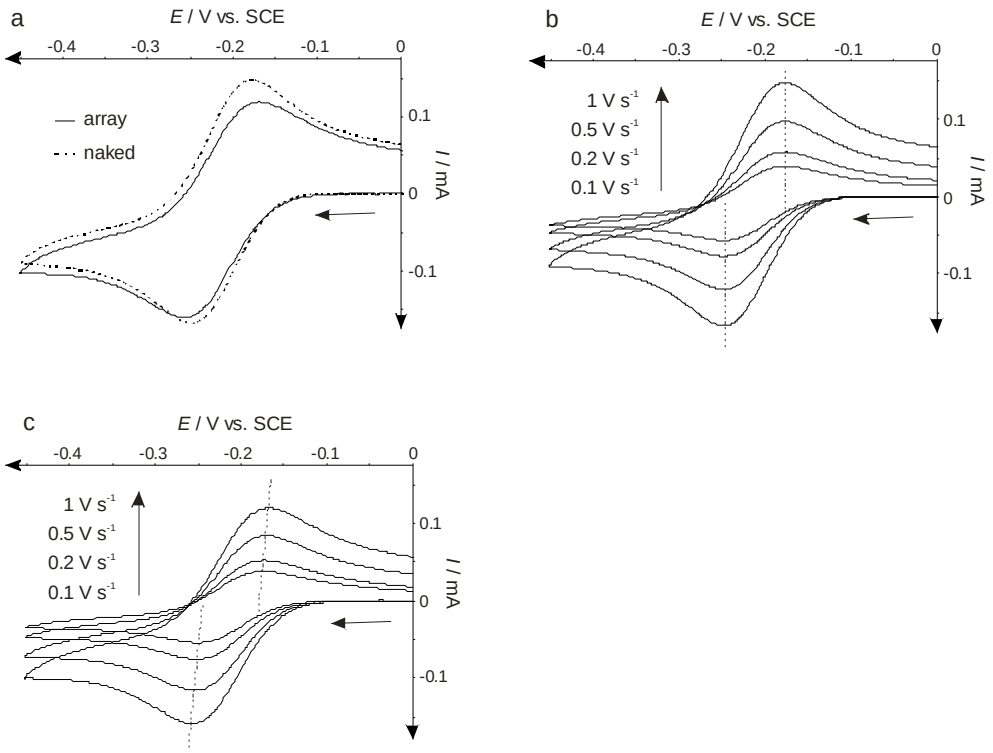

Figure 11.6: a) Cyclic voltammogram taken at 1 V s^{-1} in 1.0 mM $Ru(NH_3)_6^{3+}$ / 1 M KCl at the gold nanoband array in figure 11.2c (solid) and a gold electrode of the same surface area (dashed). b) and c) Cyclic voltammograms taken at varying scan rates in 1.0 mM $Ru(NH_3)_6^{3+}$ / 1 M KCl at the gold electrode (b) and the gold nanoband array (c).

Figure 11.6a illustrates a cyclic voltammogram recorded with the gold nanoband array in figure 11.2c immersed in 1.0 mM $Ru(NH_3)_6^{3+}$ / 1 M KCl where the scan rate is 1 V s^{-1}. Overlaid as a dashed curve is the corresponding response for a gold electrode of the same surface area, i.e. $A_{elec} = A_{array}$ (in this case the gold electrode was prepared via gold plating a metal slab and was used in the same electrode housing as the array). Although the coverage of the nanoband array is ~90 %, meaning only 10 % of the array surface is gold, we observe an *I-E* response almost equal in magnitude to that of the "naked" gold electrode. In addition the peak to peak separation for the array is larger than that for the naked electrode. This observation is in complete agreement with the theory discussed above. At 1 V s^{-1} the diffusion layer thickness at the peak potential of the forward scan will be ~15 μm.[14] From figure 11.2c we can see that the spacing between the bands is less than 1 μm. Therefore, we would expect the observed response in figure 11.6. The fact that the nanoband array with coverage $\Theta \sim 0.9$ gives a response almost equal in magnitude to that of the naked electrode indicates mass transport to the nanobands must be considerably faster than to the naked electrode. A potential application of this is illustrated by figures 11.6b and c, which illustrate cyclic voltammograms recorded at various scan rates in the same solution as in 6a at the naked gold electrode (b) and the gold nanoband array (c). The $Ru(NH_3)_6^{3+}$ / $Ru(NH_3)_6^{2+}$ redox reaction has an electron transfer rate constant of ~0.5 cm s^{-1} at gold electrodes, making it electrochemically reversible at the scan rates employed in 6b.[15, 16] Hence, in figure 11.6b we observe the same peak to peak separation, ΔE_p, (~60 mV) at all scan rates. In this situation, only thermodynamic data for the redox reaction can be deduced and we would have to go to much higher scan rates (or smaller electrodes) to deduce reliable kinetic data.[15, 16] However, the nanoband array effectively reduces k^o to $(1-\Theta)k^o$, such that the redox reaction now

appears to be quasi-reversible at the scan rates employed, as shown in figure 11.6c where ΔE_p increases with scan rate. Thus, well characterised nanoband arrays could have fundamental applications (i.e. alternative methods to investigate fast electron transfer reactions) in addition to their use in electroanalysis.

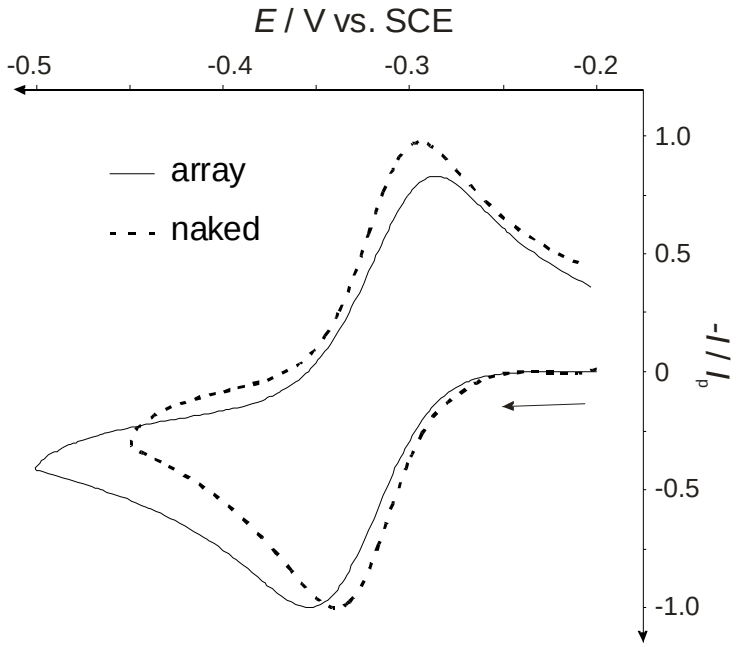

Figure 11.7: Cyclic voltammograms taken at 0.2 V s^{-1} in 2.5 mM Na_2SO_3 / 1 M H_2SO_4 at the copper nanoband array in figure 11.5 (solid) and a copper macroelectrode (dashed).

Similar voltammetric characteristics were observed for the other arrays in a range of redox systems. For example, figure 11.7 illustrates cyclic voltammograms recorded at 0.2 V s^{-1} in 2.4 mM Na_2SO_3 and 1 M H_2SO_4 at the copper nanoband array in figure 11.5 (solid) and a naked copper electrode. As reported by Wain and co-workers, at this pH, the *I-E* curve represents the 2 electron reduction of aqueous SO_2 which is electrochemically reversible at 0.2 V s^{-1}, with a peak to peak separation of ~60 mV.[17] However, the nanoband array effectively reduces the electron transfer rate constant, making the system appear quasi reversible.

In conclusion, we have demonstrated a method for generating large assemblies (of a size limited only by the HOPG block employed) of metal nanobands. The method has been shown to be effective for generating gold, silver and copper nanobands, and may work with any material that can be evaporated on to the electrode surface to form a stable, 200 nm thick layer. Control of the mean nanoband width has also been demonstrated: by varying the MoO_2 deposition time, we have created bands with widths between approximately 90 and 180 nm. In principle the method can be easily extended to produce narrower bands simply by decreasing the deposition time further. However, in practice we found this somewhat problematic as shorter deposition times tended to produce 'patchier', less continuous nanowires. Conversely, wider nanobands can be produced by increasing the deposition time. Although not considered in the present study, it should also be possible to vary the nanoband density. The band density is a function of the density of step edges on the HOPG surface: it could therefore be decreased by employing a higher grade of HOPG, or increased by using a lower grade.[18] The method of preparing a fresh HOPG surface can also affect the edge step density. For example, McDermott and McCreery found that cleaving an HOPG surface with a sharp blade results in far less edge steps than the adhesive cleaving technique employed in this work.[19]

11.5 References

[1] M. Samuelsson, M. Armgarth, C. Nylander, *Anal. Chem.* **1991**, *63*, 931.
[2] J. Wang, X. Rongrong, T. Baomin, J. Wang, C. L. Renschler, C. A. White, *Analytica Chimica Acta* **1994**, *293*, 43.
[3] S. L. Caston, R. L. McCarley, *J. Electroanal. Chem.* **2002**, *529*, 124.
[4] R. W. Dyson, *Specialty Polymers*, Chapman and Hall, New York, **1987**.
[5] K. Ueno, M. Hayashida, J.-Y. Ye, H. Misawa, *Electrochem. Comm.* **2005**, *7*, 161.
[6] M. P. Zach, K. Inazu, K. H. Ng, J. C. Hemminger, R. M. Penner, *Chem. Mater.* **2002**, *14*, 3206.
[7] M. P. Zach, K. H. Ng, R. M. Penner, *Science* **2000**, *290*, 2120.

[8] E. C. Walter, M. P. Zach, F. Favier, B. J. Murray, K. Inazu, J. C. Hemminger, R. M. Penner, *ChemPhysChem* **2003**, *4*, 131.
[9] T. J. Davies, M. E. Hyde, R. G. Compton, *Angew. Chem., Int. Ed.* **2005**, In press.
[10] T. J. Davies, R. R. Moore, C. E. Banks, R. G. Compton, *J. Electroanal. Chem.* **2004**, *574*, 123.
[11] C. E. Banks, T. J. Davies, G. G. Wildgoose, R. G. Compton, *Chem. Commun.* **2005**, 829.
[12] H. O. Finklea, R. S. Vithanage, *J. Electroanal. Chem.* **1984**, *161*, 283.
[13] C. Amatore, J. M. Savéant, D. Tessier, *J. Electroanal. Chem.* **1983**, *147*, 39.
[14] T. J. Davies, E. R. Lowe, S. J. Wilkins, R. G. Compton, *ChemPhysChem* **2005**, in press (DOI 10.1002/cphc200500152).
[15] H. Matsuda, Y. Ayabe, *Zeitschrift fuer Elektrochemie und Angewandte Physikalische Chemie* **1955**, *59*, 1059.
[16] H. Matsuda, Y. Ayabe, *Zeitschrift fuer Elektrochemie und Angewandte Physikalische Chemie* **1955**, *59*, 494.
[17] I. Streeter, A. J. Wain, R. G. Compton, *J. Phys. Chem. B* **2005**, submitted.
[18] https://secure.2spi.com/catalog/new/hopgsub.shtml.
[19] M. T. McDermott, R. L. McCreery, *Langmuir* **1994**, *10*, 4307.
[20] R. Bowler, T. J. Davies, M. E. Hyde, R. G. Compton, *Anal. Chem.* **2005**, *77*, 1916.

12 Final Conclusions

In this thesis, various different applications of microscopic and voltammetric techniques to the analysis of growing deposits on electrode surfaces have been described. Broadly speaking, these may be divided into the following categories:

- **Analytical applications.** Studying the limitations of carbon electrodes with respect to anodic stripping voltammetry using AFM and optical microscopy has shed new light on the processes occurring during the deposition and stripping stages.
- **Instrumentation improvements.** A new design for a housing for HOPG electrodes has been described, and deposition of molybdenum oxide nanowires used to demonstrate the benefits of this system. These include improved reproducibility, ease of use, and the ability to remove the HOPG slab for microscopic analysis.
- **Fundamental studies.** Examining the potentiostatic deposition of silver on to boron doped diamond using in-situ optical microscopy, combined with computer modelling of an idealized deposition system, have provided new insights into the process of diffusion controlled multiple nucleation. The growth of lead deposits on a glassy carbon electrode under hydrodynamic conditions has allowed the investigation of the accuracy of a recently derived model for such processes, as well as improving the general understanding of deposition under hydrodynamic conditions. Using in-situ AFM to analyze the morphology of lead dioxide deposits on boron-doped diamond has shown a previously unrecognised correlation

between deposition pH and potential, deposit morphology, and deposit electrocatalytic activity.

- **Novel electrode fabrication.** The unusual properties of HOPG are exploited to generate ‘nanotrenches’. Using a simple, three-step process, the basal planes of the HOPG are covered in a thin, impermeable polymer layer, while the edge defects remain exposed. The fundamental aspects of this result have also been explored, as it provides new insights into the electrochemical behaviour of bare HOPG electrodes. In addition, the principles of the nanotrench method have been extended to form gold, silver and copper nanoband arrays, having unusual electrochemical properties.

In conclusion, this thesis has demonstrated how atomic force microscopy, scanning tunnelling microscopy, and optical microscopy, both in- and ex-situ, may be usefully applied to wide-ranging areas of deposition electrochemistry. In some cases, such as in the deposition of silver, the addition of microscopic data to the electrochemical data provides new insights into the processes occurring. In other cases, such as the fabrication of nanowires and nanotrenches, the procedures would be impossible without the use of these microscopic techniques.

13 Appendices

13.1 Appendix 1: Symbols

In cases where the same symbol has several meanings, the usage is made clear in the text.

A	1) Electrode area / cm^3
	2) Nucleation rate constant / nuclei per active site per second
a	Nucleus area / cm^2
A_0	Initial nucleation rate constant / nuclei per active site per second
A_c	Nucleation threshold rate / nuclei per active site per second
a_{mean}	Mean nucleus area / cm^2
α	1) Charge transfer coefficient
	2) A parameter measuring the degree of instantaneous/ progressive nucleation, defined as $(2\pi)^{\frac{3}{2}} D\left(\frac{cM}{\rho}\right)^{\frac{1}{2}}\left(\frac{N_0}{A}\right)$
	3) Symmetry coefficient
B	Constant defined as $2\sqrt{2}\pi\left(\frac{Mc}{\rho}\right)^{\frac{1}{2}} D^{\frac{1}{2}}\delta N_0$
C	Capacitance / F
c_0	Bulk concentration / mol dm^{-3}
c_c	Nucleation threshold concentration / mol dm^{-3}
C_i	Concentration of species i / mol dm^{-3} or mol cm^{-3}
c_i	'Inhibited' concentration / mol dm^{-3}
c_s	Concentration at the surface of a nucleus / mol dm^{-3}
D_i	Diffusion coefficient of species i / cm^{-2} s^{-1}
d	1) Centre to centre nucleus distance / cm
	2) Nozzle diameter / cm
$\bar{d}$	Mean nearest neighbour distance / cm
d_c	Nucleation exclusion zone radius / cm
ΔE_p	Peak to peak separation (on a CV) / V
δ	1) Diffusion layer thickness / cm
	2) Radial flux / mol cm^{-2} s^{-1}
E	Potential (applied to a cell) / V
E^0	Standard electrode potential / V
E_f^0	Formal potential / V
F	Faraday constant, 9.649 x 10^4 C mol^{-1}
Φ	Electrostatic potential / V
G	Nucleation inhibition parameter
γ_i	Activity coefficient of species i
η	Overpotential / V
i	1) Current between working and counter electrodes / A or A cm^{-2}

	2) Current to a single nucleus / A
I	Total current to an array of nuclei / A
I_0	Baseline current / A
I_m	Maximum current / A
I_p	Peak current / A
J	1) Flux / mol cm^{-2} s^{-1}
	2) Current density / A cm^{-2}
j_0	Current offset / A cm^{-2}
J_{lim}	Limiting current density / A cm^{-2}
k	1) Overall rate constant
	2) Boltzmann constant, 1.3807 x 10^{-23} J K^{-1}
k^0	Electron transfer rate constant / cm s^{-1}
λ	Dummy variable used in the SRWBS equation
M	Molar mass of depositing species / mol g^{-1}
N	1) Amount of substance / mol
	2) Nucleus density / cm^{-2}
N_0	Number density of active sites / cm^{-2}
N_0A	Global nucleation rate / nuclei s^{-1} cm^{-2}.
n_k	Critical nucleus size / atoms
N_{sat}	Saturation nucleus number density / cm^{-2}
ν	1) Number density of particles / cm^{-2}
	2) Kinematic viscosity / cm^2 s^{-1}
P	Nucleation probability
Q	Charge / C
Θ	Proportion of edge plane defects to basal plane graphite on HOPG
θ	Fractional area occupied by an array of nuclei
θ_{ex}	'Extended area' – theoretical fractional area occupied by an array of nuclei without including nucleus overlap
R	1) Molar gas constant, 8.1345 J K^{-1} mol^{-1}
	2) Resistance / Ω
r	1) Radius of a nucleus / cm
	2) Nearest neighbour distance / cm
r_d	Diffusion zone radius / cm
Re	Reynolds number T Absolute temperature / K
ρ	Density of depositing species / g cm^{-3}
t	Time / s
t_0	Induction time between application of a potential to the cell and nucleation beginning / s
t_m	Time at which maximum current is observed / s
u	Nucleus age / s
$\bar{u}$	Average nozzle exit velocity / cm s^{-1}.
v	Scan rate / V s^{-1}
V	1) Volume of a nucleus / cm^3
	2) Volume of space in which new nuclei can appear / cm^3
v'	Untransformed volume / cm^3
V_{1ex}	Total extended volume – theoretical fractional volume occupied by an array of nuclei without including nucleus overlap
v_{1ex}	Extended volume of a single nucleus
V_i'	Total transformed volume per unit volume shared by i overlapping grains of new phase

V_1	Real total volume per unit volume of new phase
[X]	Concentration of species X / mol cm^{-3}
x	Distance along arbitrary axis x / cm
z	Stoichiometric number of electrons transferred.

13.2 Appendix 2: The Avrami Theorem

Avrami[1, 2] considered a new phase nucleated by 'germ nuclei' (equivalent to active sites), having a number density $\overline{N}$. The number of actual germ nuclei per region ($N(t)$) then decreases in two ways: a) through becoming active growth nuclei, and b) by being swallowed by another nearby growing nucleus. At a given (sufficiently long) time, the active nuclei will have grown and to some extent overlapped (the assumption being that growth ceases in the overlapped region), leading to a situation such as that illustrated in figure 13.1. The hypothetical volume of any grain had its growth not been impeded by overlap is denoted the 'extended volume', v_{1ex}. Clearly the total extended volume per unit volume, V_{1ex}, is then

$$V_{1ex} = \int_0^t v_{1ex}(t,u)\, N(u)\, dt \tag{13.1}$$

where v is the volume of a single nucleus and u is the time of that nucleus' birth. As figure 13.1 shows, the extended grains may overlap each other in various ways. The total transformed volume per unit volume which is not overlapped is therefore denoted V_1', while the total volume of extended regions shared by two grains is V_2', three regions V_3', etc.

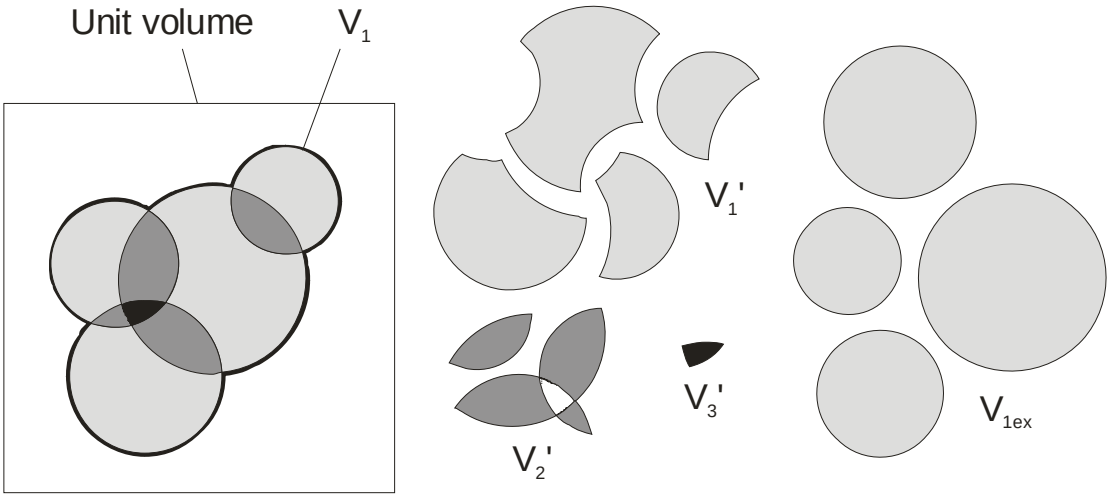

Figure 13.1: Schematic projection of overlapping spherical grains at a given time, indicating Avrami's designations of the various portions of the volume.

For the purposes of analysing overlap of diffusion zones, we next require a relation between V_{1ex} and the real total volume per unit volume of the new phase, V_1. On average, the ratio of the volume shared by no grains (i.e. untransformed volume), v', to extended volume, v_{1ex}, in any randomly selected region is equal to the density of untransformed matter at that time:

$$\frac{v'}{v_{1ex}} = 1 - V_1 \tag{13.2}$$

If new nuclei appeared entirely at random, equation (13.2) could immediately be applied to the total extended volume. However, any actual nucleus is not located randomly within the entire unit volume; it must lie somewhere outside the transformed region $V_1(u)$ at the time u of its origin. This can be circumvented by also considering 'phantom' grains: those grains associated with nuclei which would have grown, had they not been absorbed by other nuclei. Avrami demonstrates that the actual contribution of these phantom grains to V_1' and V_1 are zero, and hence

equation (13.2) may be summed over all grains (including phantoms) in a unit volume to give

$$\frac{V_1'}{V_{1ex}} = 1 - V_1 \tag{13.3}$$

Now, the same reasoning may be applied to the nonoverlapped and extended increments in grain size, rather than the volumes themselves. Hence, for an average grain (including phantom grains),

$$\frac{dv_1}{dv_{1ex}} = 1 - V_1 \tag{13.4}$$

and per unit volume

$$\frac{dV_1}{dV_{1ex}} = 1 - V_1 \tag{13.5}$$

This may now be integrated to give what is generally known as Avrami's theorem:

$$V_1 = 1 - e^{(-V_{1ex})} \tag{13.6}$$

Avrami's theorem was originally expressed in terms of volumes rather than areas, but is equally applicable to surface areas.

Note that some models use the theory of Evans[3] instead of that of Avrami; in fact it is mathematically equivalent,[4] as are several other methods sometimes quoted.[5-7] See Bosco[8] for some useful further insights into Avrami's theorem.

13.3 Appendix 3: Derivation of an Expression for Nucleation Under Conditions of Forced Convection

We initially assume that a general expression for the nucleation rate is given by

$$\frac{dN}{dt} = A\left(N_0 - N\right) \tag{13.7}$$

where N is the number density of nuclei at time t, N_0 is the saturation nucleus density (which can be considered as the number of active sites or the reciprocal of the area required for a nucleus),[9] and A is the nucleation rate constant, expressed as nuclei per active site per second per square cm. Clearly, also

$$N = N_0\left[1 - \mathrm{e}^{-At}\right] \tag{13.8}$$

Next, consider the radial flux, J_r, to an isolated hemispherical nucleus. The total amount of material diffusing per unit time to the centre at time $t = \left(t - u\right)$ where u is the time of appearance of the nucleus is given by:

$$-2\pi r^2 J_r = 2\pi r D c \tag{13.9}$$

where r is radius of the nucleus, D is the diffusion coefficient of the depositing species, and c is its concentration. If the equivalent area of plane surface towards which the same amount of material diffuses by linear diffusion is given by πr_d^2, in which r_d is the radius of the diffusion zone then the amount of material diffusing to that area in unit time is given by

$$-2\pi r^2 J_r = -\pi r_d^2 J_p \tag{13.10}$$

in which J_p is the flux to the plane area. In fact, under uniformly accessible convective conditions, this amount of material is[10]

$$-\pi r_d^2 J_p = \pi r_d^2 \frac{Dc}{\delta} \tag{13.11}$$

where δ is the diffusion layer thickness.

Comparing equations (13.9)and (13.11) gives

$$\pi r_d^2 = 2\pi r\delta \tag{13.12}$$

Next we consider the radius of the growing hemispherical nucleus. It is generally accepted that a reasonable approximation to r is[9, 11]

$$r = \left(\frac{2DcM}{\rho}\right)^{\frac{1}{2}} (t-u)^{\frac{1}{2}} \tag{13.13}$$

where M and ρ are the molar mass and density of the depositing species respectively. Hence,

$$\pi r_d^2 = 2\sqrt{2}\pi\left(\frac{Mc}{\rho}\right)^{\frac{1}{2}} D^{\frac{1}{2}} (t-u)^{\frac{1}{2}}\delta \tag{13.14}$$

If N 'independent' nuclei form by time t, then the total ('extended') coverage, θ_{ex}, is given by

$$\theta_{ex} = \int_0^t \frac{dN}{du}\pi r_d^2 du \tag{13.15}$$

Using $\frac{dN}{du} = AN_0 e^{-Au}$, and substituting equation (13.14) into (13.15), we find that the extended coverage is:

$$\theta_{ex} = 2\sqrt{2}\pi\left(\frac{Mc}{\rho}\right)^{\frac{1}{2}} D^{\frac{1}{2}}\delta AN_0 \int_0^t (t-u)^{\frac{1}{2}} e^{-Au} du \tag{13.16}$$

To calculate the total current density, we now use $I = zF\frac{Dc}{\delta}$, combined with the Avrami theorem:[2]

$$I = zF\frac{Dc}{\delta}\theta = zF\frac{Dc}{\delta}\left(1-e^{-\theta_{ex}}\right) \tag{13.17}$$

giving the result:

$$I = zF\frac{cD}{\delta}\left[1-\exp\left(-BA\int_0^t (t-u)^{\frac{1}{2}} e^{-Au}du\right)\right] \tag{13.18}$$

where $B = 2\sqrt{2}\pi\left(\frac{Mc}{\rho}\right)^{\frac{1}{2}} D^{\frac{1}{2}}\delta N_0$.

In order to evaluate the integral in equation (13.18), we use the substitution $x = \frac{t-u}{t}$,

and so

$$\int_0^t (t-u)^{\frac{1}{2}} e^{-Au}du = t^{\frac{3}{2}}e^{-At}\int_0^1 x^{\frac{1}{2}}e^{Atx}dx \tag{13.19}$$

$$= t^{\frac{3}{2}}e^{-At}\left(\frac{e^{At}}{At} - \frac{1}{i(At)^{\frac{3}{2}}}\int_0^{i(At)^{\frac{1}{2}}} e^{-x^2}dx\right) \tag{13.20}$$

$$= \frac{t^{\frac{1}{2}}}{A} - \frac{\pi^{\frac{1}{2}}}{2}A^{-\frac{3}{2}}e^{-At}erfi\left[(At)^{\frac{1}{2}}\right] \tag{13.21}$$

where $erfi(z) = \frac{erf(iz)}{i}$ is an imaginary error function. Now,

$$erfi(z) = 2\pi^{-\frac{1}{2}}\sum_{n=0}^{\infty}\frac{z^{2n+1}}{n!(2n+1)} \tag{13.22}$$

So the integral is given by

$$\frac{t^{\frac{1}{2}}}{A} - A^{-\frac{3}{2}}e^{-At}\sum_{n=0}^{\infty}\frac{(At)^{\left(n+\frac{1}{2}\right)}}{n!(2n+1)} \tag{13.23}$$

$$= \frac{t^{\frac{1}{2}}}{A}\left(1-e^{-At}\sum_{n=0}^{\infty}\frac{(At)^n}{n!(2n+1)}\right) \tag{13.24}$$

Combining equations (13.18) and (13.24) gives:

$$I = zF\frac{cD}{\delta}\left[1-\exp\left\{-B\sqrt{t}\left(1-e^{-At}\sum_{n=0}^{\infty}\frac{(At)^n}{n!(2n+1)}\right)\right\}\right] \tag{13.25}$$

This result implies that the current response should show a monotonically rising transient, with the limiting current (for a given species) dependent only on the strength of the external agitation.

13.4 References

[1] M. Avrami, J. Chem. Phys. 1939, 7, 1103.
[2] M. Avrami, J. Chem. Phys. 1940, 8, 212.
[3] U. R. Evans, Trans. Faraday Soc. 1945, 365.
[4] M. Y. Abyaneh, M. Fleischmann, J. Electrochem. Soc. 1991, 138, 2485.
[5] A. N. Kolmogorov, Bull. Acad. Sci. URSS Sci. Math. Nat. 1937, 3, 355.
[6] F. Canac, Compt. Rend. 1933, 196, 51.
[7] K. L. Mampel, Z. Phys. Chem., Abt. A 1940, 187, 43.
[8] E. Bosco, J. Chem. Phys. 1992, 97, 1542.
[9] M. Sluyters-Rehbach, J. H. O. J. Wijenberg, E. Bosco, J. H. Sluyters, J. Electroanal. Chem. 1987, 236, 1.
[10] F. Marken, R. P. Akkermans, R. G. Compton, J. Electroanal. Chem. 1996, 415, 55.
[11] R. de Levie, in Advances in Electrochemistry and Electrochemical Engineering, Vol. 13 (Eds.: H. Gerischer, C. W. Tobias), Wiley, New York, 1984, p. 1.